UNIVERSIDAD AUTÓNOMA DE NUEVO LEÓN

FACULTAD DE INGENIERÍA MECÁNICA Y ELÉCTRICA

''SYNTHESIS AND CHARACTERIZATION OF SILVER AND COPPER BISMUTH HALIDE PEROVSKITE THIN FILMS FOR OPTOELECTRONIC APPLICATIONS''
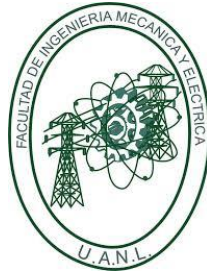
SUBMITTED IN PARTIAL FULFILLMENT OF THE REQUIREMENTS FOR THE DOCTORAL DEGREE IN MATERIALS ENGINEERING

SUBMITTED BY,

ANJALI ADAPPATTU RAMACHANDRAN

San Nicolás de los Garza, Nuevo León

UNIVERSIDAD AUTÓNOMA DE NUEVO LEÓN
FACULTAD DE INGENIERÍA MECÁNICA Y ELÉCTRICA

''SYNTHESIS AND CHARACTERIZATION OF SILVER AND COPPER BISMUTH HALIDE PEROVSKITE THIN FILMS FOR OPTOELECTRONIC APPLICATIONS''

SUBMITTED IN PARTIAL FULFILLMENT OF THE REQUIREMENTS FOR THE DOCTORAL DEGREE IN MATERIALS ENGINEERING

SUBMITTED BY,

ANJALI ADAPPATTU RAMACHANDRAN

San Nicolás de los Garza, Nuevo León

Universidad Autónoma de Nuevo León
Facultad de Ingeniería Mecánica y Eléctrica
Subdirección de Estudios de Posgrado

Los miembros del Comité de Tesis recomendamos que la Tesis " **Synthesis and characterization of silver and copper bismuth halide perovskite thin films for optoelectronic applications** ", realizada por el alumno **Anjali Adappattu Ramachandran** , con número de matrícula **1887240** , sea aceptada para su defensa como requisito para obtener el grado de **Doctor en Ingeniería de Materiales** .

El Comité de Tesis

Dr. Sadasivan Shaji
Director

Dra. Bindu Krishnan
Revisor

Dr. David Avellaneda Avellaneda
Revisor

Dr. Jorge Oswaldo González Garza
Revisor

Dr. Miguel Angel Gracia-Pinilla
Revisor

Vo. Bo.

Dr. Simón Martínez Martínez
Subdirector de Estudios de Posgrado

111

San Nicolás de los Garza, Nuevo León, Febrero de 2021

Dedicated to,

Amma & Acha,

(Mrs. Suseela and Mr. Ramachandran)

who always stood by my side and encouraged me to do what my heart says, especially this one

Acknowledgements

I would like to thank from the bottom of my heart,

To my **beloved family: My parents, aunt, grandpa, sister and brother** for, letting me go with my dreams and plans, believing in me, pushing me forward, and supporting me. I do not know to express my gratitude and love for the selfless love, care, support, and sacrifice they made for fulfilling my dream.

To my beloved close friends**: Rincy, Sebastian, Hari, Thomasutty and Shalabhu** for being there, supporting selflessly to make my dream come true, listening to me with love and care.

To all my beloved ones, friends and colleagues from Mexico and India for their love and support during this Ph.D. life.

To all the security guards of FIME, UANL for their love and support especially Juan uncle.

To mumma, uncle, and Tia Maya for supporting me, treating me with lots of love and helping me to keep my foot on the ground. Making me remember: 'take a new page from your life book so that you can add a new story to it'.

To all Mexicans for their nice, friendly, welcoming and supportive nature and the Malayali community from Monterrey for their love.

Contents

Abstract

If we look back into the past few decades, we have experienced that the optoelectronic field has revolutionized the world and impacted our daily lives. Photodetectors are one of the devices that convert light energy into electrical signals, which contributes to the development of the photoelectronic field. For this reason, photodetectors are considered as one of the inevitable semiconductor devices in fields such as remote sensing technology, optical communications, and optoelectronic applications. Till the present scenario, photodetectors have achieved the ability to detect light in UV-Vis-NIR region, making them useful for various applications in industrial, environmental, and medical fields. Several semiconductor materials have been explored to absorb light because of their appropriate bandgap values and are used for the fabrication of photodetectors. For the past few years, lead-based devices are getting considerable attention due to their outstanding performances. However, the toxicity and stability of lead-based semiconductor materials limit their applications on a large scale. Thus, developing novel materials with high stability and low toxicity which can be processed by low-cost methods is essential for future optoelectronic applications.

Bismuth based materials are considered as less toxic material due to their excellent optoelectronic properties. Antimony iodide is a material with a similar structure to bismuth iodide and less explored so far. While synthesizing and characterizing various binary materials such as bismuth iodide (BiI_3), copper iodide (CuI) and silver iodide (AgI), we find that these binary thin films can be used for the preparation of perovskites. A special focus has been given to study the structure, morphology, composition, and optoelectronic properties of SbI_3 because only a few experimental studies are reported so far. We developed a photodetector device by putting in many efforts to optimize the best optimum conditions for the formation of SbI_3. The main objective of this thesis is the synthesis and characterization of bismuth-based perovskite materials for optoelectronic

ABSTRACT

applications. Silver bismuth iodide (Ag_2BiI_5) and copper bismuth iodide (Cu_2BiI_5) perovskite's structure, morphology, elemental composition, and optoelectronic properties are deeply investigated and presented. We find that the bismuth iodide concentration has a significant role in tuning the properties of Ag_2BiI_5 perovskites. Whereas the structure, morphology, composition, and optoelectronic properties of Cu_2BiI_5 perovskites are tunable by changing the copper thickness. Based on these studies, we developed a stable and reproducible photodetector with good selectivity towards visible light. We find that these bismuth-based perovskite materials have great potential for photodetector applications and a promising future for other optoelectronic applications. This thesis will inspire to do more research on these novel perovskites and give more insights to explore lead-free materials for future optoelectronic applications.

List of figures

LIST OF FIGURES
_____

List of tables

Abbreviations

BE:	Binding Energy		PCE:	Power conversion efficiency
CB:	Conduction band		PV:	Photovoltaics
CBI:	Copper Bismuth iodide		XRD:	Powder X-Ray Diffraction
CBD:	Chemical Bath Deposition		SE:	Secondary electron mode
CIGS:	Copper indium Gallium selenide/sulfide		SEM:	Scanning Electron Microscopy
DMF:	Dimethyl Formamide		SEM:	Scanning Electron Microscopy
EDX:	Energy Dispersive X-Ray		SBI:	Silver Bismuth iodide
ETL:	Electron transport layer		TCMs:	Transparent conducting materials
FA:	Formamidinium		TO:	Transverse optical mode
FTO:	Fluorine-doped tin oxide		UV-Vis-NIR:	Ultraviolet-Visible- Near Infrared
HTL:	Hole transport layer		VB:	Valence band
I-V:	Current-Voltage		XRD:	X-Ray Diffraction
JCPDS:	Joint Committee on powder Diffraction Standards		XPS:	X-Ray Photoelectron Spectroscopy
LED:	Light Emitting Diode			
MA :	Methylammonium			

Chapter 1

Emerging lead-free perovskite materials in optoelectronics

1.1. Semiconductor materials for optoelectronic applications

Based on the conductivity properties materials can be classified into three types - insulators, semiconductors and metals. They are recognized based on the position and occupancy of valence band (VB) and conduction band (CB). The highest occupying band is called valence band and the lowest un-occupying band is called conduction band. The energy gap between valence and conduction band is called bandgap (E_g). Figure 1.1 shows the schematic diagram for the classification of materials based on their energy gap. Metals are materials whose conduction band overlaps with the valence band. The valence electrons in metals are free electrons that can move easily, resulting in good electrical/thermal conductance. There be a small energy gap (0.1-3 eV) between these bands for semiconductor materials, where for insulators, there be a large energy gap (>3 eV) between these two bands. The reason behind using semiconductor materials for photovoltaic application is that electrons can be easily excited from the valence band maximum to the conduction band minimum using solar energy because of their narrow band gap.

In every field of our life, semiconductor optoelectronic devices which convert light into electrical signals and vice versa play a crucial role. They put their fingerprints in various applications such as photodetectors, light-emitting diodes (LEDs), laser diodes, telecommunication systems, information technology, etc. In every optoelectronic device, an interaction between light and semiconductor occurs and its performance depends on the electronic properties of material. Thus, it is essential to improve the optoelectronic properties of materials, thereby improving the device performance.
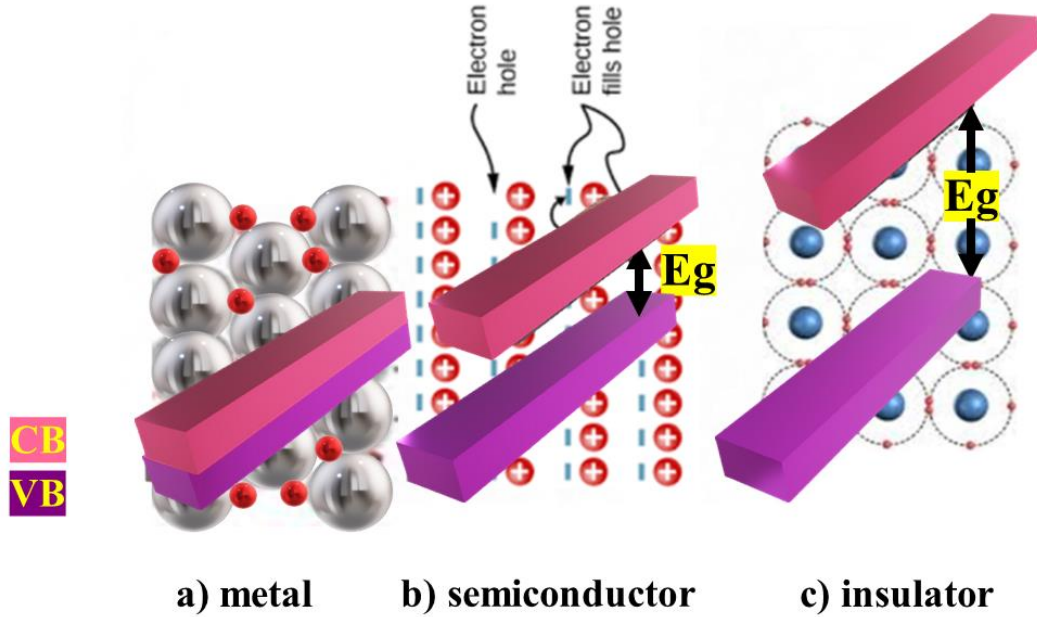
Figure 1.1. Schematic representation of materials based on their position of valance band and conduction band a) metals, b) semiconductors and c) insulators.
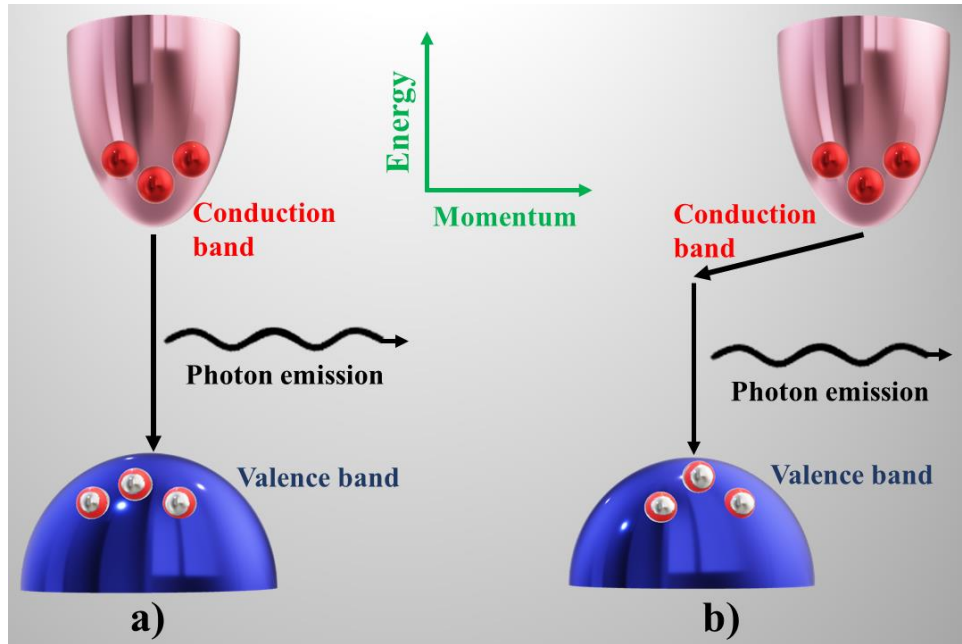
Figure 1.2. Schematic representation of E-k diagram for a) direct bandgap and b) indirect bandgap semiconductors.

The suitability of semiconducting materials for optoelectronic applications depends on their type of bandgap. There are two basic types of semiconductors: direct bandgap

semiconductors and indirect bandgap semiconductors, as shown in Figure 1.2. For direct bandgap semiconductors, the conduction band minimum and valence band maximum have the same k-vectors. In contrast, indirect bandgap semiconductors have different k values.

The energy and momentum must be conserved for any kind of electron transition. Photon wavevector is always smaller than the electron wavevector. When a photon interacts with an electron, the transition must occur vertically thereby keeping energy-momentum conserved. For the indirect bandgap semiconductors, the conduction band minimum and valence band maximum are not vertically aligned. Thus, when a photon interacts with the electron in the valence band, the energy and momentum will not be conserved. So, another particle is involved in the indirect transition and is called phonon. Phonons are particles associated with lattice vibrations and they have smaller energy and larger momentum compared to photons. An indirect transition involves a three-particle interaction thus the probability of transition is significantly reduced. That is why direct bandgap semiconductors are mainly used for optoelectronic applications. Many semiconductor materials have been explored for optoelectronic application. Lead (Pb) based compounds are one of the most studied materials for optoelectronic applications for the past few years. When considering its toxicity and the harm that it causes to the environment, there is an urge to explore new less-toxic materials.

1.2. Organic-inorganic perovskites

Perovskite was originated from a mineral named calcium titanate ($CaTiO_3$) and was found by Gustav Rose in the Ural Mountains of Russia. Perovskite structure was named by the Russian mineralogist L.A. Perovski. Till now many materials have been discovered with $CaTiO_3$ perovskite crystal structure. Perovskites have a basic crystal structure with the general formula ABX_3 (Figure 1.3). For organic and inorganic hybrid perovskites based on metal halides, A is an organic cation (e.g., CH_3NH_3 or MA+, fromamidinium or FA+) or inorganic cation (e.g. K^+, Rb^+, Cs^+) which is selected to balance the total charge, B is a metal cation (e.g., Sn^{2+} or Pb^{2+}) and X is a halogen (Cl, F, Br or I). Perovskite structure involve a network of corner-sharing BX_6 octahedra with A cations occupying 12-fold coordinated holes within the structure[1,2].
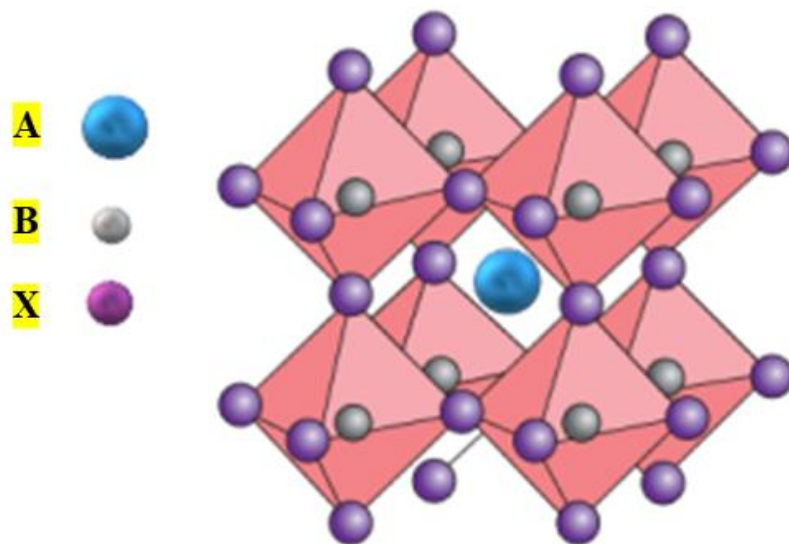
Figure 1.3. Schematic representation of basic structure of perovskite where A,B and X atoms are shown in blue, grey and purple colors[3].

A solar cell is one of the optoelectronic devices that use solar energy for electricity production. Photovoltaics is a phenomenon that converts directly solar energy into electrical energy using semiconductor materials[4]. There are different types of solar cells and they are classified according to the type of material used for charge generation. Earlier photovoltaic (PV) technologies were mainly based on commercial silicon, gallium arsenide (GaAs), cadmium telluride (CdTe), and copper indium gallium selenide/sulfide (CIGS)[5–8]. According to the junctions applied, solar cells are classified into three major groups, i.e., inorganic p-n junction solar cells, hybrid solar cells, and organic e-acceptor/e-donor solar cells.

Interestingly, hybrid solar cells are again classified into two groups: dye-sensitized solar cells and other hybrids. In recent years, solar cells based on quantum confinement and nanostructures also have been investigated[9]. The basic structure of a solar cell is shown in Figure 1.4. The device performance varies from one cell to another since there are differences in the crystal structures, the fabrication of the device structures, and power generation of different PV devices. A PV device can be an excellent one when it has high power conversion efficiency (PCE), less expensive precursor materials, a simple device fabrication process, and has a longer lifetime. Methylammonium lead iodide was the first

metal halide perovskite solar cells reported by Miyaska et *al.* in 2009. After that, many efforts have been made so far. Perovskite solar cells have become very popular in a short period (10 years) since their PCE has jumped from 3.8 to 25.2% [10,11] as shown in Figure 1.5.
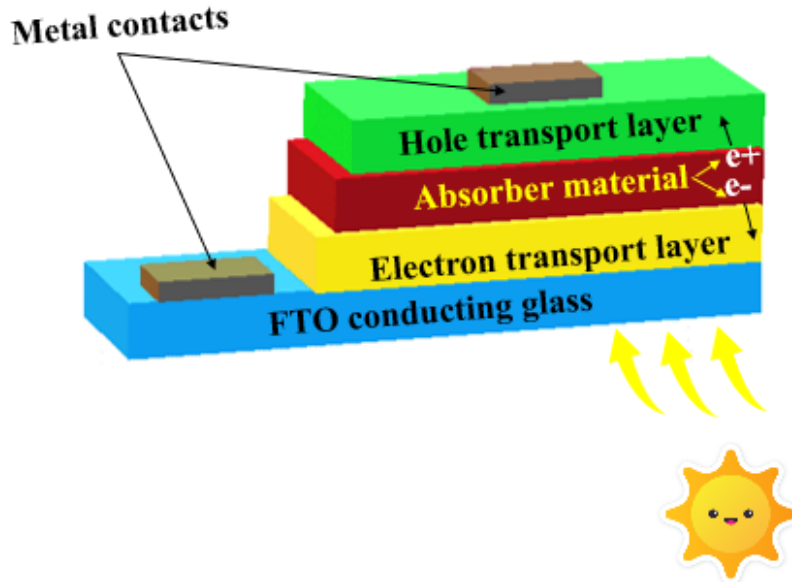
Figure 1.4. Device structure of a p-n junction solar cell.
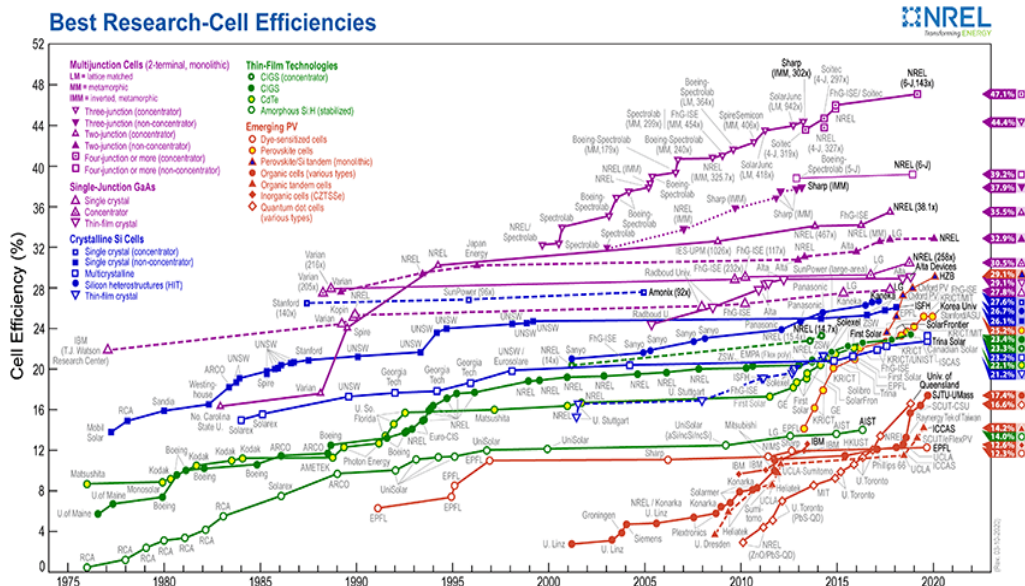
Figure 1.5. Best cell efficiency chart by NREL https://www.nrel.gov/pv/assets/pdfs/best-research-cell-efficiencies.20191106.pdf (accessed January 4, 2020).

Perovskite materials have attractive optoelectronic properties such as high optical absorption coefficient in the Vis-NIR range, tunable band gap, prolonged carrier recombination lifetimes, high electron/hole mobilities, and small electrons/hole effective masses and binding energy of the exciton[12–14]. There are two essential factors related to the perovskite crystal structure. They are the tolerance factor (t) and octahedral factor (μ). The structural stability of perovskite can be described by Goldschmidt tolerance factor (t), which is given by the equation,

$$t = \frac{RA + RB}{\sqrt{2}(RX + RB)} \qquad (1)$$

where RA, RB and RX are the ionic radii of the metal cation and anion ions. Whereas the distortion of the crystal can be predictable by the octahedral factor which is given by,

$$\mu = \frac{RB}{RX} \qquad (2)$$

For a stable octahedron, the octahedral factor's value should range from 0.41 to 0.73[15]. The ideal value for the tolerance factor should be ≈ 1, and it is found that most of the 3D perovskite materials have 't' in between 0.8 and 1[16–18]. Organic-inorganic hybrid halide perovskite materials attain different structures depending on the tolerance factor. For example, they tend to form cubic structure when 0.8 < t < 1, hexagonal structure when t > 1, and orthorhombic structure when t < 0.8[18]. Depending upon the tolerance factor, there is a wide variety of organic-inorganic hybrid halide perovskites[19].

The organic-inorganic perovskite performance has become comparable with commercial silicon-based optoelectronic devices, but are suffering from degradation and distortion of their crystal structure under heat, moisture and light. As a result, perovskites performance is affected by their low stability, which is mainly due to their instability of its organic components (e.g. methylammonium and formamidinium) under moisture and UV light. These organic components are also easy to react with water molecules, sunlight, and heat to form intermediate hydrates, which results in the perovskite degradation and thus poor lifetime[20–23]. Besides the instability factor, the toxicity of lead also affects the commercialization of lead-perovskite-based optoelectronic devices. There have been

many efforts reported to improve the stability of perovskites so that the optoelectronic devices' commercialization can practically be possible. For example, two-dimensional perovskite structure designing, mixing with Cs^+ to adjust the band gap value and tolerance factor resulted in improved PCE and long-term stability[24,25]. Also, deposition of two dimensional perovskites on the top of the three dimensional perovskites resulted with higher stability of the devices by engineering the interface[26,27]. Devices encapsulated with polymers also improved the stability and it plays an important role in the commercialization of devices with long-term stability[28–30].

1.3. Emerging lead-free perovskite materials

Lead halide based perovskite materials have limitations like its toxicity, bioavailability, carcinogenicity, water solubility of lead can contaminate the water, and instability under ambient conditions like air, heat, humidity and light[31,32]. Due to these reasons, many elements have been investigated to replace lead, such as Sn, Ge, Bi, Sb and some transition metals, which resulted in perovskite structure with attractive optoelectronic properties[33,34].

Lead substitution with environmentally friendly and non-toxic elements resulted in lead-free metal halide perovskites and it can be achieved in two ways. The first way is substitution of homovalent lead with isovalent cations such as group 14 elements (example, Ge, Sn, etc.), alkaline earth metals (example, Mg, Ca, Sr, Ba, etc.), and transition metals (example, Mn, Fe, Ni, Pd, Cu, Cd). The second way is heterovalent substitution with aliovalent cations such as transition metals, main group elements (Sb, Bi, Te etc.), lanthanides and actinides[35]. Homovalent and heterovalent substitution based on the elements from periodic table resulted into a wide variety of lead-free metal halide perovskite materials. For example, the first homovalent substitution of lead are group-14 elements like Sn and Ge wherein Sn^{2+} and Ge^{2+} have a similar electronic configuration as Pb^{2+}. $CH_3NH_3SnI_3$ and $CH(NH_2)_2SnI_3$ are the most studied Sn halide perovskites. Both Ge and Sn have good optical properties, while they can quickly oxidize from Sn^{2+} and Ge^{2+} to +4 oxidation states[36,37]. The homovalent and heterovalent substitution of lead with the periodic table elements is schematically shown in Figure 1.6.

Periodic Table of Elements

Figure 1.6. Homovalent and heterovalent substitution of lead with different elements from periodic table[35].

Due to the +2-oxidation state like Pb and suitable ionic radii to form perovskite structures, non-toxic, and earth abundance, alkaline earth metals such as Mg, Ca, Sr and Ba can be used for the replacement of Pb. They have been investigated extensively due to the photoluminescence properties that arrived from doping with rare earth metal cations like Eu^{2+}, Yb^{2+}, or Tm^{2+}[38–41]. Transition metal halide perovskites have been studied for lead replacement because of their magnetic properties. For example, transition metals like vanadium, manganese, iron, cobalt, nickel, palladium, copper, zinc, cadmium, and mercury have been considered as candidates for Pb replacement transition metals in the perovskite structure[42,43]. Various transition metal halide perovskites have been reported as alternatives to lead in the perovskite crystal structure[44,45]. Multiple oxidation states of perovskites based on transition metals could be one problem when considering its

chemical stability[46]. In addition to these materials lanthanides and actinides (e.g. La^{3+}, Ce^{3+}, Pr^{3+}, Nd^{3+}, Sm^{3+}, Eu^{3+}, Gd^{3+}, Dy^{3+}, Er^{3+}, Tm^{3+}, Lu^{3+} and Pu^{3+}, Am^{3+}, Bk^{3+}) have been used in quaternary halide double perovskites as an alternative for lead halide perovskites.

Another approach for replacing Pb is the heterovalent substitution, where a cation in another valence state replaces the divalent lead cation. That is, it can be a monovalent, trivalent or tetravalent cation. The straightforward substitution of the heterovalent cation is not possible since the valence states are different. Thus, there are two approaches that we follow for the heterovalent substitution of Pb. The first method is the mixed-valence approach, where Pb with +2 valence state is replaced with a mixture of monovalent and trivalent cations to give an overall valence of +2. Thallium and gold halide perovskites follow the mixed-valence approach[47,48]. In the second method, the divalent Pb^{2+} is substituted with the trivalent cations like Sb^{3+} and Bi^{3+}[49–51]. In this approach the perovskite structure changes from ABX_3 to $A_3B_2X_9$ to maintain charge neutrality. Another way to achieve the replacement of Pb halide perovskites is by utilizing chalcogenide anions (split-anion method). It can be achieved where the halides in the metal halide perovskites are substituted with chalcogenide anions. As a result, the crystal structure ABX_3 changes to chalcogenide halide perovskites with general formula $(Ch, X)_3$. Metal chalcogenide bonds are more covalent compared to metal halide bonds. This more covalent bonding nature leads to prolonged stability under ambient atmosphere[52,53]. In this decade, this class of materials has become popular and there have been extensive investigations regarding their crystal structures and physicochemical properties[54,55]. In addition to these materials, oxidic perovskites can be a hot topic for lead replacement studies in the optoelectronics field. There have been some reports regarding their suitable optical properties for optoelectronic application[35,56]. Table 1.1. shows the list of some emerging lead-free materials, their respective band gap values.

Table 1.1.Lead replacement by the elements and the resultant perovskite materials.

Perovskite	Crystal structure	Energy band gap (eV)	Reference
$CH_3NH_3SnBr_3$	Pseudocubic (*P4mm*)	2.15–2.2	[1,57]
$CsSnI_3$	Orthorhombic	1.27–1.31	[58–61]
$CH(NH_2)_2SnI_3$	Orthorhombic (*Amm*2)	1.4–1.41	[62–65]
$CsGeI_3$	Trigonal (*R3m*)	1.53–1.63	[37,66–70]
$CH_3NH_3GeI_3$	Trigonal (*R3m*)	1.9–2.0	[37,66,69]
$CH_3NH_3MgI_3$	Tetragonal	1.5	[43]
$CsMgI_3$	Orthorhombic	1.7	[43]
$CH_3NH_3CaI_3$	Tetragonal/pseudo-orthorhombic	2.95, 3.78	[71,72]
$CH_3NH_3SrI_3$	Tetragonal	3.6	[71]
$CH_3NH_3BaI_3$	Tetragonal	3.3	[71]
$(CH_3NH_3)_2CuCl_2Br_2$	Orthorhombic (*Acam*)	2.12	[73]
$CuBiI_4$	Cubic	1.81	[74]
$Rb_3Sb_2Br_9$	Trigonal ($P\bar{3}m1$)	2.48	[75]
$Cs_3Bi_2I_9$	Hexagonal ($P6_3/mmc$)	1.8-2.2	[49,75,76]
Cs_2TeI_6	*Fm 3-m*	1.52–1.59	[75]

1.4. Bismuth-based perovskite materials

Bismuth is the 83rd element in the periodic table and gets often confused with lead (Pb) and tin (Sn). The word bismuth originated from the German word 'wismuth' means white mass[77]. Bismuth is receiving quite good interest as a Pb replacement material. Various factors make them attractive, such as the trivalent metal cation, Bi^{3+} isoelectronic to Pb^{2+}[78]. Also, Bi^{3+} has similar electronegativity as Pb^{2+}. For example, the electronegativity of Bi^{3+} is 2.02 whereas Pb^{2+} is 2.33. In addition to these, the ionic radii of both metal cations are comparable values, i.e., 103 pm for Bi^{3+} and 119 pm for Pb^{2+}[79–81]. It may help the easy incorporation into the perovskite crystal structure. Figure 1.7. shows a schematic representation for using Bi^{3+} in the lead-replacement.
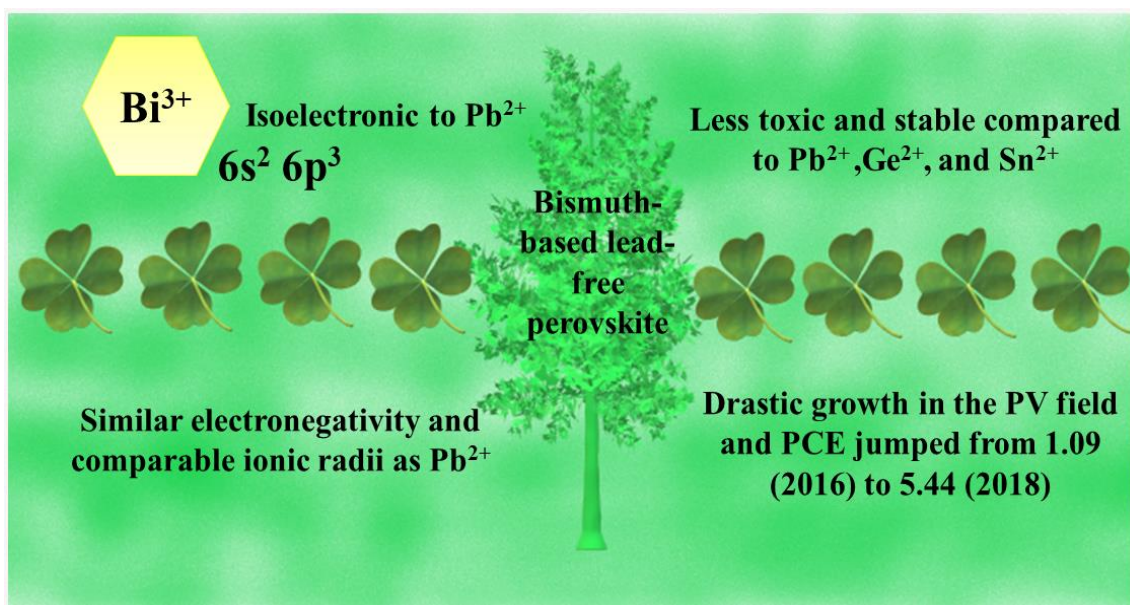
Figure 1.7. Schematic representation for using Bi^{3+} in the lead-replacement.

Besides, bismuth is a promising stable metal cation when compared to Sn^{2+} and Ge^{2+} because both get easily oxidized under ambient atmospheric conditions. Thus, Bi^{3+} is one of the promising candidates for a lead-free mission. There is a wide variety of bismuth halide perovskites which range from zero-dimensional dimer units, one dimensional, two-dimensional up to three-dimensional double perovskites structure[51]. Due to different valence states trivalent bismuth cation cannot directly replace the divalent

lead cation. For example, when it is combined with monovalent metal cations such as Cu, Ag, and Au double perovskites (example, $Cs_2BiAgCl_6$ and $Cs_2BiAgBr_6$) can be formed. These materials have shown electronic properties similar to lead-based perovskites and considerable stability towards heat and moisture with appreciable bandgap values in the visible range[82,83].

Regarding optoelectronic applications, $(CH_3NH_3)_3Bi_2I_9$ is the well-studied bismuth halide perovskite material. This material is an environmentally promising semiconductor and stable under ambient atmospheric conditions and humidity[84]. In 2016, Johansson et al. successfully synthesized and fabricated $Cs_3Bi_2I_9$ or $MA_3Bi_2I_9$ PV devices[85]. Interestingly, Lehner et al. experimentally and computationally investigated the all-inorganic bismuth iodide perovskites $A_3Bi_2I_9$(A = K, Rb, Cs). They found that from the calculated band structures, the K and Rb based perovskites are direct bandgap semiconductors whereas Cs-based perovskites are indirect bandgap semiconductors[51]. Thus, a large number of studies are going on the bismuth-based light absorbing materials. Iodo-bismuthates are among them. Their high solubility at room temperature and attractive electrical and optical properties find them a position among the perovskite family[86,87]. The tuning of optical and electrical properties of the iodo-bismuthates is achieved by adding monovalent metal cations like Ag and Cu into their structure to form Ag-Bi-I and Cu-Bi-I perovskites. In 1991, Fourcroy et al. first reported the $CuBiI_4$ phase[88]. In 2016, Kim et al. were the first ones to report the PV device-based on silver bismuth iodide with PCE of 1.22%[89]. Table 1.2 shows various Ag-Bi-I and Cu-Bi-I perovskites and their bandgap values.

Table 1.2. Bismuth based perovskites by addition of silver and copper metal cations into the iodo-bismuthate system and resultant perovskite materials.

Material	Crystal structure	Band gap (eV)	References
$AgBi_2I_7$	Cubic	1.87	89
Ag_2BiI_5	Hexagonal	1.85	90

Ag_3BiI_6	Trigonal	1.79-1.83	[91]
$Ag_3BiI_xS_{6-x}$	Hexagonal	1.84-1.89	[92]
$AgBiI_4$	Cubic (Fd3m)	1.8	[93]
$Ag_2Bi_3I_{11}$	Cubic (Fd3m)	1.8	[94]
$Ag_4Bi_5I_{19}$	Rhombohedral	1.8	[94]
$Cs_2AgBiCl_6$	Cubic (Fd3m)	2.77	[76]
$Cs_2AgBiBr_6$	Cubic (Fd3m)	2.19	[76]
$CuBiI_4$	Cubic (Fd3m)	1.81-2.67	[74,95]

1.5. The photodetector device

Photodetectors are devices that convert the incident light energy into electrical signals through the photoelectric phenomenon. In this era, photodetectors have made their signature in the various scientific and industrial applications such as chemical/biological sensing, imaging and environmental monitoring[96,97]. Their remarkability makes them useful in various fields, mainly operating in the IR region. Further, their applicability has spread over different areas, such as military, detection of a target, space, medical imaging, remote control, communication, and industry automation control[98,99]. A photodetector's performance can be boosted by choosing appropriate semiconducting materials with high carrier mobility and absorption coefficient[100]. These properties ensure significant absorption of light by the material and thereby the resulting higher amount of photocurrent. Semiconductor photodetectors are intensively used in the optical communication system. Primary photodetectors are based on inorganic semiconducting materials like Si, GaN and InGaAs[101]. These traditional photodetectors have some limitations like manufacturing complexity, high cost, lack of mechanical flexibility, and high driving voltage, making them unattractive for industrial applications[102]. As mentioned earlier, perovskite materials have good optoelectronic properties, low cost, and easy fabrication process, and this makes them grab more attention for perovskites-based optoelectronic applications. They have large absorption coefficient values over the

13

wavelength ranges from 300-800 nm (UV-Vis-IR), making them applicable for broadband photodetection[103].

In general, photodetectors are wavelength-specific devices, i.e., the device works over the specific wavelength region, depending on its bandgap. Thus, absorption coefficient (α) of the semiconductor material is an important factor for a photodetector. The absorption coefficient is the factor that determines the penetration depth of incident radiation into the device. According to Beer Lambert's law, the absorption coefficient and the penetration depth are inversely proportional to each other. Thus, if materials have larger α, the absorption will be close to the material surface, whereas, materials with small α most of the incident photons will pass through without absorption. Another critical factor that affects a photodetector's performance is its response time, especially when the incident light is in the form of pulses. There are three main steps involved in the conversion of light to electricity by a photodetector. The first step is the photon absorption and generation of carriers when radiation is incident on the semiconductor. The second step is the transportation of photogenerated charge carriers to the metal electrodes. The last step is to extract photo-generated charge carriers in the form of electric current to the external circuit. In general, while choosing the metal contacts, it should be noted that the work function of the metal (φ_m) should be closer to the work function of the semiconductor(φ_s) and the work function of the metal electrodes must be higher than the electron affinity of the respective semiconductor (χ_s). The schematic diagram of a photodetector is shown in Figure 1.8.
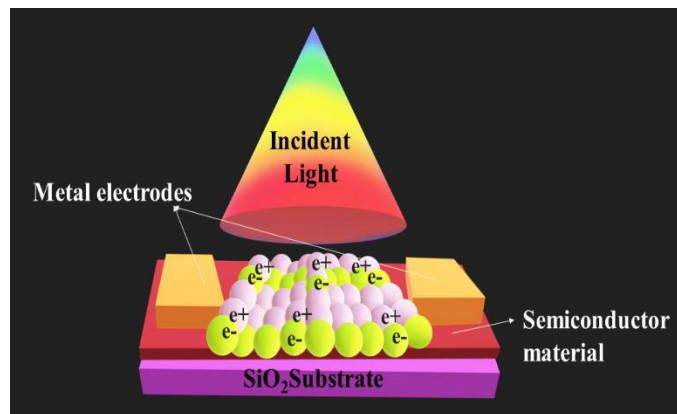
Figure 1.8. Schematic diagram of a basic photodetector.

A good functioning photodetector possesses specific key parameters such as high responsivity, high sensitivity, narrow spectral selectivity, high detectivity, high photon to current conversion efficiency, fast response time, etc. Responsivity is defined as the amount of photocurrent generated per unit area per unit light intensity. If I_d is the dark current, I_l is the photocurrent, L_λ is the intensity of the incident light and S is the effective area of illumination, then we can calculate the responsivity using the following equation[104],

$$R = \frac{I_{light} - I_{dark}}{L_\lambda S} \qquad (3)$$

Another factor is the sensitivity which can be given by the equation[105],

$$S\% = \frac{I_{light} - I_{dark}}{I_{dark}} \times 100 \qquad (4)$$

The next factor is the external quantum efficiency of the photodetector device. It can be defined as the ratio between the number of charge carriers collected by the photodetector and the number of incident photons and is given by the following equation[106],

$$EQE = \frac{Rhc}{e\lambda} \qquad (5)$$

where R is the responsivity, h is the Plank's constant, c is the velocity of light in vacuum, e is the charge of an electron and λ is the wavelength of the incident light.

Specific detectivity is another most important factor for a photodetector which is defined as the measure of least detectable radiant power or in another word its ability to detect the weakest light signal and is given by the equation[106],

$$D = \frac{\sqrt{AB}}{NEP} = \frac{e\,\lambda\sqrt{A}EQE}{hci_{noise}} \qquad (6)$$

The fast response speed is an attractive feature of a photodetector. The response speed measures its rise time (τ_r) and fall time (τ_f) response to an optical signal, which can be defined as the time between 10% and 90% of the maximum value of photocurrent. The

response speed is strongly related to the photogenerated charge carrier collection and transport. Small electrode spacing helps to have a fast response, and it ensures sufficient light absorption with a small amount of leakage current[107].

1.6. Principle of operation

In semiconducting materials, the photodetection process is based on a general principle of the generation of electron/hole pairs under light illumination. When a semiconducting material is illuminated with radiation, and if the incident photons have energy greater than or equal to the bandgap of the semiconductor, the photons will be absorbed by the material. As a result, the absorbed photons promote electrons to jump from the valence band to the conduction band and we can say that the electrons are in the excited state. They can act as free electrons and free to travel through the crystal structures under the influence of an externally applied electric field. In addition to the flow of free electrons in the conduction band, the holes left in the valence band also contribute to the current by moving from one state to another. Thus, the current generated by the electron-hole pairs through the absorption of light is named as 'photocurrent,' which is directly proportional to incident light intensity[108].

Based on the nature of the applied electric field, there are two photodetectors classes: ''photoconductors and photovoltaic detectors.'' The photoconductors consist of a single layer of semiconducting material with two ohmic contacts. When a bias voltage is applied at the electrode ends, an electric field is generated, leading to the generation and collection of charge carriers. The photo-detecting devices are photoconductors, photodiodes, and phototransistors. Figure 1.9 shows the diagram of a photo-conducting device. Here, the device consists of a single layer of semiconductor with ohmic contact at both ends. A fixed bias voltage V_B, applied between the contacts generates a current (bias current) I_B. This bias current flows through the semiconductor material by obeying Ohm's law. The light active surface is formed between the two electrodes. When it is illuminated with light, the photogenerated carriers produce photocurrent. This current adds to the bias current under the presence of the electric field, leading to an increase in the conductivity of the device[109].
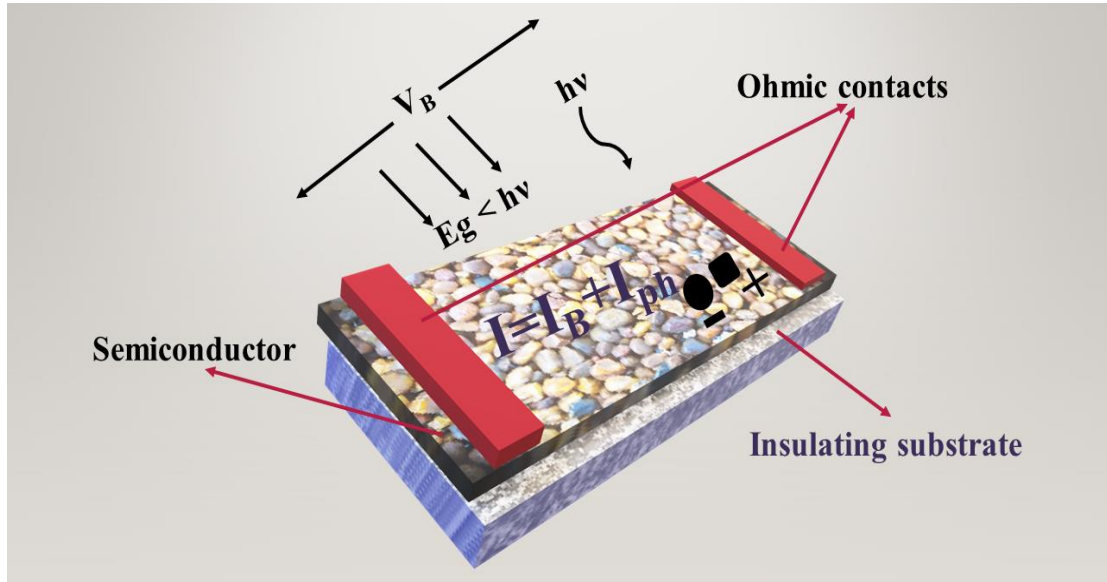
Figure 1.9. Schematic diagram and working of a photo-conducting device when incident light photon of energy *hv* is absorbed by the material.

When a metal is in contact with the semiconductor material, electron transfer occurs from the semiconductor to the metal. In general, while choosing the metal contacts, it should be noted that the metal's work function (φ_m) should be closer to the work function of the semiconductor(φ_s) and the work function of the metal must be greater than the electron affinity (χ_s) of the semiconductor. Figure 1.10 shows the energy level diagram when a metal is in contact with the semiconductor.
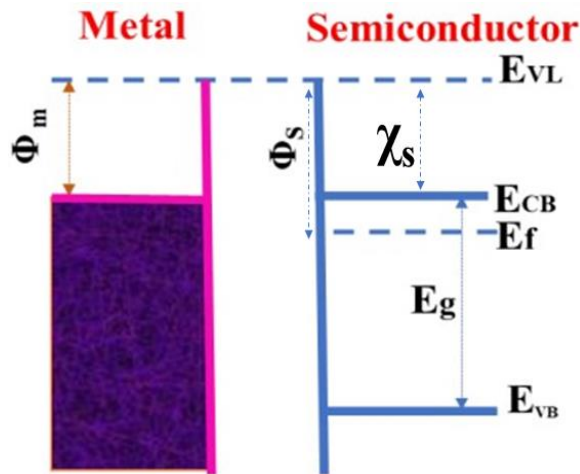
Figure 1.10. Energy level diagram when a metal is in contact with the semiconductor in thermal equilibrium.

17

In thermal equilibrium, the Fermi levels of the metal and semiconductor are equalized, and electron transfer occurs. As a result, a depletion region is formed at the metal-semiconductor junction. Its space charge region depends on the type of semiconductor, whether it is *p*-type or *n*-type. Thus, in equilibrium there is an intrinsic electric field at the metal-semiconductor junction. When it is illuminated, electron-hole pairs are generated in the depletion region. Two factors affect a photodetector's performance, and they are separation and transport of photogenerated charge carriers. The phenomenon of generation of photo-excited charge carriers in the depletion region separated by the electric field leads to photocurrent[110].

1.7. Perovskites based photodetectors

Silicon, germanium, and gallium arsenide are the most studied materials for different optoelectronic applications. They have been explored widely for photodetector applications too, but high manufacturing cost, complexity, less-flexibility, and necessity of high applied voltage limit their applicability on a large-scale. Besides, for the detection of feeble signals, these traditional photodetectors demand low temperature[111]. Thus, it is essential to find alternative materials with high absorption in the Vis-NIR region, low cost, solution processability, high sensitivity and detection of signals in the broad spectrum. Many organic materials, nanocomposites and nanoparticles have shown significant performance for photodetection purposes[112–114]. The low charge-carrier mobility of these active layers hinders the overall performance of the device[115].

Thus, the organic-inorganic perovskite materials have been explored and made their fingerprint in the optoelectronics field with their outstanding performances. The high charge carrier mobility, absorption coefficient, low cost, low-temperature solution processability, simplicity in device fabrication, flexibility properties, etc., warmly welcomed them to photodetector application world[116]. For example, the perovskites' large absorption coefficient is $\approx 10^5 \, cm^{-1}$ and can absorb light efficiently in the Vis-NIR region. As a result, only a thin layer of material is needed for photon absorption. Thus, the photo excitons need to travel only a short distance resulting in the fast response of the device. Also, fast electron-hole separation, low recombination rate and high charge mobility properties of the hybrid inorganic perovskites are similar to inorganic semiconductors

(e.g. Si). All these qualities make them very attractive for sensing, photodetection and other optoelectronic applications. Table 1.3. shows a list of perovskite materials, their deposition method, and the sensing wavelength.

Table 1.3. Perovskites used for photodetector application.

Perovskite	Deposition methodology	Sensing wavelength of illumination (nm)	Reference
$CH_3NH_3PbI_3$	Drop casting	310-780	[117]
$CH_3NH_3PbCl_3$	Inverse temperature crystallization	365	[118]
$CH_3NH_3PbBr_3$	Antisolvent vapor-assisted crystallization	380-600	[119]
$CsPbBr_3$	Inverse temperature crystallization	410-570	[120]
$Cs_3Bi_2I_6Br_3$	Spin coating	300-600	[121]
$Cs_3Bi_2I_9$	Spin coating	450-950	[122]
$CsBi_3I_{10}$	Spin coating	650	[123]
$MA_3Bi_2I_9$	Spin coating	400-700	[124]
Ag_2Bi_{I5}	Spin coating	350-800	[125]
$Cs_2AgBiBr_6$	Spin coating	510-900	[126]
$Cs_3Cu_2I_5$	Spin coating	300-370	[127]
$CH_3NH_3SnI_3$	Thermal evaporation	900	[128]
$(CH_3NH_3)_3Sb_2I_9$	Drop casting	460	[129]
$(AG_3Bi_2I_9)$	Spin coating	405-700	[130]
$AgBiI_4$	Spin coating	UV 390	[131]
Ag_2BiI_5	Spin coating	UV 390	[131]
$AgBi_2I_7$	Spin coating	UV 390	[131]
$(H2MDAP)BiI5$	Slow evaporation	X-Ray	[132]
Cs_2AgSbX_6 (X= Cl, Br or I)	Surfactant assisted method	325	[133]

MA$_3$Bi$_2$I$_9$	Seed-crystal-assisted constant - temperature evaporation method	X-Ray	[134]

As mentioned earlier, recent works related to iodobismuthates gave birth to new promising materials such as silver bismuth iodides(SBIs) and copper bismuth iodides (CBIs). As a new family of compounds, the silver bismuth iodides are Ag$_3$BiI$_6$, Ag$_2$BiI$_5$, AgBiI$_4$, and AgBi$_2$I$_7$, which are formed on the basis of the variation in the AgI and BiI$_3$ ratio. The first photovoltaic device of this new class of compounds is employed on AgBi$_2$I$_7$ perovskite by Sargent et *al.* in 2015, where they obtained a PCE o 1.22% for the best cell[89]. Their work motivated others to focus more on these lead-free SBIs. In this thesis, a lot of efforts have been invested in understanding the structure, phase, morphology, elemental composition and optoelectronic properties of silver bismuth and copper bismuth halide perovskites. Also, the optimization of the experimental conditions for copper bismuth iodide perovskite is the hard-core part of the thesis because no reports related to the Cu$_2$BiI$_5$ perovskite have been available so far. Many investigations based on the silver bismuth iodide perovskites have been reported. In 2016, Zhu et *al.* synthesized Ag$_2$BiI$_5$ by varying AgI, BiI$_3$ ratio and investigated its effect on their photovoltaic properties and reported a PCE of 2.1%[90]. In 2017, Harry et *al.* prepared silver deficient AgBiI$_4$ cubic-defect spinel structure with an indirect bandgap of 1.63 eV. Later, Turkevych et *al.* carried out systematic structural and optoelectronic properties studies of these SBIs where they concluded that the AgI rich compound, Ag$_3$BiI$_6$ is the most attractive light absorber with a PCE of 4.3%[135]. It indicates that the SBI compounds are promising light absorber materials since their PCE jumped from 1.22 to 4.3%. During this rapid development of silver bismuth iodides, copper also grabs more attention as an alternative to Pb. Like Pb, Cu is a divalent cation, which is abundant on the earth. Its non-toxic behavior and high charge mobility grab its novelty in the replacement of lead[42,136]. It leads to the formation of another class of iodobismuthates: Cu-Bi-I. In 2018, Zhaosheng et *al.* synthesized a new compound, CuBiI$_4$ by solution processing method. In their study, CuI and BiI$_3$ powders were dissolved in DMA solvent and HI acid which was then spin coated and annealed at low temperature. They obtained a wide bandgap value of 2.67 eV with a cell efficiency of

0.88%[95]. So far now, no reports have been published for the Cu_2BiI_5 perovskite. Thus, silver and copper bismuth halide perovskites are potential candidates for optoelectronic and solar energy harvesting applications.

1.8. Hypothesis

Highly stable silver bismuth and copper bismuth halide perovskites with varying optical and electrical properties are formed by combining spin coating and thermal evaporation methods and post-deposition treatments.

1.9. General Objective

The general objective is to develop silver bismuth iodide and copper bismuth iodide perovskite thin films for optoelectronic applications.

1.10. Specific objectives

Specific objectives of the study are to,

- Synthesize silver iodide and bismuth iodide (AgI and BiI_3) powders.
- Fabricate BiI_3, AgI and CuI thin films and develop a photodetector device based on BiI_3.
- Fabricate antimony iodide (SbI_3) thin films and investigate the effect of iodization time, Sb_2S_3 deposition times on its properties.
- Develop a photodetector device based on SbI_3.
- Fabricate silver bismuth iodide (SBI) and copper bismuth iodide (CBI) perovskite thin films.
- Investigate the effect of precursor concentrations and annealing temperature on the properties of the perovskites.
- Evaluate the structure, morphology, elemental composition and optoelectronic properties of SBI and CBI perovskite thin films.
- Develop photodetector devices based on SBI and CBI perovskites.
- Investigate the stability of perovskites under ambient air and light irradiation.

1.11. Justification

Semiconductor optoelectronic devices have become a part of our daily life. Lead-based-perovskite devices have been used for the optoelectronic applications due to their remarkable optoelectronic properties. When considering the toxicity and impact on the environment, lead must be replaced by non-toxic elements. Thus, many semiconductor materials have been explored and there comes the role of bismuth. Bismuth has similar optoelectronic properties of lead. This facilitates the consideration of bismuth as a suitable candidate for optoelectronic applications. Further, it is more stable and less toxic compared to lead. The perovskites based on iodobismuthates have shown considerable attention within a short period. Their optoelectronic properties can be easily tunable by introducing metal cations into its crystal structure. This study focuses on the synthesis and characterization of silver bismuth iodide and copper bismuth iodide perovskite thin films for the optoelectronic applications.

Chapter 2
Experimental methods

This chapter describes all the experimental techniques used and the procedures followed to synthesize precursor powders, their films and perovskite films. For the fabrication of thin films, we used spin coating, thermal evaporation, and chemical bath deposition methods. For the structure, morphology, elemental composition, and optoelectronic properties studies X-Ray diffraction (XRD), Raman spectroscopy, Scanning electron microscopy (SEM), Energy dispersive X-Ray spectroscopy (EDS), X-Ray photoelectron spectroscopy (XPS), UV-Vis-NIR spectroscopy are used. A detailed discussion about the characterization techniques used is summarized.

2.1. Precursor material synthesis

2.1.1. Bismuth iodide (BiI$_3$)

BiI$_3$ powder was prepared in our laboratory by coprecipitation method. For that, we used salts of Bi(NO$_3$)$_3$·5H$_2$O (Fermont 99.0 %), and KI (Fisher chemical 99.2%). Using a filter paper, the precipitate of bismuth iodide was filtered and washed using deionized water. The filtered precipitate was heated at 120 °C for 1 h in a furnace and dried overnight. Dark brownish powder of bismuth iodide was crushed, powdered finely, and stored in a vacuum desiccator for future purposes.

2.1.2. Silver iodide (AgI)

Silver iodide power was synthesized using the salts of AgNO$_3$ (Fermont 99.1%) and KI (Fisher chemical 99.2%). Co-precipitation method was employed for the preparation of powder. AgI powder with light yellow color was formed as precipitate and it was heated in a furnace at 120 °C for 1 h to remove the water content.

2.2. Synthesis of binary iodide thin films and perovskite thin films

2.2.1. Bismuth iodide (BiI$_3$) thin film

BiI$_3$ thin film was prepared by spin coating BiI$_3$ solution on the well-cleaned glass substrates. For this, BiI$_3$ powder was first subjected for heating in a furnace at 120 °C for 30 minutes. This process helped to get uniform thick films since the heating removed the moisture present in precursor powder. BiI$_3$ solution was prepared by dissolving BiI$_3$ powder of 1 M concentration in dimethylformamide (DMF, Fermont 99.9%) (of volume 8 ml) using a continuous stirring system. Once the solution was mixed well in the solvent, it was heated at 70 °C for 1 h. After that spin-coating was done (4000 rpm for 30 s) on the premium glass substrate. Annealing was carried out at a temperature of 140 °C (30 minutes, sealed at 100 mTorr).

2.2.2. Antimony iodide (SbI$_3$) thin film

SbI$_3$ thin films were fabricated by the iodization of chemically deposited antimony sulfide[137,138] thin films (Sb$_2$S$_3$). For the preparation of Sb$_2$S$_3$ thin film, 0.325 g of antimony chloride (SbCl$_3$) was weighed in a glass beaker and dissolved in 1.2 mL acetone (CH$_3$COCH$_3$). Into that, 12.5 mL of sodium thiosulfate (Na$_2$S$_2$O$_3$.5H$_2$O,99.99%, 1M) and 32.5 mL of deionized water were added one after another and stirred well. The whole solution was poured into a glass beaker. Then, well-cleaned glass substrates were kept vertically into the whole solution. The deposition temperature of bath was kept at 25 °C and deposition was done for different durations like 30 min, 1 and 2 h. After that, these Sb$_2$S$_3$ thin films were iodinated for 30, 60, 90, 120, 150 s, and 5 min by exposing them to iodine vapor (iodine powder (1 g) heated at 100 °C). Schematic representation for the fabrication of SbI$_3$ thin films has given in Figure 2.1.
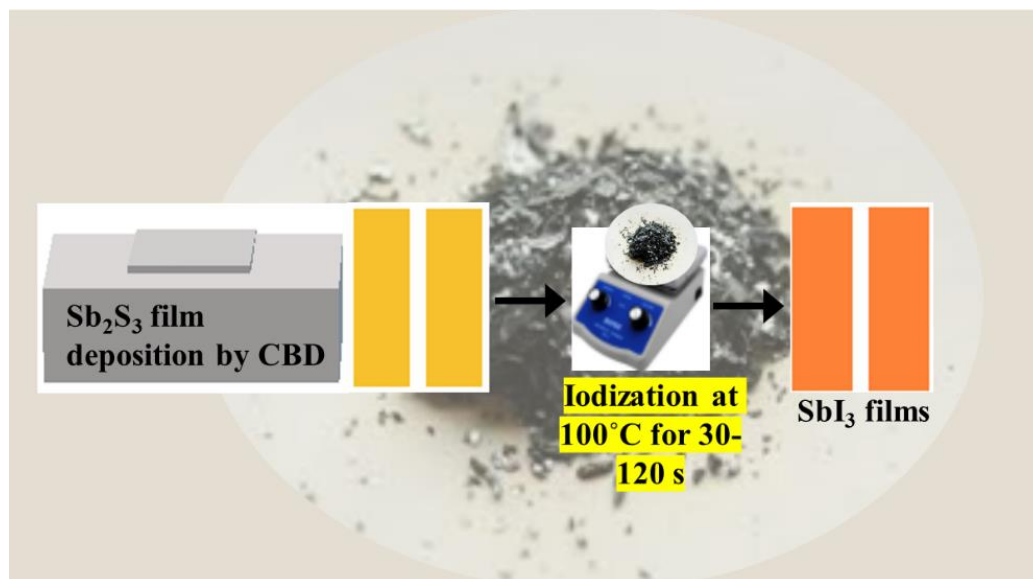
Figure 2.1. Schematic representation for the fabrication of SbI$_3$ thin films by rapid iodization process.

2.2.3. Copper iodide and silver iodide (CuI and AgI) thin films

A two-step method was employed for the fabrication of CuI and AgI thin films. Copper and silver of various thickness were evaporated individually on cleaned glass substrates by thermal evaporation method. These metallic thin films were subjected to iodization by enclosing them in a closed chamber containing iodine vapor. A vacuum thermal evaporator (Torr International, model number THE2–2.5 kW-TP) is used to fabricate silver/copper thin films using silver/copper wire of 99.99% purity. Perfectly cleaned glass substrates were fixed on the sample holder of the thermal evaporator equipment. We did the evaporation under a high vacuum of the order of 10^{-6} Torr. Substrate rotation of 20 rpm was used during the thin film deposition process, and the film deposition rate was 20 Å/s. Iodization was done at 100 °C (60 s) for various Ag/Cu thicknesses (10, 50, 80, and 100 nm). The reaction mechanism is explained using the following solid-gas type chemical reaction,

$$2\,M(solid\,) + I_2(gas) \rightarrow 2\,MI(solid)$$
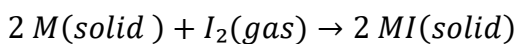
Where M is the respective metal.

2.2.4. *Silver bismuth iodide (Ag₂BiI₅) thin film*

Silver bismuth iodide (Ag$_2$BiI$_5$) was synthesized using bismuth iodide and silver iodide powders that we already synthesized in our laboratory. Solution processing method was employed where we varied the BiI$_3$ concentrations from 0.45 to 1 M, keeping the AgI concentration as a constant (1M). Spin coating solution was prepared by two steps. Firstly, the precursor powders of all molar concentrations were mixed well and heated in an air furnace at 120 °C for 15 minutes to remove excess water content. In the second step AgI and BiI$_3$ powder mixture was dissolved in dimethylformamide (DMF, 8 ml). For that the solutions were subjected to continuous heating and stirring. Heating of the solution was done at 70 °C for 1 h in an open atmospheric condition. The experiment was done under ambient conditions. After that, the solution was taken in a micropipette and spin-coated (4000 rpm for 30 s) on the glass substrates in ambient air followed by heat treatment at 140 °C for 0.5 h (sealed at 100 mTorr). The fabrication of SBI perovskite thin films are schematically represented in Figure 2.2.
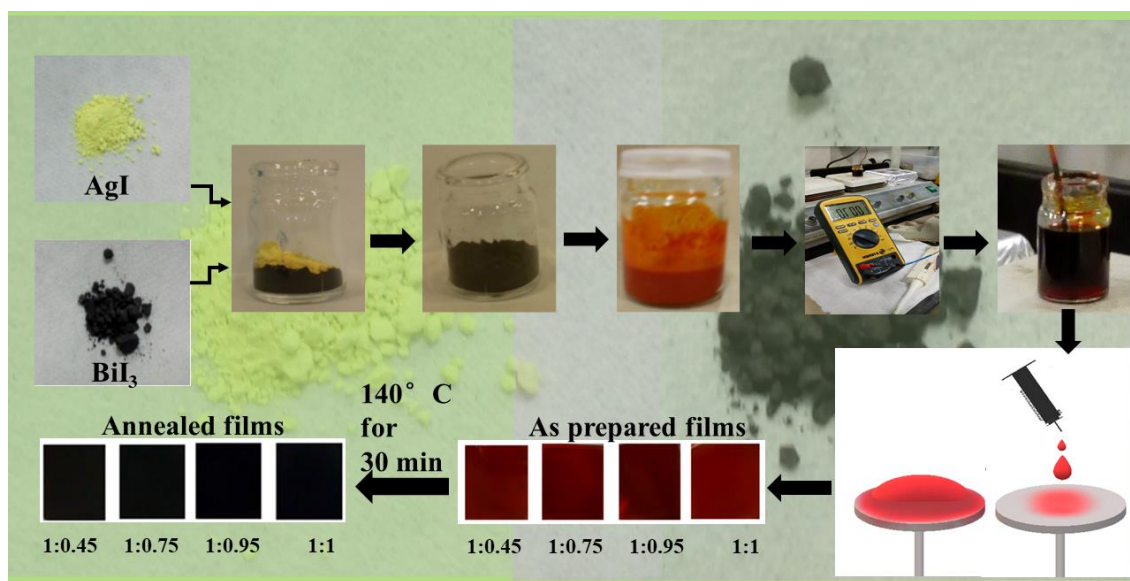
Figure 2.2. Schematic representation for the synthesis of silver bismuth iodide films by solution processing spin coating method.

2.2.5. *Copper bismuth iodide (Cu₂BiI₅) thin film*

Copper bismuth iodide films were deposited using spin coating followed by thermal evaporation method. We incorporated Cu into spin coated BiI_3 thin film via thermal evaporation method. For that copper of varying thicknesses (10, 50, 80, and 100 nm) were deposited onto the spin coated bismuth iodide thin film (which was synthesized as explained in section 2.2.1). Copper deposited bismuth iodide films were annealed at 100 °C for 30 min (sealed at 100 mTorr). Films were taken out at room temperature.

2.3. Thin film deposition techniques:

2.3.1. *Spin coating method*

Spin coating is one of the simplest and dominant methods for the fabrication of uniform films with thickness ranging from nanometers to micrometers. Emil et *al*. were the first who performed spin coating more than fifty years ago where they considered the spreading of Newtonian fluid on a planar substrate rotating with a constant angular velocity. Spin coating was first done for the coating of paint and pitch[139]. It starts with the dilution of the desirable material that must be coated in the appropriate solvent. The solution is then spread over the entire surface of the desired substrate. There are four stages involved in the spin coating process for the fabrication of thin films and are illustrated in Figure 2.3. The stages are,

- Fluid dispenses
- spin-up
- stable fluid outflow
- evaporation

After spreading the solution, the substrate spun at high speed. Most of the experiments involve the deposition of a few drops of fluid onto the center of a substrate followed by spinning the substrate at high speed typically around 3000 rpm. The centrifugal force causes the solution to flow radially outward. Because of the viscous force and surface tension, the thin film is retained on the flat substrate. The outward liquid flow and evaporations cause the films to be thin. Various factors affect the thickness of the film:

27

spinning speed, surface tension, dispense volume, solution concentration, spinning time, and viscosity of the solution. The properties of film can be achieved by varying different parameters involved in the spin process. Stages three and four have the most impact on the final thickness of the thin films and are briefly described below.

Deposition

In this stage, the fluid dispenses over the substrate and the substrate is accelerated to desired speed. The centrifugal force causes the solution to spread over the substrate.

Spin up

Spin up is the second stage when the substrate is accelerated up to the desired rotation speed. In this stage the fluid is expulsed from the substrate surface due to the rotational motion. Spiral vortices may be present in this stage. It occurs due to the twisting movement caused by the inertia at the top of the liquid during the substrate rotation at a higher speed. Eventually, the fluid becomes thin which would be enough to corotate with the substrate. Finally, the substrate arrives at the desired speed and the liquid becomes thin enough so that viscous shear drag balances the rotational accelerations.

Stable fluid outflow

In the third stage of spin coating process, the substrate spins at a constant rate. This is the stage at which the gradual thinning of fluid takes place. Even if the solution contains volatile solvents the fluid thinning is relatively uniform, and one can see interference colors spinning off. Also, often one can see edge effects because the fluid uniformly flows toward the outward direction but there would be droplets at the edge. Thus, due to this reason, there may be a small thickness difference around the rim of the final substrate, and this depends on the surface tension, viscosity, rotation rate, etc.

Evaporation

Once the spinning off stage is over, the drying stage starts. In this stage, the centrifugal outflows stop, and solvent loss leads to further shrinkage. This leads to the formation of a thin film on the substrate. During this stage, solvent evaporation takes place because of the spinning of the substrate at a constant rate. The rate of evaporation depends on the

chemical potential of each solvent species between the bulk gas that flows nearby and the free surface of the fluid layer. During the evaporation process, dissolved species in the solvent may grow. Thus, to get a solid skin one should concentrate on the high viscous liquid.
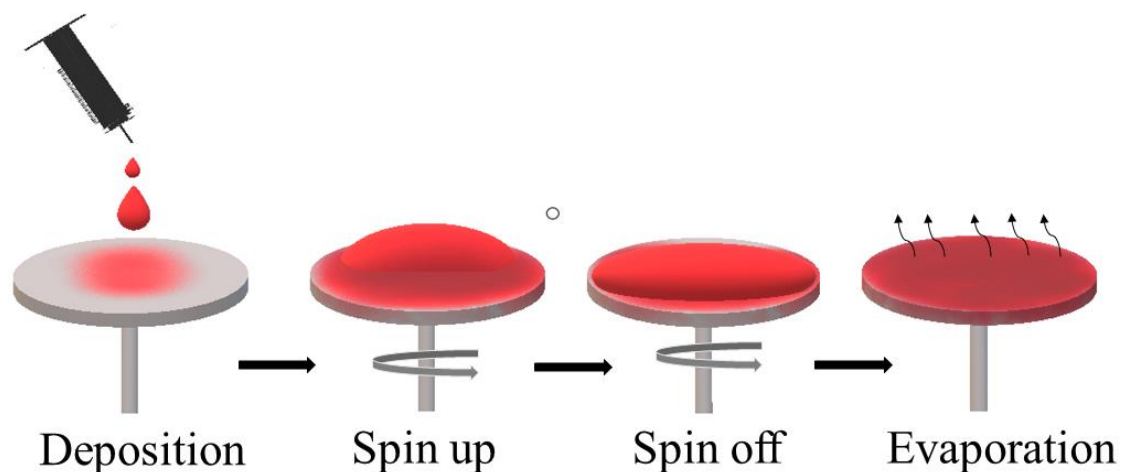
Figure 2.3. Different stages involved in spin coating process.

Like any other method, spin coating has advantages as well as disadvantages. One of the most significant benefits is effortless, fast, economical and no need for coupled process variables. The film's thickness is easily varied by changing the spin coating parameters such as viscosity, spinning time, spin speed, etc. If the film has become completely uniform, then it can remain so during the entire process. This technique can be considered one of the popular methods because a lot of information is available about the subject. As the substrate size increases, it is complicated to spin to get a uniform thin film. One of the disadvantages is materials wastage because only 2-5% of material is utilized for the film synthesis and the rest of 98-95% is wasted during the spinning process.

2.3.2.   Thermal evaporation method

The thermal evaporation method is one of the physical vapor deposition techniques (PVD). This technique is used to deposit thin films wherein a vacuum technology is used for the deposition of pure materials over the surface of the substrate or different materials. The resultant coatings are called films, which can be of the order of micrometers to

angstrom. They can be coated with a single material or a mix of materials as a double layer. Materials used for coatings in the thermal evaporation technique can be pure metals, non-metals, or molecules such as oxides and nitrides. The thermal evaporation process involves heating the desired solid material under high vacuum at high temperature. As a result, some vapor pressure is created inside the chamber. Relatively low vapor pressure can make a vapor cloud inside the chamber under vacuum. As a result, evaporated material forms a stream of vapor and it goes to every corner of the chamber. Then, it reaches the substrate and gets deposited onto it as a film. In the thermal evaporation process, material that must be coated on the substrate is heated to its melting point and turns into liquid form. Hence the material holder is always designed at the bottom of the chamber. Sample holder is always facing down towards the heated source material to receive the coating.

It is possible to control the film thickness by assigning programs to the equipment (evaporation rates or using thickness sensors/monitors (quartz crystals)). Films with uniformity are one of the significant advantages of this method. Filament evaporation is a simple method of resistive heating of the filament for the melting of source material. It can have various physical configurations and often called boats. These boats are made of suitable metals with high melting points (tungsten, tantalum, molybdenum etc.), and the source material is placed on these boats for coating purposes. These filament boats offer safety for working at low voltages even though the current is high. Figure 2.4 shows a basic schematic of the thermal evaporation process.
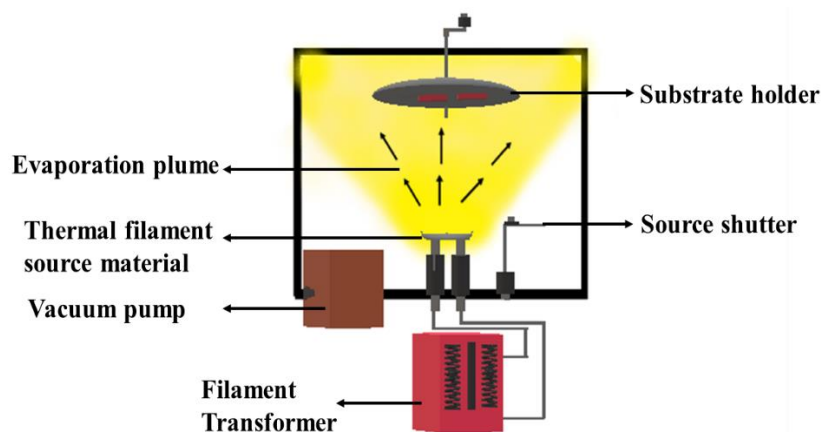
Figure 2.4. Schematic diagram of a thermal evaporator.

30

2.3.3.   *Chemical bath deposition (CBD) method*

In a chemical bath deposition system, well-cleaned substrates are immersed in the precursor solution. Two processes that take place in chemical bath deposition and they are nucleation and film growth. Different parameters affect the deposition process are deposition duration, the temperature of the bath, pH of the precursor solution, and molarity.

2.4. Device fabrication

The photodetector device was fabricated on glass substrates. For that, the material was deposited first, and then Ag electrodes were painted as metal contacts. The photodetectors were illuminated with different wavelengths of LEDs of power 50 W and tungsten lamp at a given bias voltage.

2.5. Characterization techniques

2.5.1.   *X-ray diffraction (XRD)*

X-ray diffraction (XRD) is used for determining the crystal structure of materials. The wavelength of X-ray is comparable with the interplanar distance of a crystal. When an incident beam of X-rays interacts with a sample, it will be scattered in different directions. Atoms in the crystal planes act as a periodic array of coherent scattering centers. As a result, diffraction occurs and the diffraction pattern contains information about the atomic arrangement within the crystal. Bragg's law explains X-Ray diffraction in crystalline materials and it can be written as,

$$n\lambda = 2d_{hkl}Sin\theta \qquad (7)$$

where λ is the wavelength of incident X-rays, n is an integer, d_{hkl} is the interplanar distance between the hkl planes and θ is the angle of incidence[140]. When two parallel rays of X-rays incident on the sample and diffracted, they interfere constructively and their path difference must be equal to integral multiple of the wavelength. According to Bragg's law, as the interplanar distance varies, the incidence angle also varies for a constant

wavelength. In the XRD pattern, peak intensities are corresponding to the respective atomic positions. From the XRD pattern, one can calculate the crystallite size using the Scherrer equation, which is given by,

$$D = \frac{0.9\lambda}{\beta Cos\theta} \qquad\qquad (8)$$

where D is the crystallite size and β is the full-width half maximum of the peak (FWHM). In this work, X-ray diffraction patterns of the samples were recorded in the normal mode in the range of 2θ = 10-60° by using Empyrean PANalytical diffractometer (Cu-Kα radiation with wavelength, λ=1.54056 Å). The XRD patterns were compared with the standard JCPDS files and crystal structures were determined.

2.5.2.   *Raman spectroscopy*

Raman spectroscopy is based on the Raman effect. When a particle is irradiated with a frequency, the radiation will be scattered by the molecule. It contains the incident photons with the same frequency and other frequency components whose frequency is shifted from that of the incident radiation. In every detail, the scattered light consists of a very strong beam which has the same frequency as the incident light (elastically scattered photons) and the process is called Rayleigh scattering. The other process is called Raman scattering which is composed of the weakest signal and has a frequency greater than or less than that of the incident light (inelastically scattered photons). We measure the vibrational frequency which has the shift from that of incident light's frequency. Thus, Raman spectra give a detailed information about the molecular vibrations, structure, and phases present in a sample[141]. All the Raman spectra were collected using Thermo Scientific DXR™ 2 Raman Microscope employed with a 532 nm laser wavelength of excitation. The data were collected from the wavenumbers ranging from 20-1500 cm⁻¹.

2.5.3.   *Scanning electron microscopy (SEM)*

SEM is used for getting information about the surface morphology, topographical and compositional studies (EDS associated with SEM) of materials. It uses a focused beam of high-energy electrons to extract information from the sample. When a beam of electrons

interacts with the sample, two types of interactions occur between the electrons and samples under scanning, they are elastic and inelastic interactions. Backscattered electrons (BSE) are produced when the incident electrons interact with electrons with comparable energy. Thus, BSE are due to the elastic interaction since electrons bounce back to their origin and retain their initial energy. When the electrons incident on the sample, they get decelerated and the energy is dissipated as various kinds of signals. These signals give various information about the sample under analysis. For example, secondary electrons which produce the SEM images (showing the morphology and topography of samples), backscattered electrons which illustrates the contrast in composition for multiphase samples. Here heavier elements appear as bright since they produce more BSE and lighter elements appear as dark. The inelastic collision of incident electrons with the electrons in the discrete shells of the atoms in the sample causes the generation of X-rays. SEM with EDS (energy dispersive X-ray spectroscopy) has been used in this work. EDS helps for elemental identification and composition by recording the characteristic X-rays of the specimen. Because each element has its characteristic X-rays and thus it can be differentiated. It helps to measure the concentration of constituent elements in a specimen[142]. In this work, the surface morphology of the samples was characterized using field emission scanning electron microscopy (FESEM) (Hitachi SU 8020) with different magnifications. Conductive silver colloid (silver paint) was used as contacts between the sample surface and the holder to get good-quality images and reduce sample charging effects.

2.5.4.   *X-ray photoelectron spectroscopy (XPS)*

The basic operation principle behind the functioning of XPS is the photoelectric effect (the emission of electrons when the sample is irradiated with light). The photoelectric effect was explained by Einstein where the light consists of small packets of energy called photons. Each photon has energy $h\nu$, where h is the Planck constant and ν is the frequency of radiation. The emission of electrons upon the irradiation of light is called 'photoelectric effect' and the electrons are called photoelectrons. The emission of electrons occurs only when it gets enough energy which is higher than the work function (φ). The photoelectrons kinetic energy is given by the following equation,

$$KE = hv - BE - \varphi \qquad (9)$$

where BE is the binding energy.

The XPS spectra are composed of intensity of photoelectrons detected versus binding energy and the BE values decrease from left to right. The signals from the core levels preserve their original binding energy values. The other inelastically collide electrons gives the background. An increase in the background with an increase in binding energy values results in lowering the signal to noise ratio. In XPS, it maps only the binding energy difference between the initial and final states, and it does not map any energies corresponding to the initial stage.

XPS analysis is widely used for getting information such as bonding nature and composition at the surface and interfaces. It is achieved by analyzing the compound's chemical environment and studying the shift in the core level electron binding energy, usually the term used for this is 'chemical shift.' Various approaches have been applied to measure the binding energy (BE) of a well-defined peak. A basic correction is applied to the peak. The most popular BE correction is adventitious carbon correction where C1s (284.6 eV) is used as the basic reference. The Fermi level edge must be at 0 eV with the BE scale so that there is good contact between the sample and the spectrometer. In other words, the Fermi level of the sample and the spectrometer should be in alignment, i.e., they should share a common Fermi level which becomes a natural reference level. It is possible only if there is enough density of states in the Fermi level of the sample then only sufficient charge transfer can occur. This is a serious problem for semiconductors and insulators because the deficiency of density of states at their Fermi level makes hard to predict whether the Fermi levels are aligned or not. Another issue is when the electrons leave the sample surface due to the photoexcitation, the holes must be refilled with negative charge otherwise the charge neutrality cannot be maintained, and this leading to the phenomenon of 'charging.' The charging effect causes all the core level BE shifted to higher BE values[143].

In XPS analysis, there is a notation that gives the core level signals and has the form, "*X nlj*". Here, X denotes the element, *n* denotes the principal quantum number, *l* is

the angular momentum quantum number, and j is the total angular momentum quantum number, which can be written as the sum of orbital quantum number and spin quantum number, i.e, $j = l \pm s$. When $l \geq 1$, the core levels of spin split doublets have of the form, $p_{3/2}$-$p_{1/2}$, $d_{5/2}$-$d_{3/2}$, $f_{7/2}$-$f_{5/2}$. Based on the degeneracy of each electronic level given by $2j+1$, the spin split doublets have their theoretical area ratios in the order 2:1, 3:2, and 4:3 for p, d, and f levels. The binding energy difference between these doublets denoted by ΔBE varies from a fraction of eV to several eV and depends on the radius of the respective orbital. In general, for a constant value of n and l the ΔBE increases with an atomic number for a given subshell and decreases as l increase for a given shell. Depending on the chemical environment, the binding energy and the area ratios are not constant for a given element. It varies for each element and depends on the nature of the chemical environment.

XPS is a fingerprint technique because each element has its own unique characteristic core level spectra. In the case of elemental analysis, to get all the species present in the sample, a survey spectrum is used. By performing high-resolution scans at the narrow region, we get the core level signals of the element under consideration. The width of the peak is not constant, and it varies from one element to another. The distribution of constituent elements till the depth of a sample can be studied from the depth profile analysis. In the depth profile analysis, the surface of the sample is etched using argon ions in each cycle of the etching process. Thus, the composition and uniformity of the sample can be studied from the analysis. In this work, the elemental composition and their chemical states were analyzed using X-Ray Photoelectron Spectrometer, Thermo scientific K-Alpha having a monochromatic X-ray source of Al-Kα (E=1486.68 eV).

2.5.5. *UV-Vis/NIR spectroscopy*

The optical properties of samples were studied using UV-Vis/NIR spectrometer. The baseline for the measurement was set by using a plane glass substrate as sample and reference. A standard reflector (supplied by the manufacturer) was used as the reference for the reflectance measurements. The optical bandgap (E_g) value of thin film was calculated using the equation;

$$(\alpha h\nu)^n = A(h\nu - E_g) \qquad\qquad (10)$$

where *A* is a constant, *α* is the absorption coefficient, *h* is Plank's constant, and ν is the frequency of the incident photon. The value of the exponent *n* depends on the type of optical transition, i.e., *n* = 2 for a direct allowed, *n* = ½ for an indirect allowed and *n* = 2/3 for a forbidden bandgap semiconductor respectively. The absorption coefficients α (cm^{-1}) of the films were calculated using the equation,

$$\alpha = \frac{1}{d} ln \left[\frac{(1-R)^2}{T} \right] \qquad\qquad (11)$$

where *T* is the transmittance, *R* is the reflectance, and *d* is the average film thickness (cm). The average thickness of the films was measured using a profilometer. Optical properties were studied from absorbance, transmittance and reflectance spectra of the thin films using a UV-Vis-NIR spectrophotometer (Jasco V-770).

2.5.6. *Electrical measurement*

The thin films' electrical properties were studied by measuring their photocurrent response and current-voltage (I-V) characteristics. For that, silver electrodes were painted and dried by annealing at 100 °C for 10 min. Keithley 6487 picoammeter/voltage source was used for the electrical measurements. The film was kept in the dark for 10 min to eliminate the noise. The photocurrent measurements were done using a tungsten lamp (50 W) and LEDs with different wavelengths. The measurements were done under both dark and illumination conditions. A 532 nm continuous laser was the light source for the photocurrent measurements at different laser power densities.

Chapter 3
Binary halides: studies on their properties

3.1. Introduction

Transition metal dichalcogenides, organic-inorganic hybrid halides, metal halogenides, and transition metal oxides are treated as outstanding materials for the investigations because of their optoelectronic and catalytic properties[144,145]. Compared to other materials, hybrid organic-inorganic halide perovskites are considered as potential candidates for the photovoltaics and optoelectronic applications[146,147]. Halides of bismuth, antimony and arsenic have been investigated for the past few decades and used in many fields such as semiconductor, nanotechnology, halogen metallurgy, and the medical field[148]. Iodides of bismuth and antimony such as BiI_3 and SbI_3, have a similar layered structure[149] and been employed for photovoltaics. The covalent bonds and van der Waals forces present in their structure hold these layers together. The rhombohedral structure of SbI_3 contains eight atoms and it has high photosensitivity and intrinsic optical anisotropy[150,151]. Also, they have a high refractive index and show second harmonic generation[152,153]. Because of these properties, it has been widely used for applications such as cathodes in information storage, solid-state batteries, high-resolution image micro recording, etc.[154,155]. It has not yet explored much, and more investigations are necessary to make them useful for photovoltaic and optoelectronic applications.

Over the past decades, transparent conducting materials (TCMs) have attained considerable attention. For example, copper iodide (CuI) and silver iodide (AgI) are among them and known as superionic conductors. They have made their signatures for chemical sensor and ionic conductor applications[156]. To bring them more for their applications in the electronics field, their electrical and chemical properties must be understood. To achieve this, a detailed study of their characterizations is very important

for a better understanding of their fundamental structural and chemical properties for the future applications.

AgI is well-known as a solid electrolyte with high ionic conductivity[157] and photosensitivity. It is used in photographic films, photocatalysis and cloud condensations applications[158,159]. They have not been investigated much for electronic applications since they are less stable towards open atmospheric conditions[160]. There are three polymorphs for AgI, namely α-AgI, β-AgI and γ-AgI. Here α-AgI has bcc structure, the second phase has a hexagonal structure and the third phase has an fcc structure. Among them β-AgI and γ-AgI are most stable at ambient pressure[161]. β-AgI has high ionic conductivities with n-type conductivity. Copper iodide (CuI) is a well-known transparent semiconductor and has high p-type conductivity. Copper vacancies are the reason behind their high p-type conductivity. This makes them suitable for applications such as hole transport layer in solar cells, field emission displays, organic catalysts[162,163], and optoelectronic devices[164,165]. Like AgI, there are three crystal phases for CuI, namely, α-CuI (fcc structure), β-CuI (hexagonal structure) and γ-CuI (fcc structure)[166–169]. Compared to other phases, γ-CuI is treated as the most important one for optoelectronic applications because of its solution processability at room temperature[170]. This chapter describes the synthesis and detailed characterizations of metal halides namely, BiI_3, SbI_3, AgI, and CuI.

3.2. Fabrication of bismuth iodide thin films for photodetector application

3.2.1. *Results and discussion*

3.2.1.1. *Structure*

Crystal structures of BiI_3 powder and thin film were examined by analyzing the respective X-Ray diffraction patterns. BiI_3 powder shows reflections from (003), (113), (116), (300), (119), (223), (226), (309), (413), (3012), and (416) planes. It (given in Figure 3.1) has rhombohedral phase and is consistent with the standard database: JCPDS # 48-1795.

Figure 3.2 shows the XRD patterns of BiI_3 thin films. We observed well-defined reflections from (003), (006), (113), (116), (009), (300), and (0012) planes correspond to the diffraction angle at 2θ = 12.782°, 25.727°, 26.981°, 35.251°, 39.099°, 41.564°, 43°,

and 52.946° respectively. These results agree with the rhombohedral phase for BiI_3 (space group R-3, JCPDS # 00-048-1795). After annealing the diffraction peak intensities increased and this might be due to the improvement in the crystallinity[171–173].
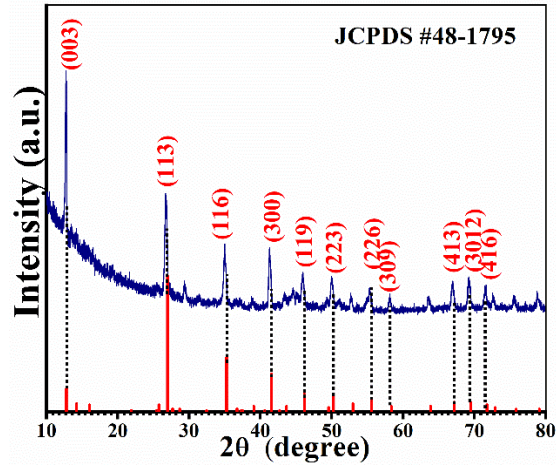
Figure 3.1. PXRD patterns of BiI_3 powder.
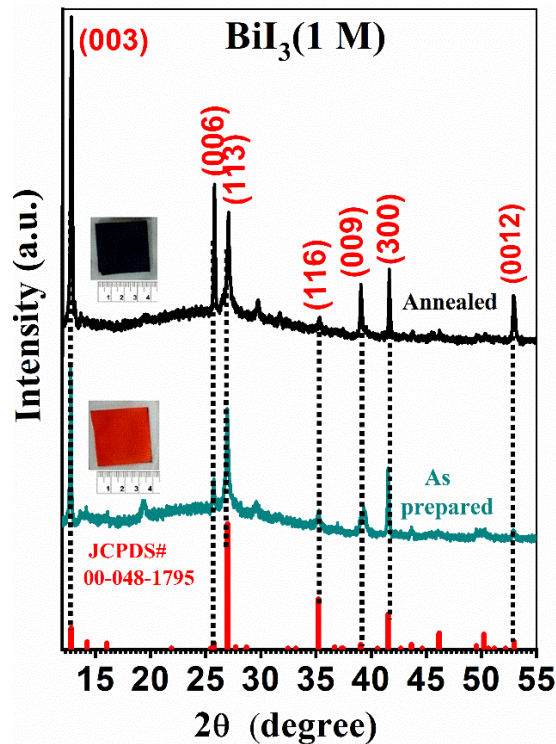
Figure 3.2. XRD patterns of as prepared and annealed BiI_3 thin films.

3.2.1.2.*Structure and phase*

The molecular structure of precursor powder is elucidated using the respective Raman spectrum. Figure 3.3 shows the Raman spectrum for BiI_3 powder. We observed Raman peaks at 54, 73, 90, 110, and 155 cm^{-1}. Raman active modes corresponding to these peaks are E_g, A_g, E_g, A_g, and A_g[174,175]. According to literature [174,175], the line at 155 cm^{-1} probably arise from second-order Raman peak.
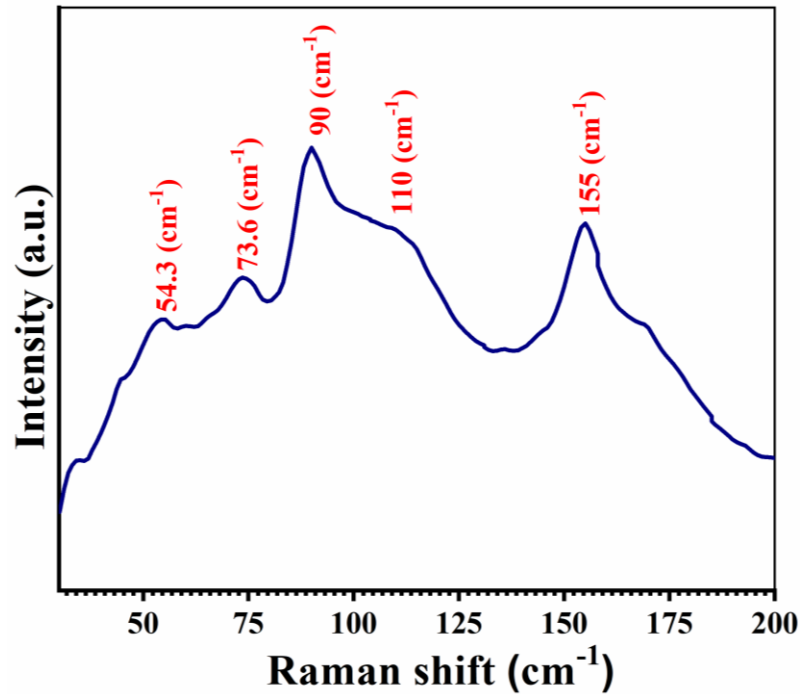
Figure 3.3. Raman spectrum of BiI_3 powder at room temperature.

Figure 3.4 illustrates the Raman spectrum for annealed BiI_3 film of 1M concentration. Four Raman active modes are observed at 50, 86, 104 and 150 cm^{-1}. Among these lines, the two prominent peaks are situated at 86 and 150 cm^{-1}. The former peak corresponds to the E_g mode [174,175]. The second intense line at 150 cm^{-1} may arise due to the second-order Raman line which is only observed in bulk materials[174,175]. In addition to these major peaks, there exist minor peaks positioned at 50 and 104 cm^{-1}. These two lines are corresponding to A_g Raman active mode and similar results are observed in the literature related to BiI_3[174,175].
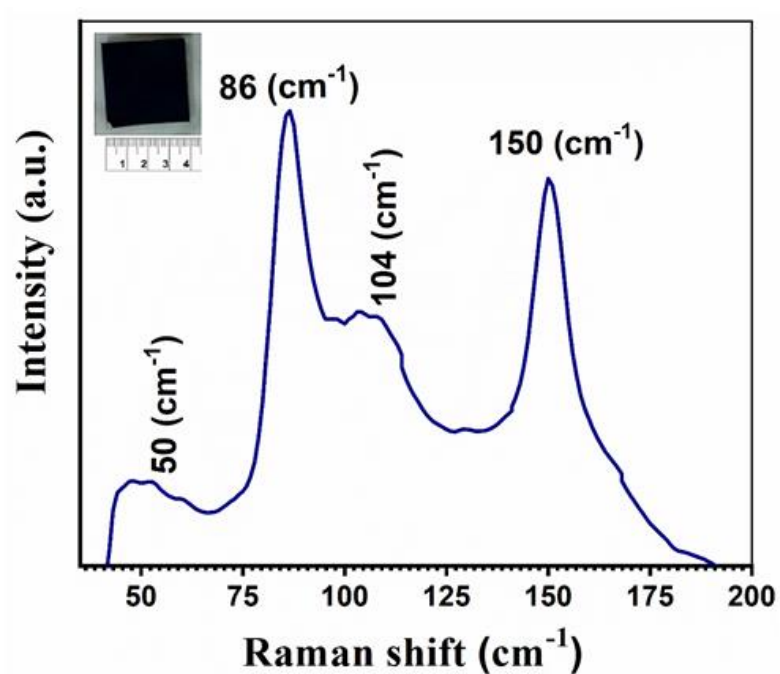
Figure 3.4. Raman spectrum of BiI₃ film.

3.2.1.3. *Morphology*

Surface morphologies of BiI₃ thin films are captured using FESEM and are given in Figure 3.5. 5 kV was the applied acceleration voltage and images were taken in the secondary mode (for magnifications of 10 and 25 k).
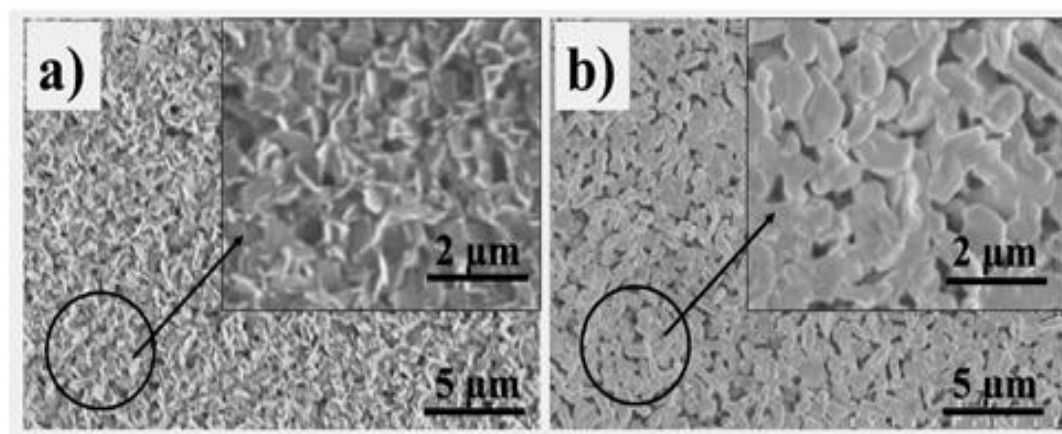
Figure 3.5. SEM images of BiI₃ film of 1 M concentration a) as deposited film and b) heat-treated film.

41

The morphology of as-prepared film is composed of densely arranged, irregularly shaped particles. The particles are appeared as planes pointing outwards. After annealing, the film surface gained a new morphology as in Figure 3.5 (b). Here, the surface morphology is consisted of small rod-shaped particles and voids are observed.

3.2.1.4. *Chemical state and composition*

Surface analysis of BiI_3 powder and the thin film were studied from the survey spectrum and high-resolution spectra using XPS.
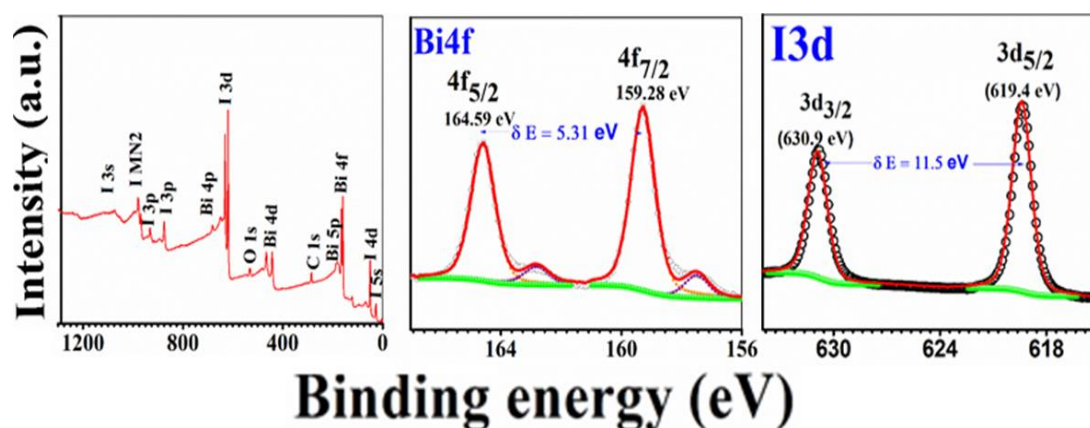
Figure 3.6. Survey spectrum and high-resolution spectra of Bi 4f and I 3d for BiI_3 powder.

Figure 3.6 corresponds to the survey and high-resolution spectra for BiI_3 powder. The core-level spectrum for Bi 4f consists of two doublets. Peaks at 159.28 eV and 164.59 eV correspond to the Bi^{3+} in BiI_3[176–178]. The high-resolution spectrum for I 3d consists of two peaks at binding energies 619.4 eV and 630.9 eV. These peaks are separated by an energy difference of 11.5 eV and correspond to I⁻ in BiI_3[176,177]. Figure 3.7 shows XPS analysis for BiI_3 film.

In the survey spectrum, C, O, Bi, and I species are detected. The high-resolution spectra consist of core level spectrum, deconvoluted peaks and the envelope (which is resulted after the deconvolution process and peak fitting). Bi 4f spectrum has two major peaks with B.E. values, at 159.29 eV and 164.6 eV are corresponding to +3 state of Bi in BiI_3[176–178] (shown in Figure 3.7(b)).
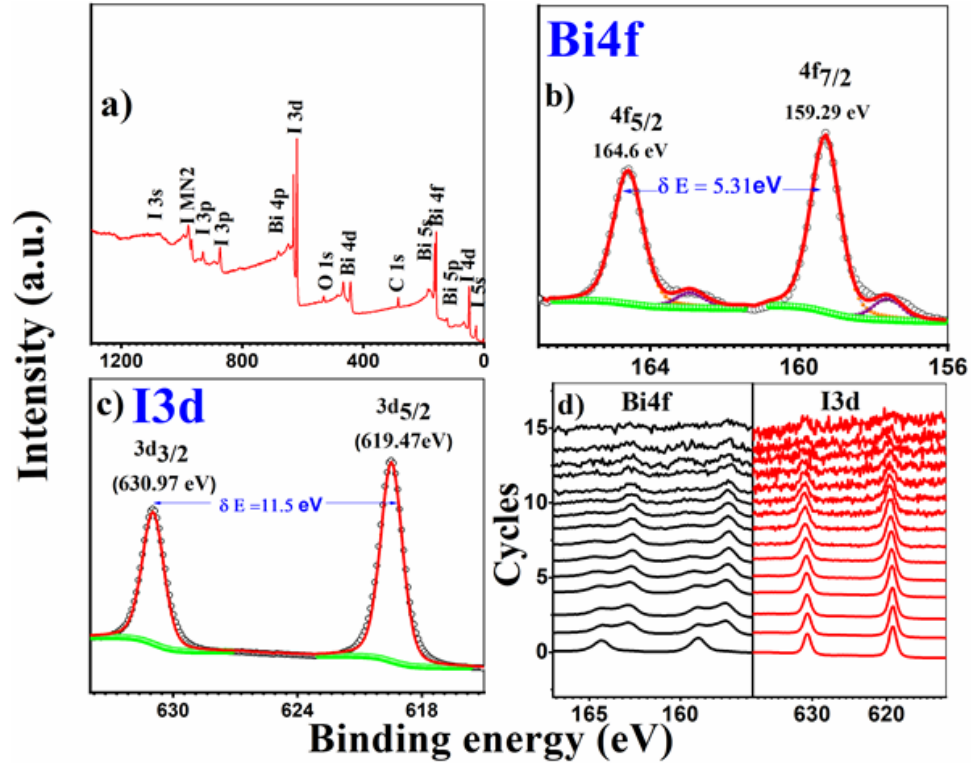
Figure 3.7. Survey spectrum, high-resolution spectra and depth profile of BiI₃ film.

All the peaks within the core region are maintained at an energy difference of 5.31 eV. One pair of Bi 4f levels with low intensity appear at 157.61 eV and 162.92 eV and are corresponding to elemental bismuth. I 3d high-resolution spectrum is composed of (presented in Figure 3.7 (c)) two peaks at 619.47 eV and 630.97 eV (with peaks binding energy difference of 11.5 eV), are belonging to I⁻ state in BiI_3[176]. To see how the elements are distributed till the depth of the film, a depth profile analysis was conducted and is presented in Figure 3.7 (d). During the analysis, BiI_3 was removed by etching from the sample using Argon ions. Due to Ar^+ etching, after one cycle of etching process, presence of metallic bismuth was found. The elements: Bi and I are uniformly distributed to the 11th level of the film. After the 11th level, the elements are not enough to produce a strong signal indicating that the incoming signal has reached the substrate surface.

3.2.1.5. *Optical properties*

Absorbance spectra of pristine and annealed films of BiI_3 of 1 M concentration are given in Figure 3.8. The as prepared film shows a keen absorption around 600 nm. After annealing, we observed a higher optical absorption around 720 nm. The optical bandgap (E_g) values of the as prepared and annealed films are estimated from Tauc plots. Direct bandgap values of 2.15 eV and 1.75 eV are obtained for the as prepared and annealed films respectively (shown in the inset). The reduction in the bandgap value might be attributed to the improvement in the crystallinity and the larger particles that we see in the diffraction pattern and morphology of the annealed film. The energy range was taken in agreement with the absorption range of the absorption spectrum. The decrement in the bandgap might be due to the improvement in crystallinity of the sample after annealing (see Figure 3.8). The bandgaps obtained are close to the corresponding reported values of BiI_3[179–181]. We observed that a strong noticeable peak appears around 500-585 nm in the as prepared film and after annealing, this peak appears around 600-685 nm. Similar peaks are observed in the previous works related to the iodide compounds and are ascribed as the exciton peaks[182].
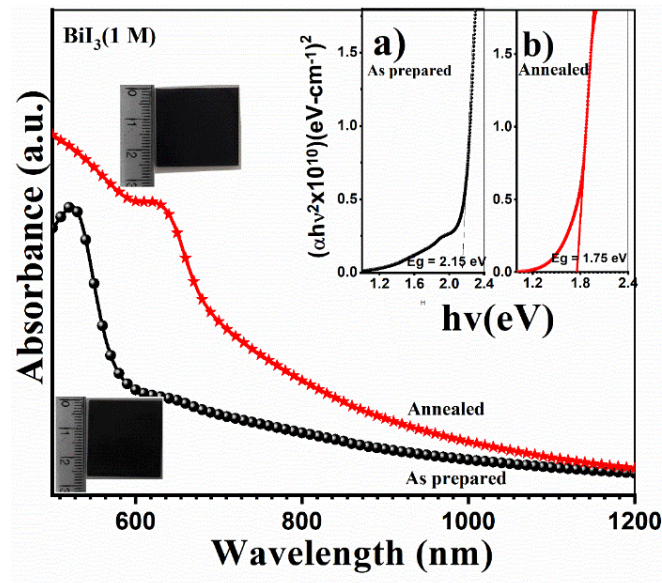
Figure 3.8. UV-Vis absorption spectra of as prepared and annealed BiI_3 films (Tauc plots for the films are given in inset).

3.2.1.6. *Electrical properties*

For the fabrication of the BiI$_3$ photodetector, we painted Ag electrodes of dimensions 5×5 mm as shown in Figure 3.9 (a). Tungsten lamp and LEDs with different wavelengths (with a power of 50 W) were used to illuminate the device for the photocurrent response measurements. Interestingly we observed an increase in photocurrent when the light sources were switched on. I-V characteristics are shown in Figure 3.9 (b) and the linear and symmetric behavior ensures a relatively high-ohmic contact between electrode and bismuth iodide.
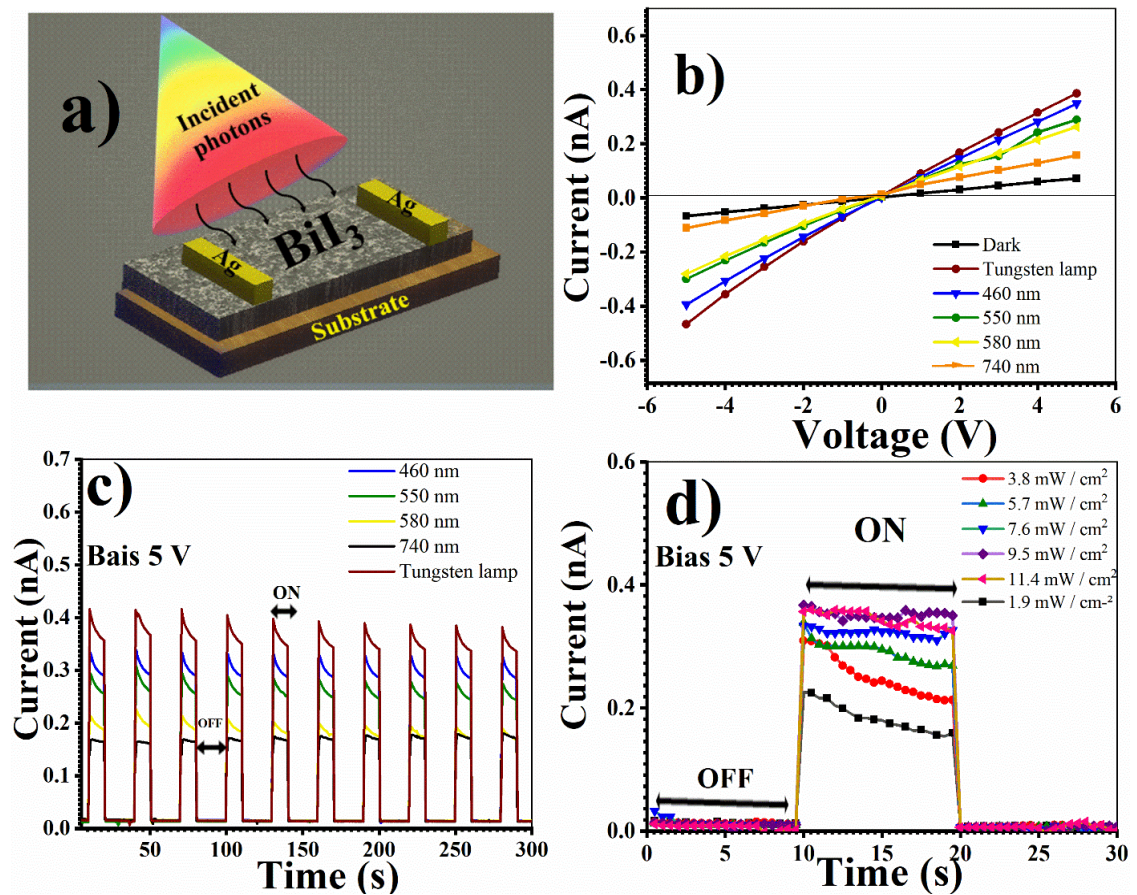
Figure 3.9. a) Schematic diagram, b) I-V characteristics c) switching behavior of BiI$_3$ photodetector when illuminated with different wavelengths of LEDs (at a bias voltage of 5V), and d) photocurrent response towards the light with various power densities (when illuminated with 532 nm laser).

The photocurrent response of BiI_3 photodetector under dark and light is shown in Figure 3.9 (c). When the photodetector was illuminated with light, we observed a sudden increase in photocurrent compared to the dark current. This increment in current is resulted due to the photogenerated carriers when BiI_3 absorbs the incident photon energy. In addition, the reproducibility and stability of the device must be noted. It could easily attain a stable high value of photocurrent and come back to a low value of photocurrent when the light is repeatedly turned on and off. If I_{light} and I_{dark} are the photocurrents under light and dark, then the sensitivity of a photodetector can be calculated. The sensitivity towards different wavelengths of light was calculated using the following equation[104],

$$S \% = \frac{I_{light} - I_{dark}}{I_{dark}} \text{x} 100 \qquad (12)$$

It is one of the most important parameters to determine the quality of a photodetector. Sensitivity versus wavelength of light is given in Figure 3.10 (a). The photocurrent response was measured for various power densities using a continuous 532 nm laser and is given in Figure 3.9 (d). We observed that the photocurrent response of detector increases with the light intensity. Thus, to investigate the photocurrent response as a function of power densities, we calculated responsivity (R). It is one of the important parameters of a photodetector that can state the quality of a photodetector. It is defined as the amount of photocurrent generated per unit area per unit light intensity and can be calculated using the equation[13],

$$R = \frac{I_{light} - I_{dark}}{L_\lambda S} \qquad (13)$$

Here L_λ is the power density (1.9, 3.8, 5.7, 7.6, 9.5, and 11.4 mW/cm^2) of the light source and S is the area of the electrode. We plotted responsivity as a function of incident power density (shown in Figure 3.10 (b)). It is evident that the responsivity decreases with increase in power density. This might be due to trap states present in the sample which causes the recombination and suppression of photogenerated carriers.
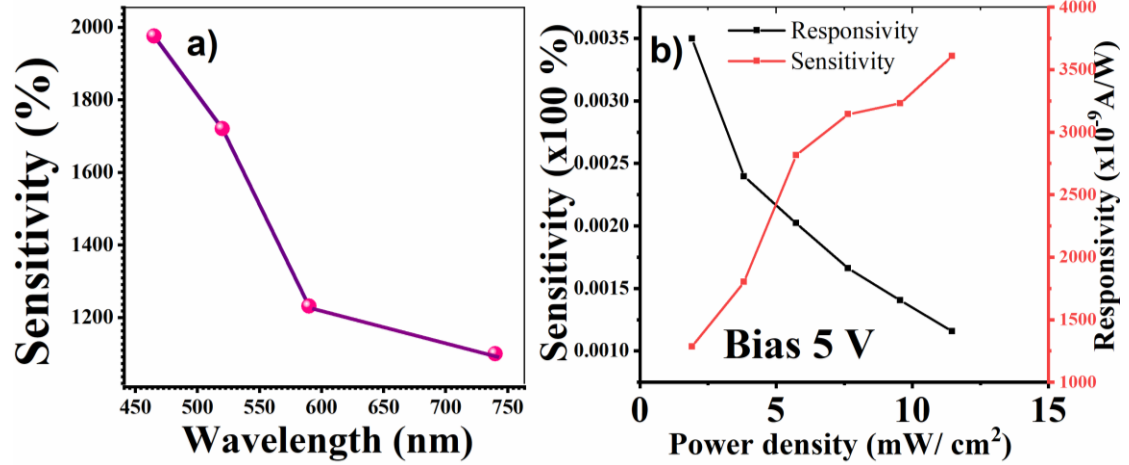
Figure 3.10. a) Sensitivity versus wavelength of incident radiation and b) sensitivity and responsivity versus power density graph.

3.3. AgI powder and thin films: Synthesis and characterization

3.3.1. Results and discussion

3.3.1.1. Structure

XRD pattern of AgI powder is included in Figure 3.11. Moreover, a comparison has done between the data with the standard database to confirm the crystalline phase. Yellow-colored AgI powder showed reflections from (100), (002), (101), (102), (110), (103), (112), (202), (203), (210), (300) and (302) planes and are matching well with the hexagonal phase for β-AgI (JCPDS # 09-0374).
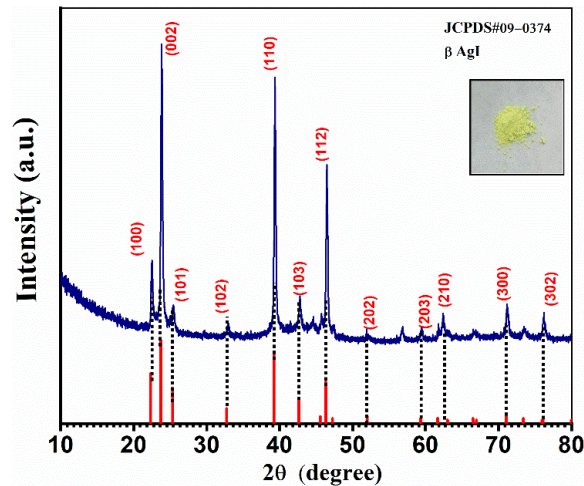
Figure 3.11. PXRD patterns of AgI powder.

Iodization for metallic Ag films of different thicknesses are done as we did for antimony sulfide (see section 3.5).
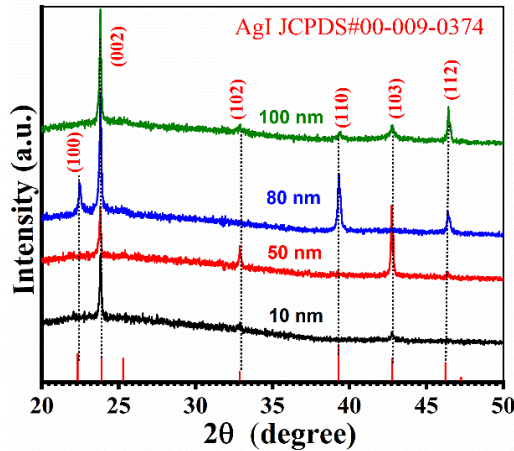
Figure 3.12. XRD patterns of AgI thin films formed at different Ag thicknesses (10, 50, 80, and 100 nm).

Diffraction patterns of AgI thin films are given in Figure 3.12. Peaks are compared and matched well with the standard JCPDS (file number 00-009-0374) of hexagonal AgI. The diffraction peaks located at 2θ = 22.31°, 23.7°, 32.7°, 39.2°, 42.6°, 46.3° are corresponding to (100), (002), (102), (110), (103), and (112) reflections of AgI. It is observed that appearing and vanishing of certain planes occur as Ag thickness varies. Compared to Ag-10 nm case, Ag-50 nm case has additional diffraction peaks due to (102) and (103) planes and they vanished in Ag-80 nm case. Also, a new pair of planes, (100) and (110) are identified for Ag-80 nm iodized film and they are absent in Ag-50 nm case. In addition, plane (100) is not observed in Ag-100 nm film in comparison with Ag-80 nm case. In all the cases a major diffraction peak at 23.7° is observed. Because of the increase in crystallinity of samples this peak intensity gets stronger with Ag thickness. The crystallite sizes of AgI films are calculated using equation ((8), see section 2.5.1) and the obtained values are 26.5, 48.8, 54.4, and 59.9 nm for 10, 50, 80, and 100 nm cases respectively. The crystallinity of AgI thin films vary with Ag film thicknesses, and this result matches well with the earlier studies[193–195].

48

3.3.1.2.*Structure and phase*
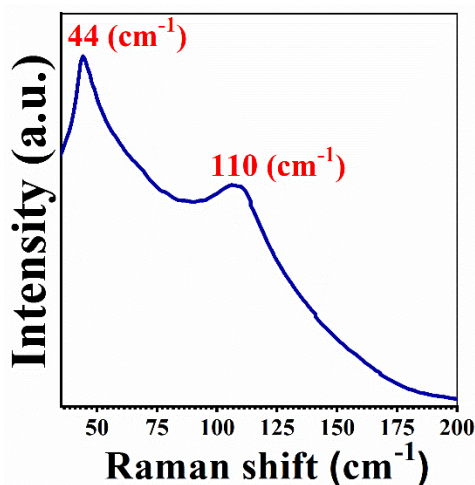
Figure 3.13. Raman spectrum of AgI powder at room temperature.

The molecular structure of precursor powder is elucidated using their respective Raman spectral analysis. Figure 3.13 shows the Raman spectrum obtained for AgI powder. We observed two Raman active modes for AgI powder as depicted in Figure 3.13, one at 44 cm^{-1} which is identified as 'boson mode' and other at 110 cm^{-1} which is due to Ag-I stretching[196–199].
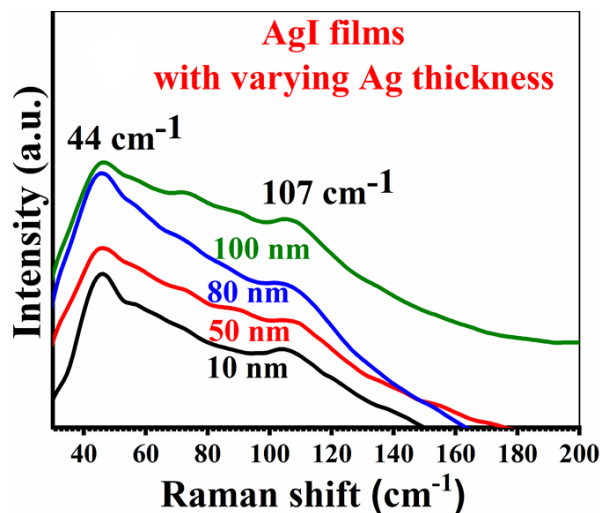
Figure 3.14. Raman spectra of AgI films with various Ag thicknesses.

Figure 3.14 illustrates the Raman spectra of AgI thin films. A major peak at 44 cm^{-1} as well as a low intensity peak at 107 cm^{-1} are noticed. The 107 cm^{-1} peak is due to Ag-I

stretching. Both Raman active modes positioned at these values are in well terms with the earlier reports[196,200].

3.3.1.3. *Morphology*

FESEM images correspond to both Ag and AgI thin films are captured in the secondary electron mode (SE) with an applied acceleration voltage of 2 kV. The magnified images are given in inset of each micrograph. Surface morphologies of Ag and AgI thin films are compared. FESEM images of Ag thin films are illustrated in Figure 3.15 (a, c, e, and g). The surface morphologies of metallic films consisted of compactly arranged particles. In comparison with metallic films, each silver iodide film (given in Figure 3.15 (b, d, f, and h)) has distinct surface morphology. For 10 nm iodized film, it is composed of randomly distributed, irregularly shaped particles. In the case of 50 nm iodized film, the surface morphology has small spherical-shaped particles with some voids in between them. The 80, and 100 nm iodized films morphologies are similar. Compared to 50 nm iodized film, 100 nm film morphology is composed of bigger particles. Similar nature for surface morphologies was reported for electrochemically deposited AgI thin films by Zheng et al[201].
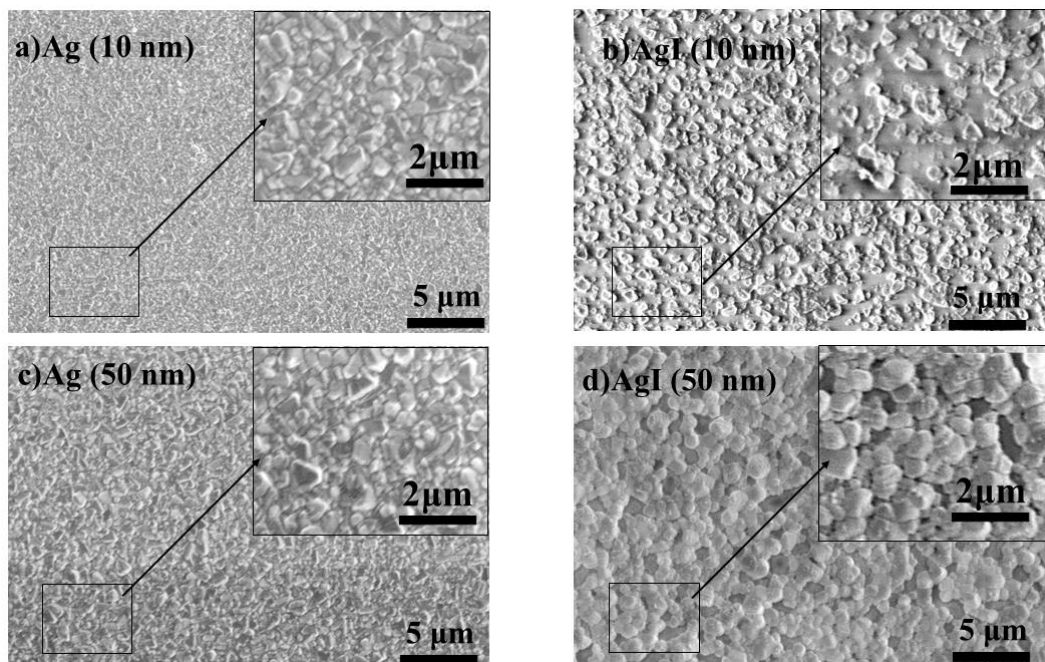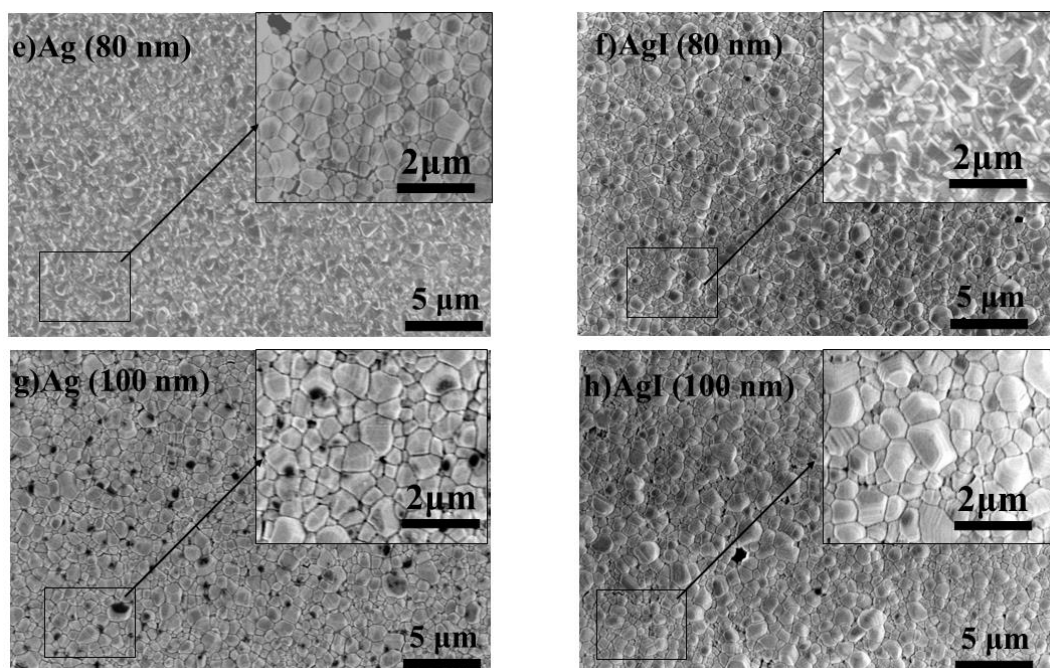
Figure 3.15. FESEM micrographs of Ag and AgI films formed with different Ag thickness, a) Ag(10 nm), b) AgI(10 nm), c) Ag(50 nm), d) AgI(50 nm), e) Ag(80 nm), f) AgI(80 nm), g) Ag(100 nm), and h) AgI(100 nm).

3.3.1.4.*Chemical state*

Figure 3.16 starts with the survey pattern and high-resolution spectra for AgI powder. Survey spectrum for AgI shows the presence of Ag and I. The Ag core level is splitting into two singlets (Ag $3d_{5/2}$ located at 368.2 eV and Ag $3d_{3/2}$, located at 374.2 eV). These binding energy values are corresponding to the Ag^+ state in AgI [176,202]. The two peaks of I $3d_{5/2}$ and I $3d_{3/2}$ (at 619.51 and 631.01 eV) are belonging to I^- state in AgI with a binding energy difference of 11.5 eV[176,203].
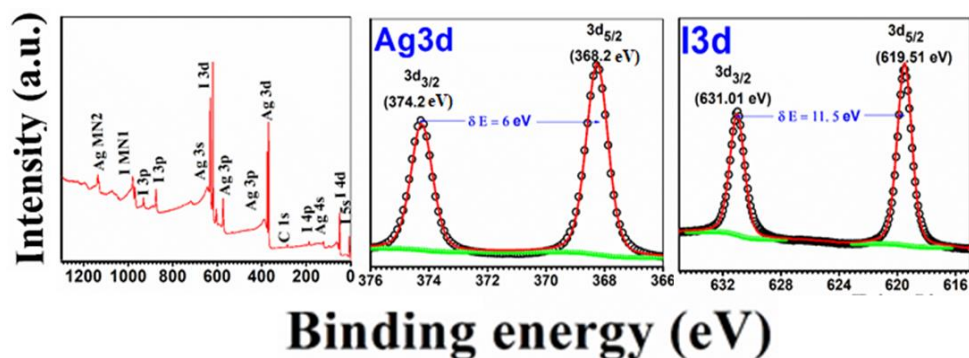
Figure 3.16. XPS analysis of AgI powder.

XPS analysis of AgI thin film is given in Figure 3.17. The survey pattern of AgI thin film reveals Ag, I, and C elements on the sample surface. Binding energies values of Ag 3d at 368.24 and 374.24 eV are corresponding to Ag^+ state in AgI with 6 eV of energy difference[202]. The binding energies of I 3d peaks at 619.45 eV and 630.95 eV are due to I^- state in AgI with an energy separation of 11.5 eV[203].
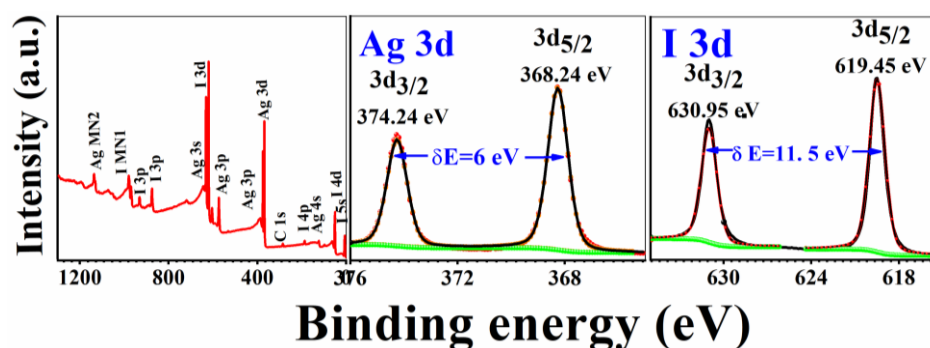
Figure 3.17. XPS analysis of AgI film (silver thickness of 100 nm).

A comparative study of high-resolution spectra of the silver iodide thin films of various silver thicknesses are carried out and are shown in Figure 3.18. As silver thickness increases, the peak intensity corresponds to the constituent elements also increases, this result correlates with the XRD results. A small shift in the peak position is observed for all the cases.
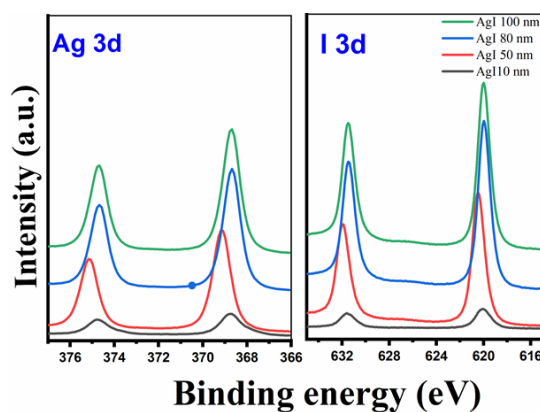
Figure 3.18. Comparison between the XPS high-resolution spectra of AgI thin films of various silver thickness.
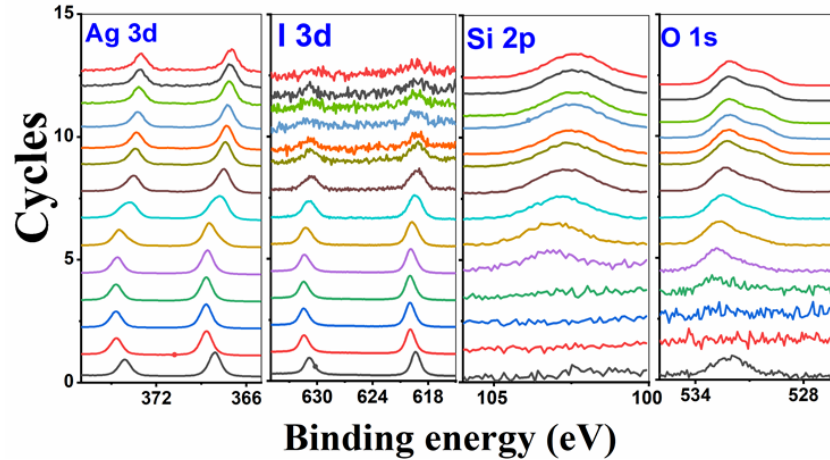
Figure 3.19. Depth profile analysis of AgI thin film (Ag thickness: 100 nm).

As mentioned earlier, XPS surface analysis can perform up to the depth of 10 nm. A detailed study was conducted to see how the elements are distributed through the film's depth (100 nm film of AgI) (shown in Figure 3.19) through depth profile analysis. It was done by etching out AgI from the sample surface using Ar+ ion after each cycle of analysis. Elements: Ag and I are uniformly distributed till 11th level of the film, while Ag is identified till the depth due to difference in etching rate. The signals from the glass substrate (Si and O) identified from the 12th level.

3.3.1.5. *Optical properties*

Optical properties of the films are studied from their respective absorbance, transmittance, and reflectance spectra. Both measurements and calculations, have done as explained in section 2.5.5. Figure 3.20 (a) illustrates the optical absorption spectra for AgI thin films in the wavelength range 300-1500 nm. After the iodization, the films of silver turned into light yellowish AgI films. From its zoomed version in the range 300-500 nm (shown in inset), it has a fundamental absorption edge around 400-450 nm. From the Tauc plots (Figure 3.20 (b)), optical bandgap (E_g) of AgI films was estimated. Direct bandgap values are in the range 2.74-2.65 eV (Figure 3.20 (c)) for 10, 50, 80, and 100 nm silver thickness respectively and the values agree with the earlier reports[158,204].
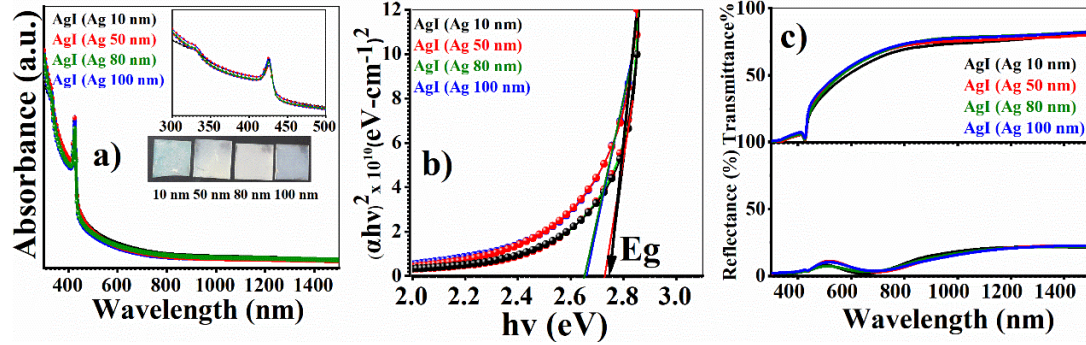
Figure 3.20. Optical absorbance spectra and direct Tauc plots of AgI thin films synthesized at different silver thickness.

3.4. Rapid iodization process for the fabrication of CuI films

3.4.1. Results and discussions

3.4.1.1. Structure

Diffraction profile of CuI films (with different copper thicknesses) are given in Figure 3.21Figure 3.21. The diffraction peaks are compared with standard JCPDS file (PDF#00-006-0246) and they match well with the standard zinc blend CuI. Three diffraction peaks are observed at $2\theta = 25.47°$, $29.5°$, and $42.19°$ and they correspond to (111), (200) and (220) reflections. In the XRD patterns of all films, peak at $25.47°$ is the major diffraction peak.
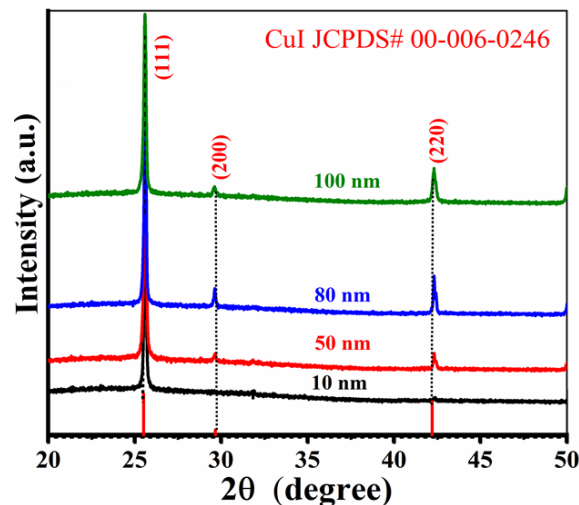
Figure 3.21. X-Ray diffraction patterns of CuI thin films formed at various copper thicknesses (10, 50, 80, and 100 nm).

With an increase in copper thickness the improvement in the crystallinity of samples is observed. Diffraction peaks of metallic copper or oxides of copper were not observed in any of the patterns. It implies that a complete transformation of metallic Cu to zinc blend CuI. We observed that with an increase in copper thickness, the diffraction peak intensities also shown an increment[205–207]. The crystallite size was estimated using Debye-Scherrer equation (8) (see section 2.5.1). For the calculation, the peak corresponding to (111) plane was considered and crystallite sizes calculated are 47, 51.4, 58.4, and 58.7 nm for 10, 50, 80, and 100 nm copper thickness, respectively. The crystallite size of samples increases with copper thickness and obtained values agree with the previous report by Dintle et *al*[208].

3.4.1.2. *Structure and phase*

Figure 3.22 displays the Raman spectra of CuI films. It is observed that there is a single-prominent peak for all films. This major peak positioned at 122 cm^{-1} is assigned as CuI transverse optical (TO) mode[209]. The intensity of this peak increases with an increase in copper thickness and this result correlates with the XRD results.
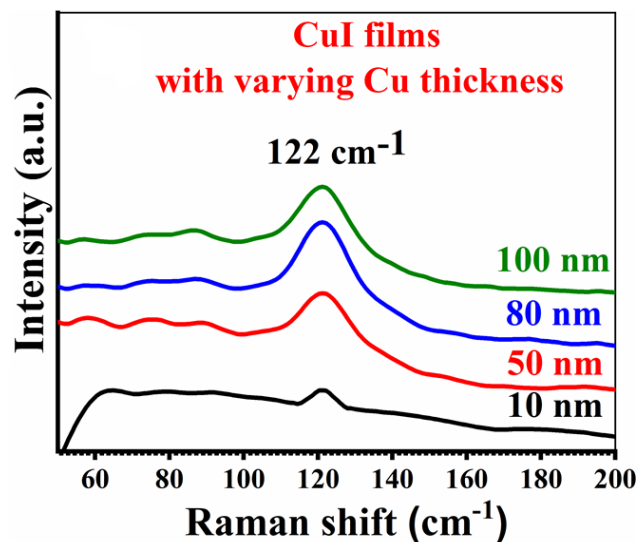
Figure 3.22. Raman spectra of CuI films with various copper thickness.

3.4.1.3. *Morphology*

FESEM images are captured in the secondary electron mode (SE) (an acceleration voltage of 2 kV). The magnified images (with magnifications 10 k and 25 k) are shown each micrograph's inset. FESEM images correspond to films of metallic copper (Cu) thin films as well as copper iodide (CuI) prepared at various copper thicknesses (10, 50, 80, and 100 nm) are given in Figure 3.23.
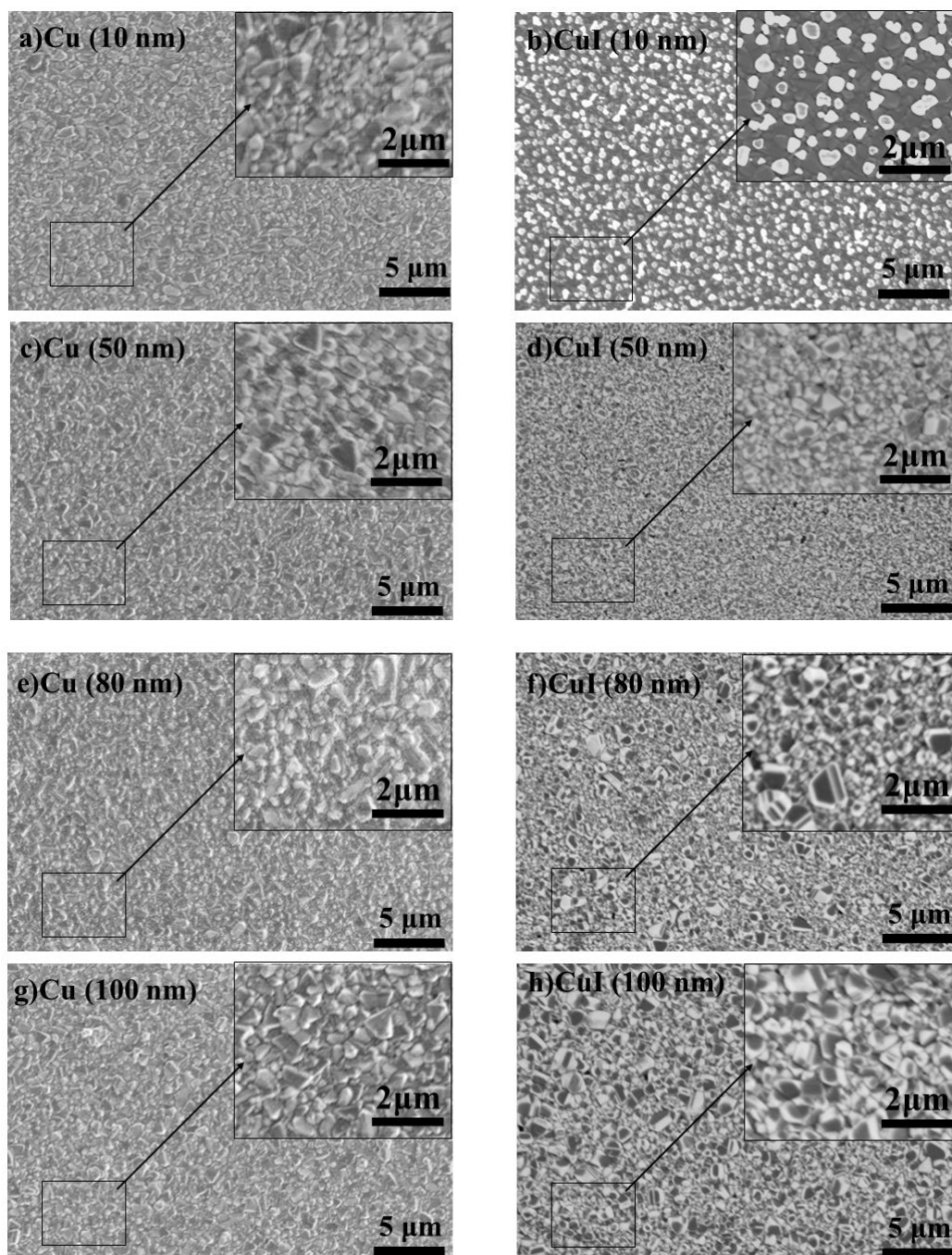
Figure 3.23. SEM micrographs of Cu and CuI films formed with different Cu thickness, a) Cu(10 nm), b) CuI(10 nm), c) Cu(50 nm), d) CuI(50 nm), e) Cu(80 nm), f) CuI(80 nm), g) Cu(100 nm), and h) CuI(100 nm).

We observed that the morphologies of the precursor films are similar (Figure 3.23 (a-g)) and composed of compactly arranged particles. Surface morphological images of copper iodide films are shown in Figure 3.23 (b, d, f, and h). For 10 nm case, the surface morphology contains rectangular like particles over which small shapeless particles are dispersed. With an increase in Cu thickness, their morphologies looked entirely different from that of Cu films and composed of densely arranged, bigger sized particles. Kaushik and his coworkers reported the same nature for surface morphologies of CuI films[205].

3.4.1.4. *Surface analysis*

The survey pattern and high-resolution spectra of individual constituent species present in the sample is shown in Figure 3.24.
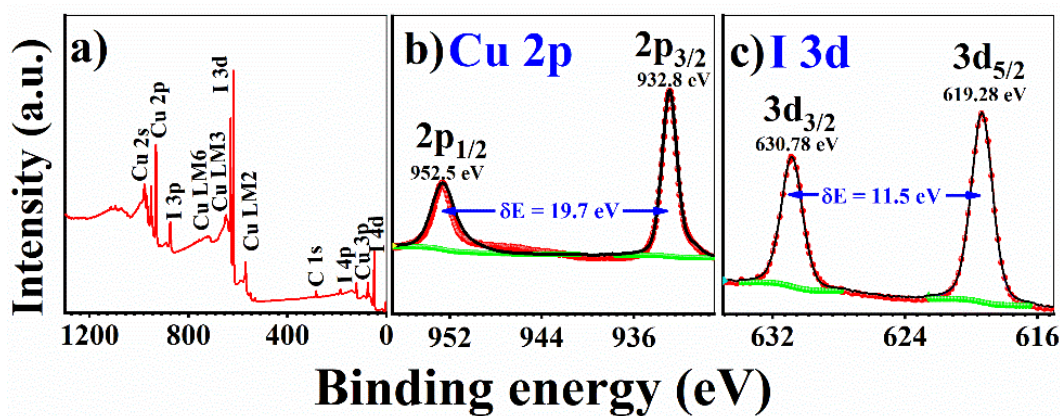
Figure 3.24. XPS high-resolution spectra of CuI film (copper thickness: 100 nm).

The survey pattern revealed that Cu, I, and C are present on the sample surface. The peaks positioned at binding energy values, 932.8 and 952.5 eV, represent the +1 state in CuI. Similarly, iodine high-resolution spectrum is composed of a 3d doublet (I $3d_{5/2}$ and I $3d_{3/2}$) with peak B.E.s at 619.28 and 630.78 eV (with an energy separation of 11.5 eV) and that corresponds to the I⁻ states in CuI [210–214].
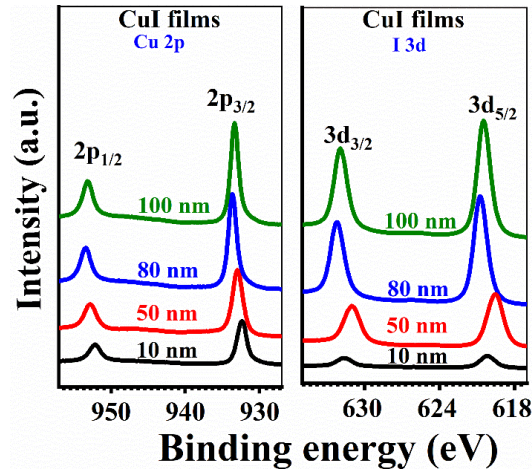
Figure 3.25. Comparison between the XPS high-resolution spectra of CuI thin films of different copper thicknesses.

Comparison between the high-resolution spectra for CuI thin films of various Cu thicknesses are shown in Figure 3.25. With an increment in Cu thickness, the constituent elements peak intensity also increases and is correlating with our XRD results.
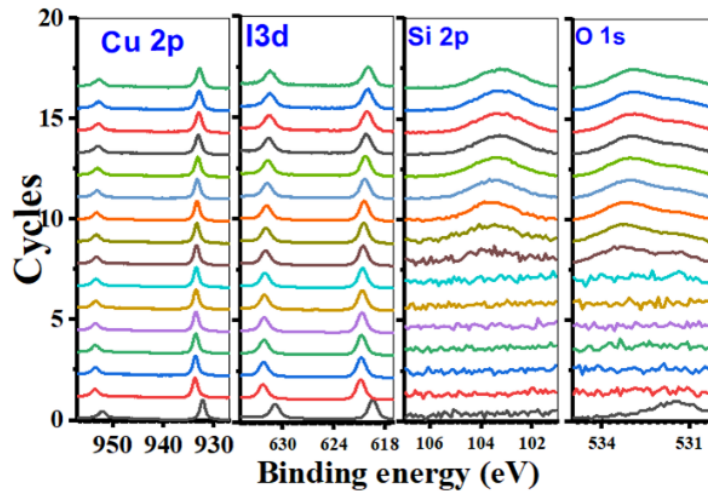
Figure 3.26. Depth profile analysis of CuI thin film with Cu thickness 100 nm.

We conducted a depth profile analysis for our CuI film of 100 nm-Cu thickness to study how the elements are distributed till the film depth (shown in Figure 3.26). CuI film was etched out by Argon ions in each cycle of analysis and a uniform distribution of the elements Cu and I are observed. Since the film was deposited on the glass substrate, Si

and O elements profile is also included. The depth profile analysis confirms the homogeneity and uniformity of the film.

3.4.1.5. *Optical properties*

All the measurements and calculations are done, as explained in section 2.5.5 for the optical property studies. The absorbance spectra of the CuI films are shown in Figure 3.27(a) and photo of the films are given in inset. The zoomed version of optical absorption spectra in the 300-500 nm wavelength range are given in inset. Each film has a fundamental absorption edge in the wavelength range: 400-450 nm. A hump is appeared for all the films at 410 nm wavelength, and it might be because of the electron excitation between the sub-bands of the valence band and conduction band[215,216]. The transmittance and reflectance spectra for each case are shown in Figure 3.27 (c). The direct optical bandgap values are obtained in the range 3.03-3.00 eV (Figure 3.27 (b)) for 10, 50, 80, and 100 nm Cu thicknesses. These bandgap values are matching with the earlier reports[208,217].
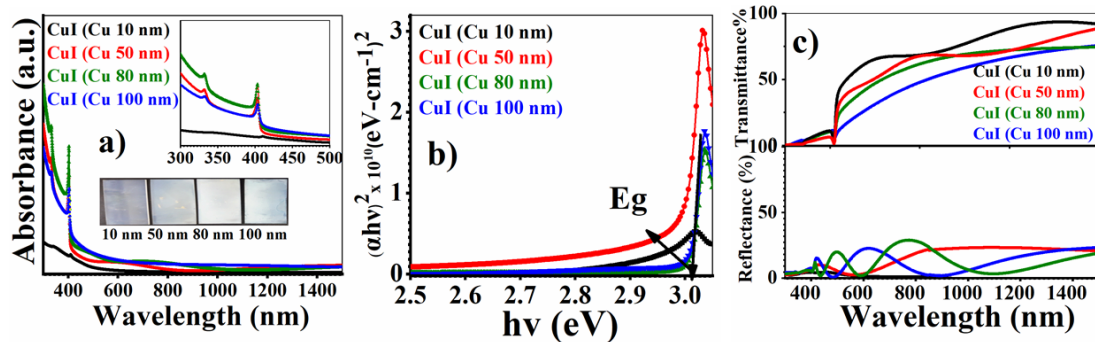
Figure 3.27. UV-Vis-NIR absorption spectra and Tauc plots of CuI thin films synthesized at different copper thickness.

3.5. Rapid iodization for the fabrication of SbI₃ thin films

3.5.1. *Results and discussion*

3.5.1.1. *Structure*

Sb_2S_3 thin films deposited at different deposition times (30 min ≈ 185 nm, 1 h ≈ 250 nm and 2 h ≈ 480 nm) were iodized for different durations (30 s to 5 min). We observed a color change after iodization where all the dark yellow Sb_2S_3 films turned into light orange color as shown in Figure 3.28.
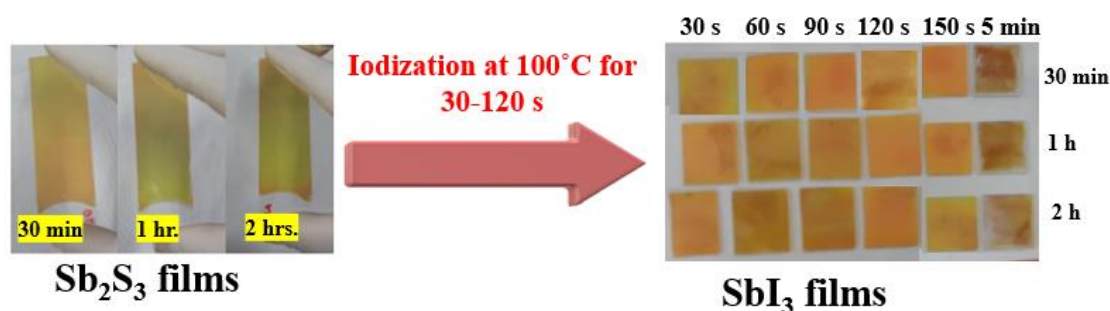
Figure 3.28. Photos of SbI₃ thin films synthesized via iodization of Sb_2S_3 films with different deposition times a) 30 min, b) 1 hour and c) 2 hours.

XRD patterns of the SbI₃ thin films are given in Figure 3.29 (a, b and c). XRD patterns of amorphous Sb_2S_3 thin films are also included in the figure and compared with the SbI₃. It is evident from the diffraction patterns that the iodization process has brought evolutions to the amorphous Sb_2S_3 films because of the appearance of new diffraction peaks. By comparing the diffraction patterns with the standard database (JCPDS#98-000-9298), we found that all the diffraction peaks are matching well with the hexagonal SbI₃. We did not observe any peaks related to sulfides, oxides or oxi-iodides in the XRD patterns. Diffraction peaks identified at 2θ values: 14.75°, 18.7°, 29.76°, 31.5°, 41.08°, and 45.31° are corresponding to (003), (012), (006), (113), (2-16), and (009) planes respectively. An earlier work done by Mohan and coworkers revealed that the iodization durations have a pronounce effect on the crystallinity of SbI₃ and iodization times ranging from 5 min-9 h was utilized for iodizing thermally-evaporated Sb films[183]. Our fast iodization process of

60

chemical bath deposited Sb_2S_3 thin films resulted in highly crystalline, phase pure SbI_3 films within the first 30 s of iodization.

In the case of 30 min deposited films, no high intensity (strong) diffraction peaks are observed for the smallest iodization time (30 s) compared to higher iodization times. Three diffraction peaks are found at 2θ values: $14.75°$, $29.76°$, and $45.31°$. For 1 and 2 h deposited Sb_2S_3 thin films iodization ended up in the formation of SbI_3 binary with additional diffraction peaks compared to 30 min deposited films. Here new diffraction peaks are observed at $18.7°$, $31.5°$ and $41.08°$. For all the three cases of chemical bath deposition time of Sb_2S_3 (30 min, 1 h and 2 h), (006) peak appeared as the principal peak of reflection for SbI_3. This major diffraction peak intensity was found to increase with the increase in iodization time.

The methodology for preparation of SbI_3 film in the present work is inspired by the work done by Tiwari et *al* for the synthesis of BiI_3 from Bi_2S_3. According to their work, iodization (at 200 °C) of Bi_2S_3 film resulted in forming phase pure BiI_3[184]. The mechanism for this conversion of Bi_2S_3 to BiI_3 was explained using the principle: 'Pearson's hard soft acid base' wherein Bi^{3+} (soft-acid) readily associates with a I^- (which is a polarizable soft-base) resulted in the formation of BiI_3. The same principle is applied here for explaining the formation mechanism of SbI_3, wherein a polarizable soft acid Sb^{3+} simultaneously replaces S^{2-} (a hard-base) with I^- (a polarizable soft-base). This resulted in the formation of SbI_3 [185].

From the XRD data, the average crystallite size (D) was calculated by using the Debye-Scherrer formula,

$$D = \frac{k\lambda}{\beta Cos\theta} \qquad (14)$$

where λ (1.54056 Å) is the X-ray wavelength, k is a constant of value 0.9, and β is the full width half maximum (FWHM) located at the respective 2θ value. The average crystallite size values obtained are listed in Table 3.1.
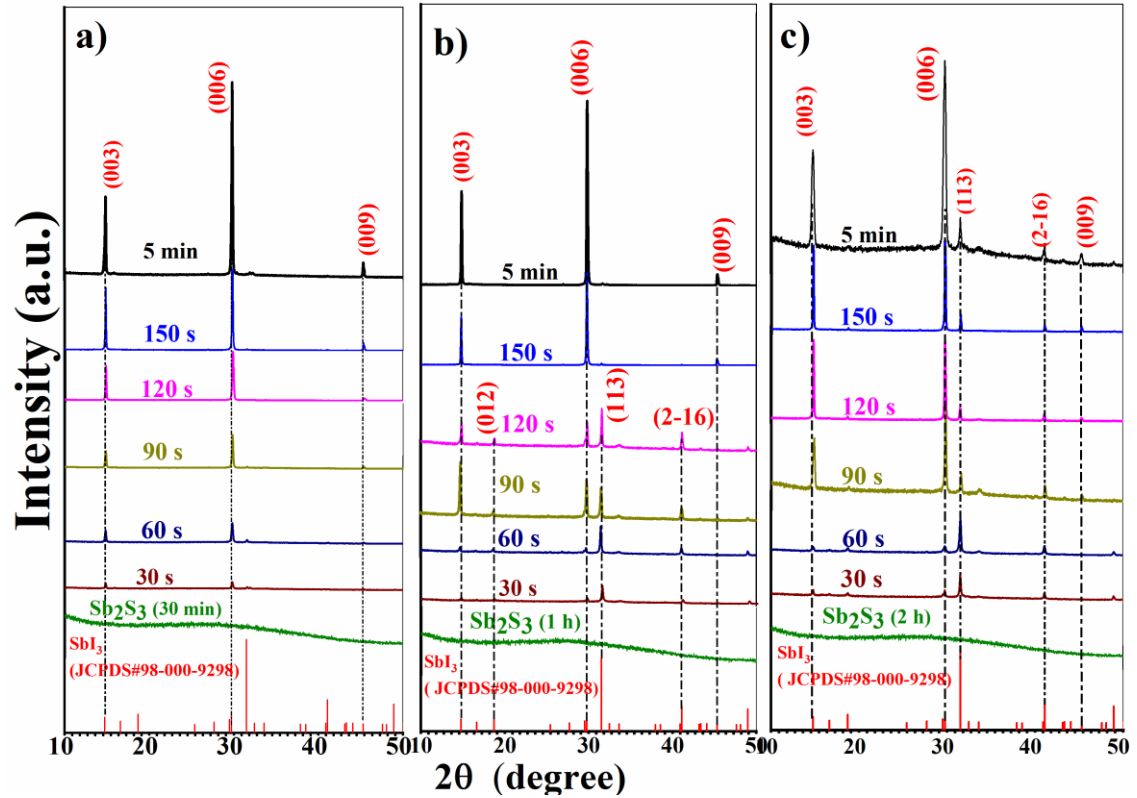
Figure 3.29. Diffraction patterns of SbI₃ thin films synthesized via iodization of Sb₂S₃ films with different deposition times a) 30 min, b) 1 hour and c) 2 hours.

Table 3.1. Average crystallite size values obtained for SbI₃ thin films.

Deposition time of Sb₂S₃ films	Iodization time taken for SbI₃ film's fabrication (s)	Average crystallite size (nm)
30 min	30	28
	60	37
	90	39
	120	41
	150	43
	5 min	44
1 h	30	32

	60	42
	90	43
	120	43
	150	49
	5 min	50
2 h	30	34
	60	42
	90	45
	120	51
	150	53
	5 min	45

3.5.1.2. *Structure and phase*

The rhombohedral SbI_3 belongs to R-3 space group. If the symmetry is known and the number of atoms in a unit cell is given, then it is possible to make the irreducible representation of a unit cell based on factor group analysis[186]. From the literature it is well known that the irreducible representation of SbI_3 unit cell has $4A_g$, $4E_g$, $4A_u$, and $4E_u$ modes. Interestingly, among these modes, Raman active are A_g and E_g modes whereas A_u and E_u modes are infrared active[187].

Raman spectra of SbI_3 films are given in Figure 3.30. Figure 3.30 (a) shows the 30 min deposited Sb_2S_3 and corresponding SbI_3 films. It is evident from their spectra that the 30 s iodized film does not show any major peak, and this result is correlating well with the XRD result of our 30 s iodized film (shown in Figure 3.29). When the iodization times were increased, we observed four major lines at 44, 65, 137, and 159 cm^{-1}. For 60 s iodized film, we observed two peaks at 137 and 159 cm^{-1} and for 90 s and 120 s iodized films, a new peak at 65 cm^{-1} appears along with those two peaks. The phonon modes at 44 cm^{-1}, 65 cm^{-1} and 137 cm^{-1} are assigned as v_1 (A_g), v_3 (A_g) and v_4 (A_g) modes respectively, and Raman active mode located at 159 cm^{-1} is assigned to v_4 (E_g) mode[187,188].
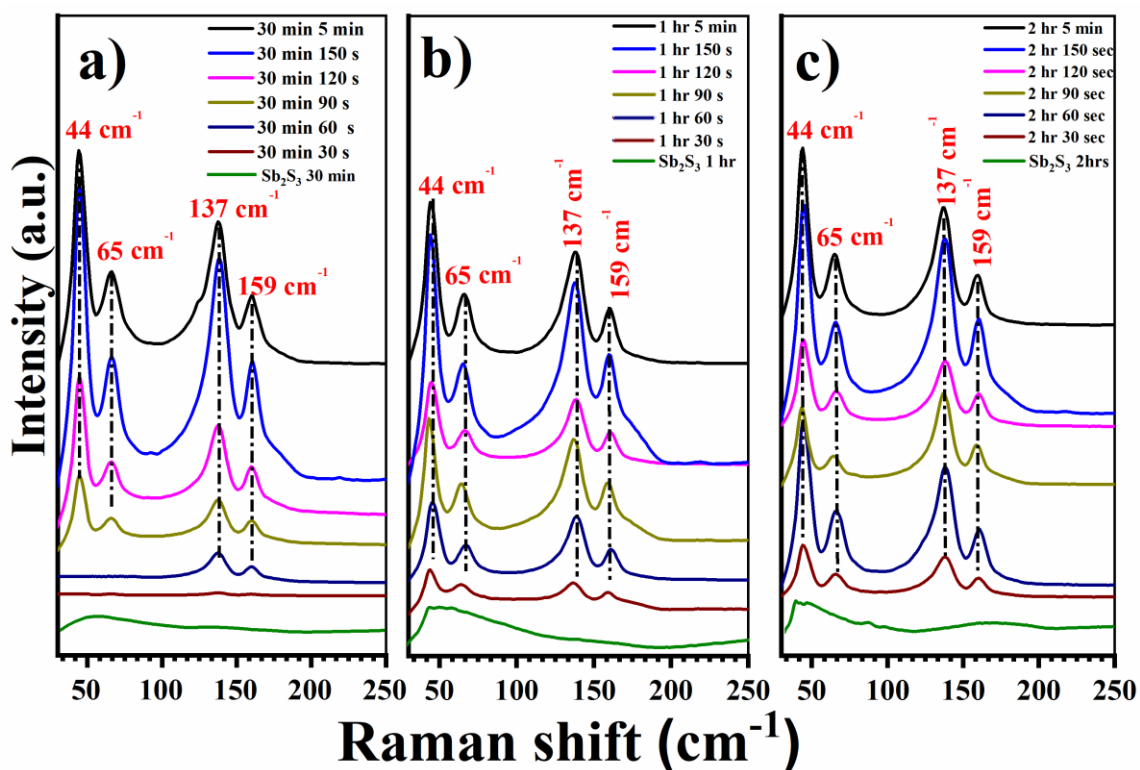
Figure 3.30. Comparison between the Raman spectra of Sb_2S_3 and SbI_3 films formed at different deposition durations and iodization times.

Whereas 1 h and 2 h deposited Sb_2S_3 and their corresponding SbI_3 films (Figure 3.30 (b and c)) showed four distinct bands of A_g and E_g modes and these modes appeared even for the lowest iodization time unlike 30 min deposited Sb_2S_3 iodized films. This result is supported by our XRD results since the films became crystalline after the first 30 s of iodization. A remarkable similarity for all the spectra of different experimental conditions was observed in the range 30 to 250 cm^{-1}.

3.5.1.3. *Morphology*

Surface morphology studies of SbI_3 thin films were done using FESEM. For that, an acceleration voltage of 2 kV was used. Images were captured in the secondary electron (SE) mode at magnifications of 10 and 25 k. Magnified images are given in the inset of micrographs of each case. A comparison between the surface morphologies of Sb_2S_3 films deposited at various deposition times (30 min, 1 h and 2 h) are done and represented in

Figure 3.31. In the figure, 30 min deposited Sb_2S_3 and their respective SbI_3 films are shown at the top, 1 h deposited Sb_2S_3 and their respective SbI_3 films are given at the center) and the bottom part represent 2 h deposited Sb_2S_3 and their respective SbI_3 films.

SEM image of pristine Sb_2S_3 is shown in (a) part of Figure 3.31 and the morphology revealed that the surface is composed of compactly arranged spherical particles. When compared to the SEM images of Sb_2S_3 films, it is found that SbI_3 films possess distinct surface morphologies. For 30 min deposited Sb_2S_3 and their respective SbI_3 films, 30 s iodized film (shown at top of Figure 3.31 (b)) surface is composed of a compact morphology, with randomly arranged irregularly shaped particles. In the case of 60 s of iodized film, the surface morphology has a net like structure with shapeless particles are attached to rod-shaped particles as given in the top of Figure 3.31 (c). For higher iodization time, that is 90 s as shown at top of Figure 3.31 (d)) the film surface is composed of thicker rod-shaped particles with many smaller shapeless particles are attached. In the case of 120 s of iodization, the film showed a morphology where interconnected rod-like particles with tiny droplets like-shaped particles are adhered (shown at top of Figure 3.31 (e)). For higher iodization times such as 150 s and 5 min films attained fewer pinholes with uniform surface coverage as shown at the top of Figure 3.31 (f and g).
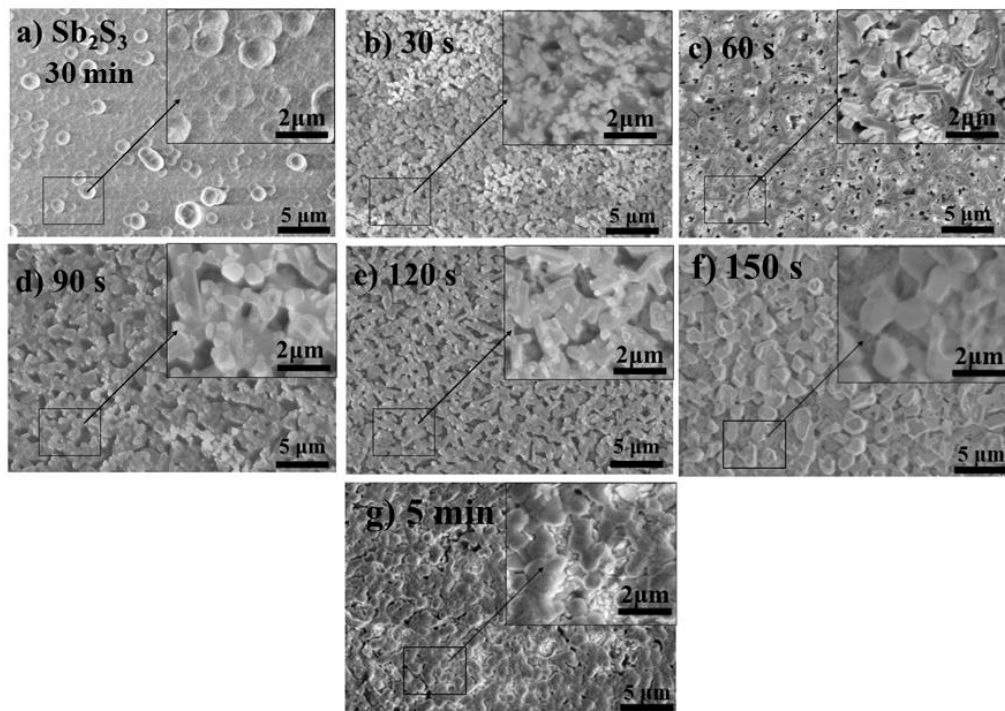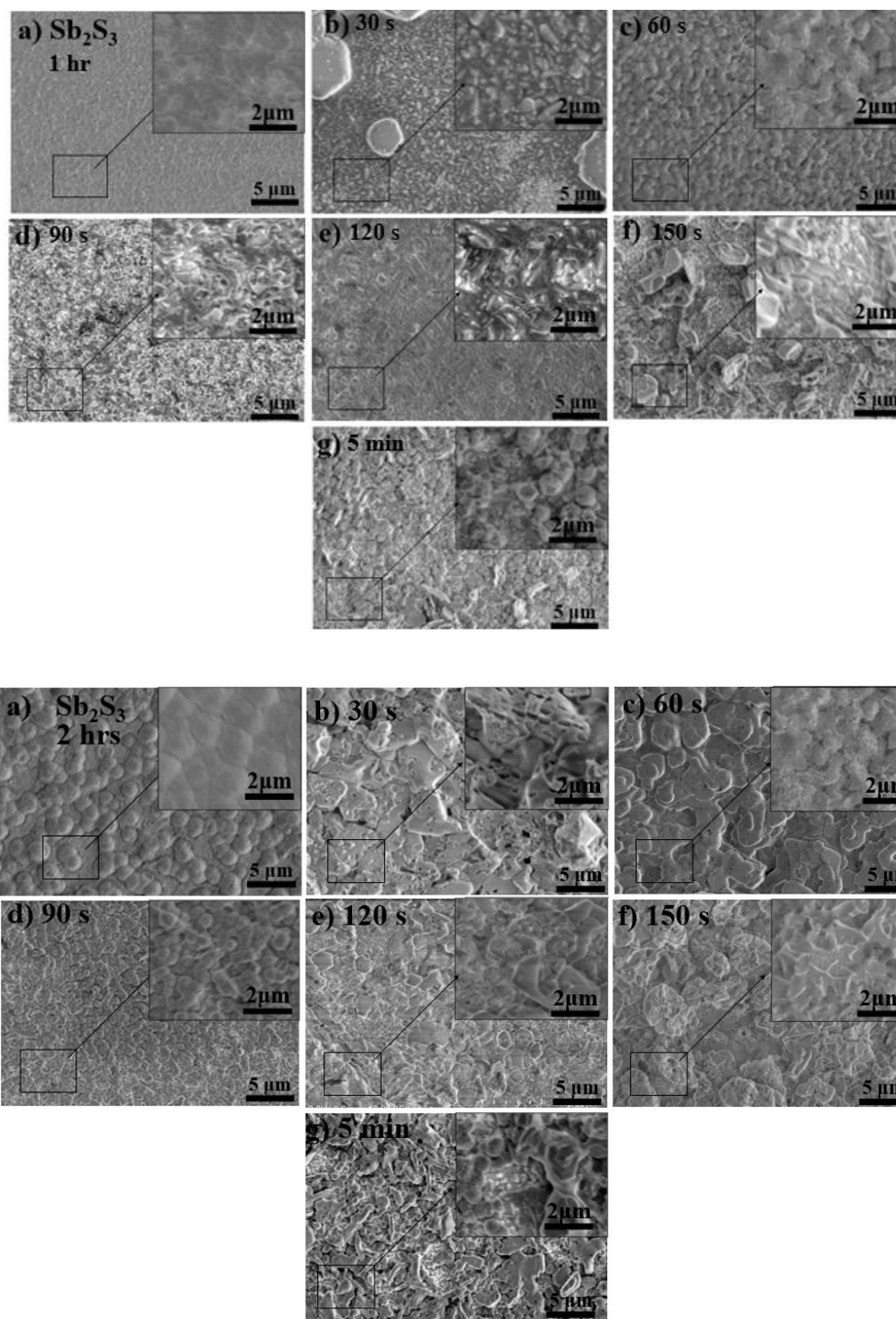
Figure 3.31. SEM micrographs of Sb_2S_3 with various thicknesses and their respective SbI_3 films formed at different iodization times, a) Sb_2S_3 as deposited film, and b), c), d), e), f), and g) SbI_3 films of different iodization times 30s, 60s, 90 s, 120 s, 150 s, and 5 min respectively. ((Top) 30 min deposited Sb_2S_3 and their respective SbI_3 films, (center) 1 h

deposited Sb_2S_3 and their respective SbI_3 films, (bottom) 2 h deposited Sb_2S_3 and their respective SbI_3 films).

As the deposition duration time of Sb_2S_3 was increased more uniformity and surface coverage is observed as shown at the center and bottom portions of Figure 3.31. All the iodide films born from higher thickened Sb_2S_3 show a compact morphology and in each case, the grain boundaries became more visible implying the improvement in surface morphologies of iodide films. SEM-EDS mapping of 2 h deposited Sb_2S_3 their respective SbI_3 films formed at iodization times of 30 s, 120 s, and 5 min was carried out for the estimation of elemental composition (shown in Figure 3.32). EDS mapping of Sb_2S_3 thin film revealed that Sb and S are uniformly distributed over the film. Whereas SbI_3 films mapping area confirms the conversion of antimony sulfide into antimony iodide with a homogeneous distribution of constituent elements: Sb, and I, over the sample surface. Compositional analysis of antimony iodide thin films is listed in Table 3.2.

Table 3.2. Composition analysis of Sb_2S_3 and SbI_3 thin films using EDS mapping.

Material	Atomic percentage			S/Sb ratio	I/Sb ratio
	Sb	I	S		
2 h deposited Sb_2S_3	3.77	-------	5.05	1.3	-------
30 s iodized SbI_3	6.71	25.83	3.93	0.58	3.84
120 s iodized SbI_3	4.58	21.02	1.23	0.26	4.58
5 min iodized SbI_3	3.07	23.77	0.52	0.16	7.74
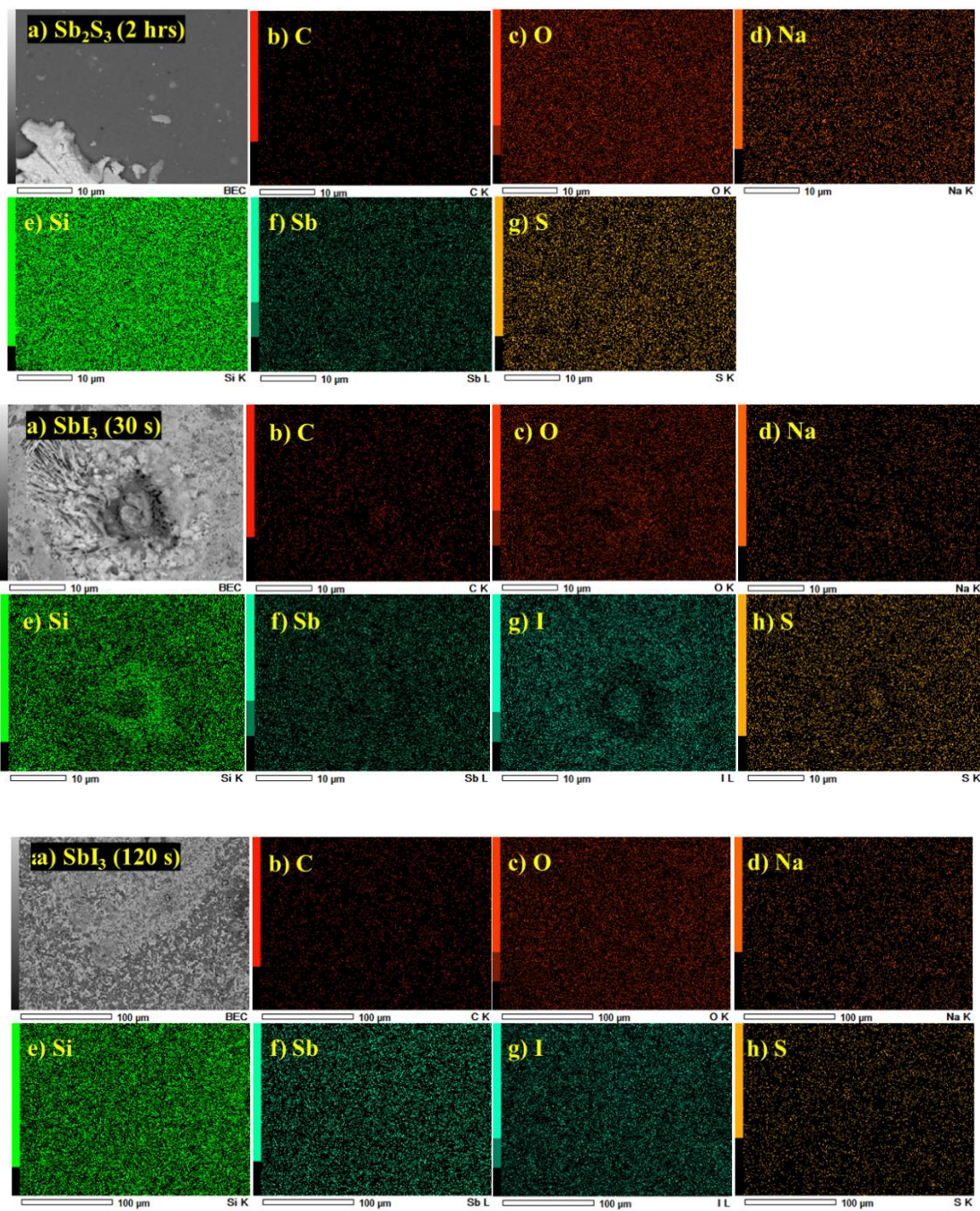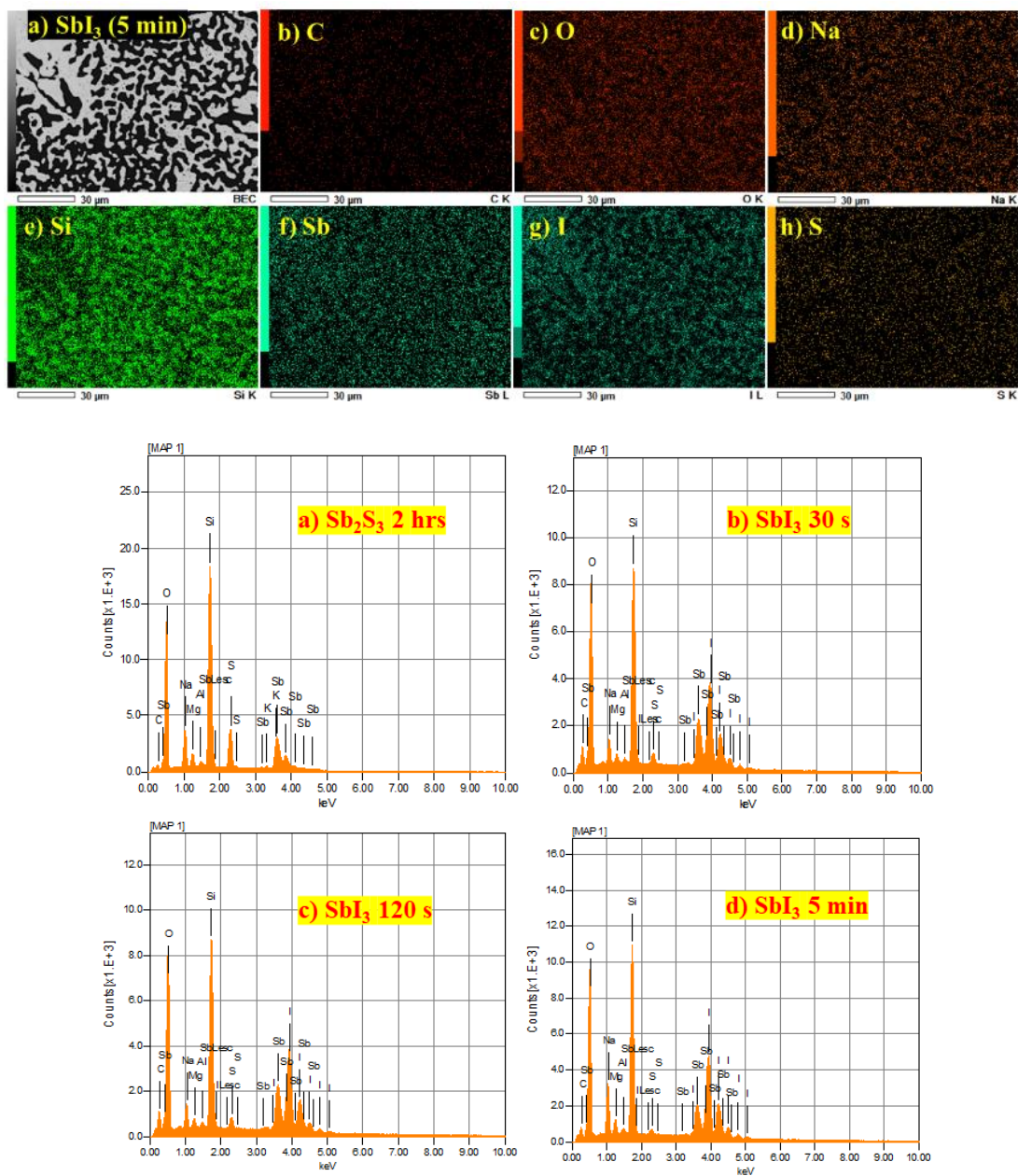
Figure 3.32. EDX mapping for a) 2 h deposited Sb_2S_3 and its SbI_3 films formed at b) 30 s, c) 120 s, and d) 5 min of iodization times.

3.5.1.4. *Surface analysis*

Surface analysis of SbI_3 film iodized for 120 s was done using XPS. In the survey analysis (shown in Figure 3.33(a)) elements of Sb, I and C are detected and no peak of sulfur is observed. The high-resolution spectrum of Sb 3d has two singlets (given in Figure 3.33

(b)), namely Sb $3d_{3/2}$ and Sb $3d_{5/2}$ located at 530.3 eV and 539.64 eV respectively. The two singlets are arisen because of spin-orbit coupling phenomenon. These two peaks are separated by an energy difference (δ E) of 9.34 eV. Peak located at 530.3 eV corresponds to the Sb^{3+} state in SbI_3[189]. The high-resolution spectrum of I 3d is composed of a doublet due to spin-orbit coupling as illustrated in Figure 3.33 (c). B.E. values observed at 619.35 eV and 630.85 eV with an energy difference of 11.5 eV. Compared to the high-resolution spectrum of Sb_2S_3, where Sb $3d_{3/2}$ and Sb $3d_{5/2}$ are located at 529.38 eV and 538.64 eV[190], there is a shift in the B.E. values for Sb 3d peak in our SbI_3.
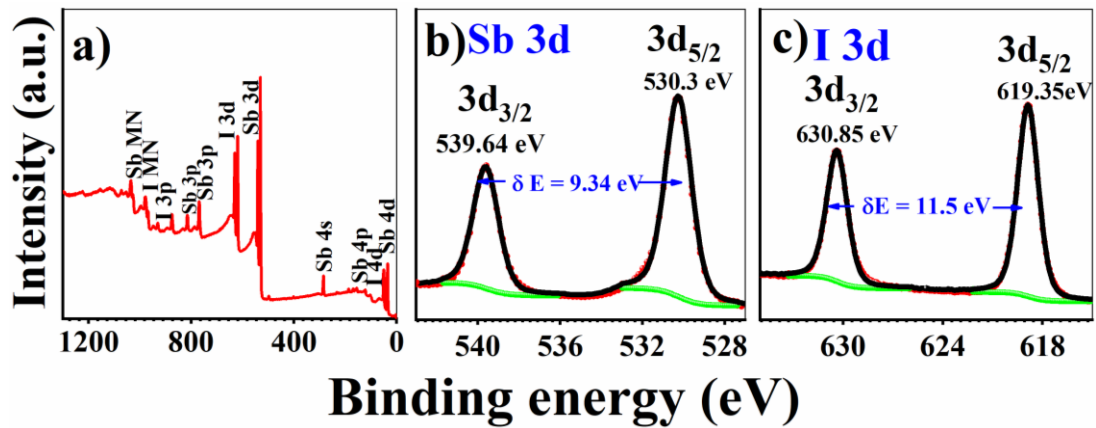
Figure 3.33. XPS high-resolution spectra of SbI_3 thin film (iodization time of 120 s) a) surface analysis, b) high-resolution spectra of Sb 3d and c) high-resolution spectra of I 3d.

3.5.1.5. *Optical properties*

The optical properties of the films were analyzed. Both the measurements and calculations were completed according to section 2.5.5. The optical absorption spectra of the Sb_2S_3 deposited at different deposition times and corresponding SbI_3 thin films are given in Figure 3.34 (a, b and c). The transmittance and reflectance plot are illustrated in Figure 3.34 (a1, b1 and c1). A color change was observed after iodization where the dark yellow Sb_2S_3 films turned into dark orange SbI_3. SbI_3 thin films displayed a systematic shift in the absorption spectrum from 551 nm to higher wavelengths with increase in the iodization time. Both direct (Figure 3.34 (e-j)) and indirect bandgap (Figure 3.34 (k-p)) values are estimated from the respective Tauc plots.
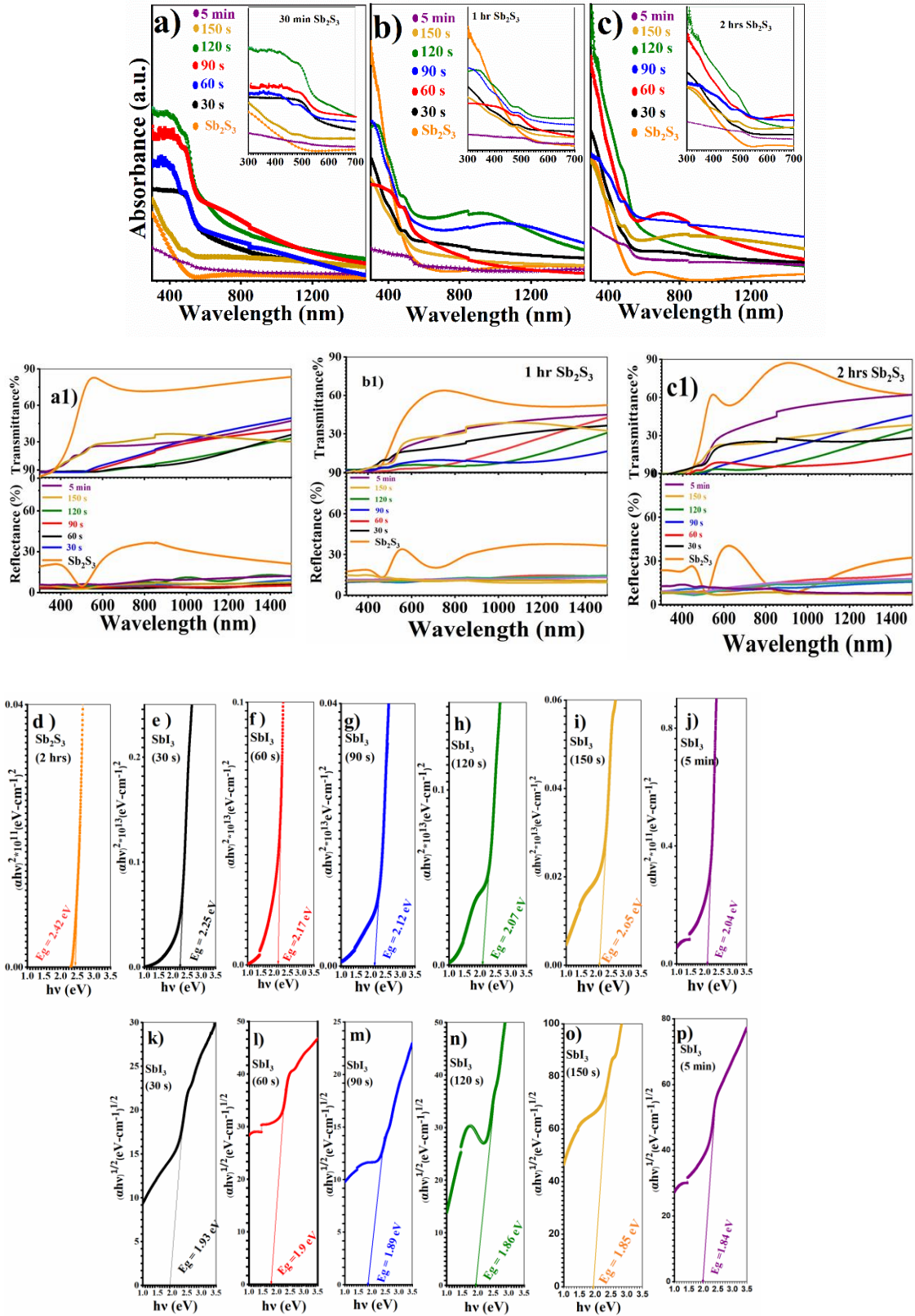
Figure 3.34. Optical absorption spectra of Sb_2S_3 and corresponding SbI_3 thin films synthesized at different iodization times (a-c), transmittance and reflectance plot (a1, b1, and c1) and Tauc plots of 2 h deposited Sb_2S_3 and corresponding SbI_3 thin films (direct (d-j) and indirect (k-p)).

From the Tauc plot, it is observed that the direct bandgap values are ranging from, 2.25-2.04 eV whereas indirect bandgap values are ranging from 1.93-1.84 eV for 30 s, 60 s, 90 s, 120 s, 150 s, and 5 min respectively. These optical bandgap values are compared with the previously reported values[149–151,191,192]. Both direct and indirect transitions are reported for SbI_3, thus for a better understanding relevant studies are necessary. Based on our optical properties study, the bandgap values vary with iodization time and it decreases for higher iodization time. Variations in optical bandgap values in our study are compared with the previously reported values and it might be because of the factors like the synthesis technique and morphological differences of films.

3.5.1.6. *Electrical properties*

Based on the above studies, we developed a photodetector device based on SbI_3. For this we painted silver electrodes with length and breadth 5 mm using flash dry silver paint. Schematic representation of SbI_3 photodetector is depicted in Figure 3.35.
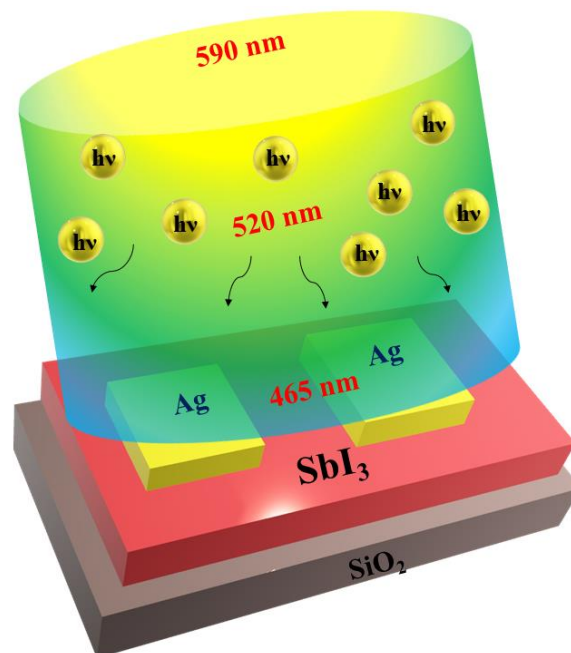
Figure 3.35. Schematic representation of SbI$_3$ photodetector.

White light and LEDs with different wavelengths (465, 520, and 590 nm) were used to irradiate the device. When the light was turned on, a high photocurrent is detected, and its photocurrent response versus time (in seconds) is measured for Sb$_2$S$_3$ and SbI$_3$ thin films (illustrated in Figure 3.36). We found that the photocurrent of SbI$_3$ thin films increases with the iodization time. It might be because of the better surface morphologies of these films which they attained for higher iodization times. Also, the role of good crystallinity of the samples is worthy to note.

Sensitivity is one of the significant parameters for a photodetector. It was calculated according to equation (12). For investigating its sensitivity towards different wavelengths of the incident light (Figure 3.37), the device was irradiated with LEDs having different wavelengths. Sensitivity values for SbI$_3$ thin films (iodized for 120 s) of 30 min, 1 h, and 2 h deposited Sb$_2$S$_3$ films are tabulated in Table 3.3.
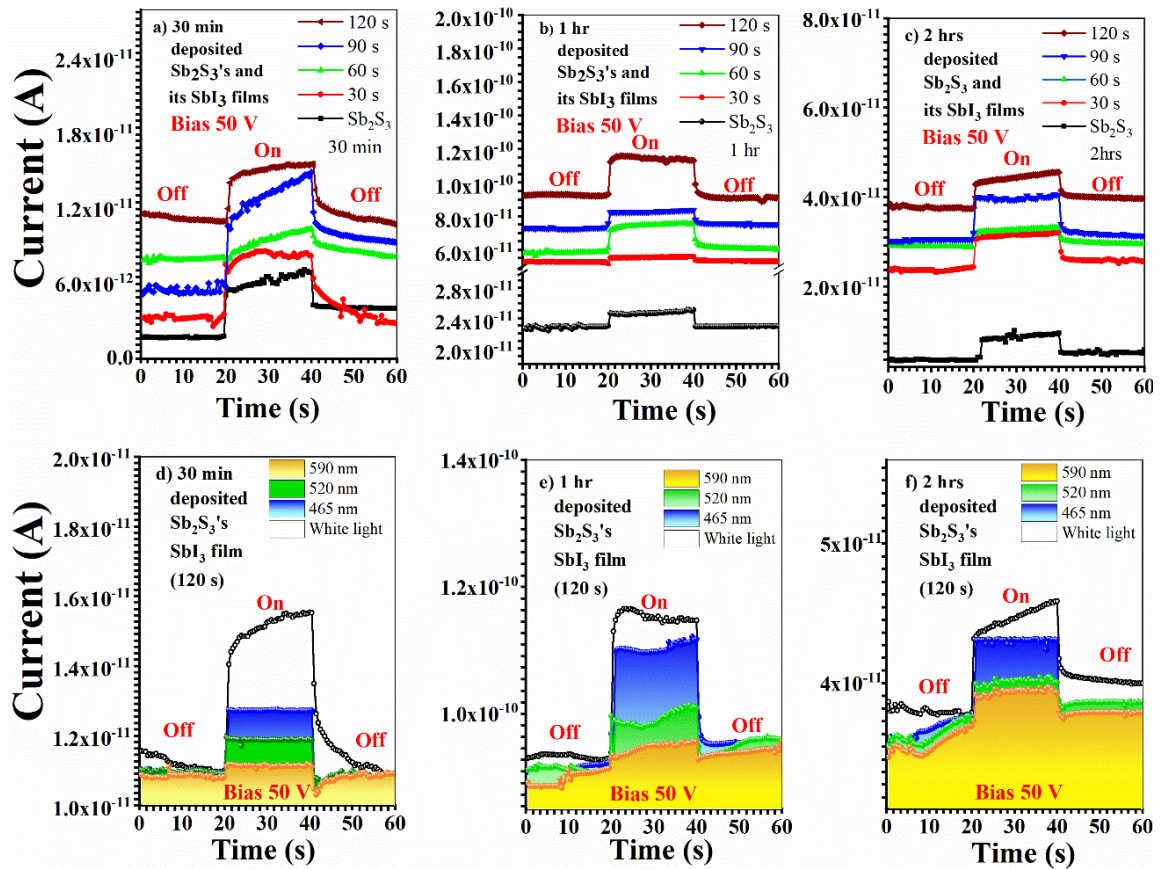
Figure 3.36. Photocurrent response of a) 30 min deposited Sb_2S_3 and its SbI_3 thin films, b) 1 h deposited Sb_2S_3 and its SbI_3 thin films, and c) 2 h deposited Sb_2S_3 and its SbI_3 thin films (with different iodization times: 30 s, 60 s, 90 s, and 120 s and illuminated with white light). I-t plot for d) 30 min deposited Sb_2S_3 and its SbI_3 thin films, e) 1 h deposited Sb_2S_3 and its SbI_3 thin films, and f) 2 h deposited Sb_2S_3 and its SbI_3 thin films (with 120 s of iodization and illuminated with LEDs of different wavelengths).

Table 3.3. Sensitivity measurements of SbI_3 thin films.

Sample (SbI_3)	Wavelength (nm)	I_{dark} (I_d) (nA)	I_{light} (I_l) (nA)	$(I_l-I_d)/I_d*(100)$ (%)
30 min 120 s	465	0.010	0.0127	15
	520	0.011	0.0119	8
	590	0.011	0.0114	3
1 h 120 s	465	0.090	0.11	20
	520	0.091	0.098	7
	590	0.09	0.095	5
2 h 120 s	465	0.036	0.044	22
	520	0.035	0.04	14
	590	0.035	0.039	11

For any photodetector device performance, its reproducibility, stability and response time must be taken into account as crucial evaluating parameters. Thanks to the crystallinity and uniform surface coverage with less voids of films, our device showed good reproducibility and stability (Figure 3.38).
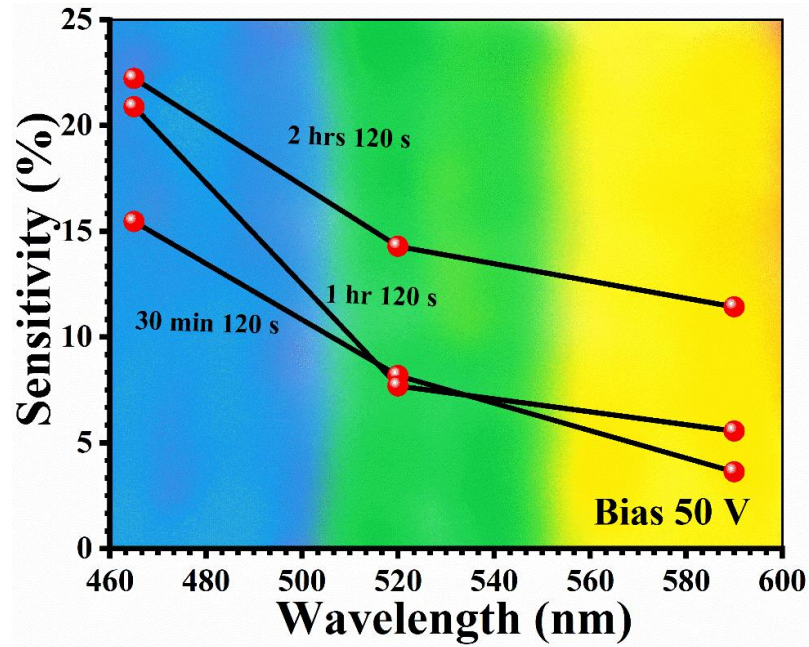
Figure 3.37. The sensitivity of SbI$_3$-photodetector towards light of different wavelengths.
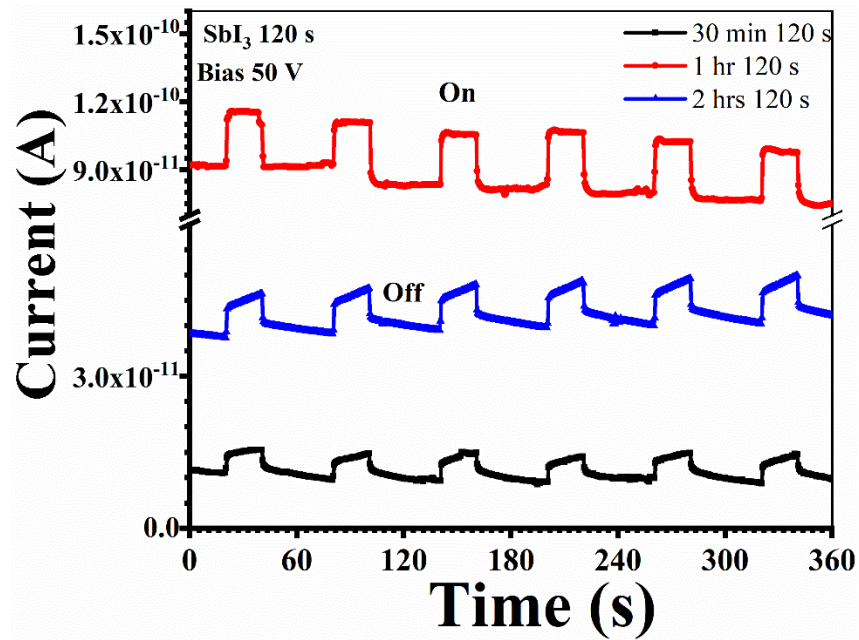
Figure 3.38. Switching behavior of SbI$_3$-photodetector when illuminated with white light.

The time required by the photodetector device to reach 90% of its maximum photocurrent value from its dark current is known as rising time (τ_{rise}). In contrast, the decay time (τ_{decay}) is the device's time to reach 10% of its maximum photocurrent. It is found that iodide film

of 2 h deposited Sb_2S_3 has better response time compared to others. Figure 3.39 portraits the rising and falling edges of SbI_3 photodetector under white light illumination. The photocurrent values are divided by the maximum photocurrent value obtained (normalized current) and are utilized for the I-t graph for the response speed calculation.
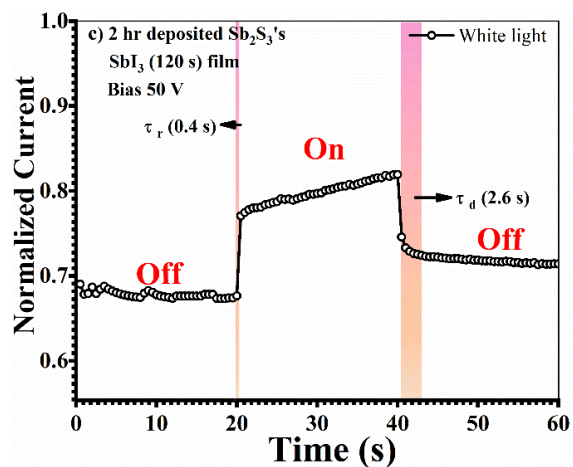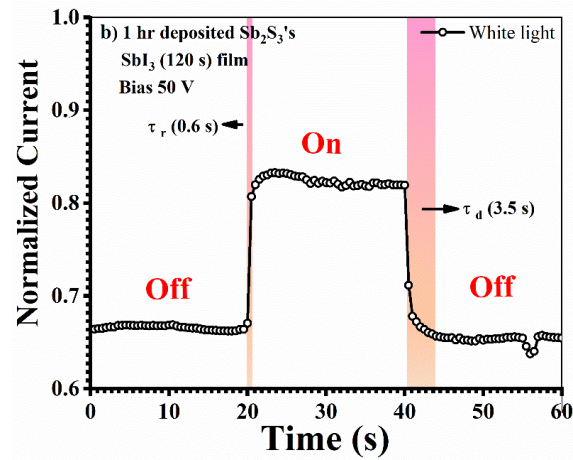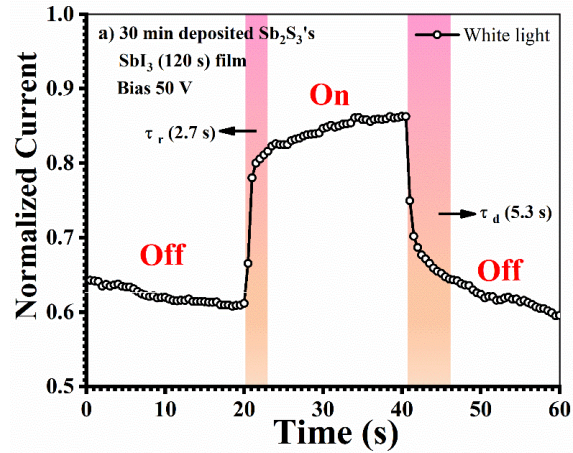
Figure 3.39. Rise and fall times of SbI$_3$ photodetector when illuminated with white light.

3.6. Conclusions of the chapter

In summary, XRD revealed a rhombohedral structure for BiI$_3$ with preferential growth along (003) direction. A photodetector based on BiI$_3$ was developed and its photocurrent responses were measured for different wavelengths of LEDs. The device performed well in the visible region with good reproducibility and sensitivity. The device responsivity towards different power densities were investigated. The sensitivity as well as responsivity of the device was affected by wavelength of incident light and power densities. Further, phase pure SbI$_3$ thin films were fabricated via rapid iodization of chemically deposited Sb$_2$S$_3$ thin films and a photodetector device was developed. The effect of Sb$_2$S$_3$ film thickness and iodization time on the structure, morphology, composition, and optoelectronic properties of SbI$_3$ revealed that the properties are tunable by precursor film thickness and iodization time. Also, polycrystalline, phase pure hexagonal AgI and zinc blend CuI thin films were deposited by combining thermal evaporation followed by rapid iodization methods. The structure, phase, morphology, elemental and optical properties were investigated as a function of precursor film thickness. Both AgI and CuI films showed high visible region transparency and the fabrication method we employed resulted in uniform films.

Chapter 4

Fabrication of Ag₂BiI₅ perovskite thin films for photodetector application

4.1. Introduction

In this chapter, the fabrication and properties studies of silver bismuth iodide (SBI) perovskite films are described. The structure, morphology, optoelectronic properties of Ag₂BiI₅ perovskite are investigated. The impact of precursor concentration on its properties are studied. Ag₂BiI₅ perovskite was used for the development of a photodetector device and the electrical measurements were done using LEDs. This thesis chapter has been published and reproduced with kind permission from Elsevier.

4.2.   Results and discussion

4.2.1.   Structure

Diffraction profile for pristine and annealed films of Ag₂BiI₅ perovskite is illustrated in Figure 4.1 (a and b). All the data are compared with the standard data base of Ag₂BiI₅ (JCPDS # 00-035-1025) perovskite. The diffraction peak positions are matching well with the standard file for hexagonal Ag₂BiI₅. Diffraction peaks situated at 2θ: 12.83°, 23.94°, 25.74°, 29.30°, 39.04°, 41.60°, 43.76° and 52.91° are corresponding to the reflections from the planes: (003), (101), (006), (104), (009), (110), (113) and (0012). All the as-deposited films show precursor peaks. After annealing (140˚C, 0.5 h), the precursor's diffraction peak intensity is reduced. Previous studies related to the Ag₂BiI₅ perovskite also revealed the presence of unreacted precursor in its structure[218,219]. To investigate whether the BiI₃ concentration variation results in another phase formation we did a structural study for all the cases. Despite of the variation in concentration, Ag₂BiI₅ is the

resulted phase. Table 4.1 shows the information about the synthesis method, sample form, and crystal structure of the reported Ag_2BiI_5 perovskites and are compared with the present study.

Crystallite sizes for all the cases were calculated using the Debye-Scherrer equation ((8), see section 2.5.1). Peak of (003) plane was considered for the size calculations. 54.7, 46.7, 41, and 37.2 nm are the obtained crystallite size values for 1:1, 1:0.95, 1:0.75, 1:0.45 cases respectively. The values are in the reported range with the previous studies[218]. The crystallite size increases with BiI_3 concentration and is portraited in Figure 4.1 (c).
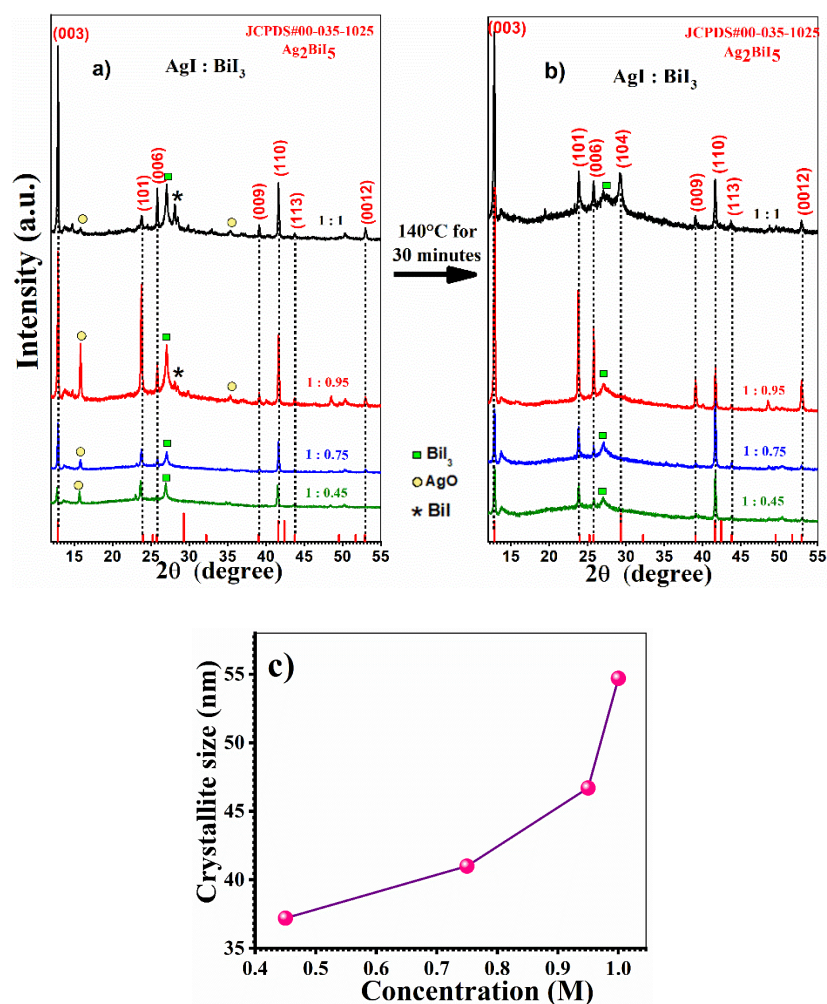
Figure 4.1. XRD patterns of the pristine and annealed ((a) and (b)) Ag_2BiI_5 perovskite thin films and c) crystallite size versus bismuth iodide concentrations (0.45, 0.75, 0.95 and 1 M). Graphs are reused with the permission from Elsevier in regard to our kind request, doi.org/10.1016/j.mtcomm.2020.101092.

Table 4.1. Comparison of the XRD results of present study with the earlier studies. Reused with the acceptance from Elsevier in regard to our kind request, doi.org/10.1016/j.mtcomm.2020.101092.

	Preparation method	Sample form	Crystal structure and impurity present in the sample
Present study	Spin coating	Film	Ag_2BiI_5 (hexagonal phase), impurity-BiI_3.
Mashadieva et al.[220]	Solid state reaction of AgI and BiI_3	Powder	Ag_2BiI_5(hexagonal phase).
Jung et al.[219]	Solid state reaction of AgI and BiI_3	Powder	Ag_2BiI_5 (hexagonal phase), impurity: BiI_3.
Zhu et al.[90]	Spin coating	Film	Ag_2BiI_5(hexagonal phase) impurity: Bi compositions
Turkevych et al.[91]	Melt solidification	Powder	Ag_2BiI_5 , impurity: AgI.
Hosseini et al.[218]	Spin coating	Film	Ag_2BiI_5(hexagonal phase), impurity: BiI_3 and AgI

4.2.2. Structure and phase
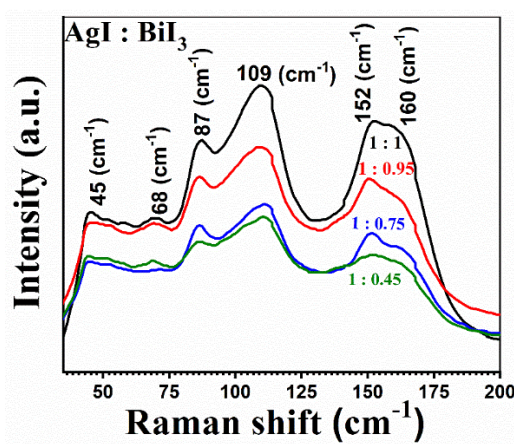
Figure 4.2. Raman spectral patterns of Ag_2BiI_5 perovskite films (AgI:BiI_3=(1:0.45, 1:0.75, 1:0.95 and 1:1 M). Graphs are reused with the acceptance from Elsevier, doi.org/10.1016/j.mtcomm.2020.101092.

Figure 4.2 shows the Raman spectra of Ag_2BiI_5 perovskite films. The peaks are appeared at wavenumbers: 45, 68, 87, 109, 152 and 160 cm^{-1}. Compared to AgI and BiI_3, Ag_2BiI_5 perovskites reveal new peaks at 68 and 160 cm^{-1}. These lines might be due to the asymmetric stretching of iodine atoms[221]. Rest of the lines show a shift in the Raman peak positions when compared to AgI and BiI_3 powders. The peak: 87 cm^{-1} corresponds to the E_g mode of BiI_3[174] (unreacted precursor) and this result correlates with our XRD results. There is a similarity in the spectrum of each case. The shift in the peak positions and the arrival of new peaks can be treated as an indication of Ag_2BiI_5 perovskite phase.

4.2.3. Morphology

The as prepared and annealed film's surface morphologies are captured using FESEM (illustrated in Figure 4.3). An acceleration voltage of 2 kV was applied. The magnified (magnifications of 10 k and 25 k) images are shown in inset of each micrograph. The surface morphology of 1:1 case is illustrated in Figure 4.3 (a) and (b). The as-prepared film surface comprises plane like particles and annealed film consists of a uniform distribution of rod-shaped-brighter particles. For 1:0.95 film (Figure 4.3 (c and d)), we observed that as prepared film morphology is composed of randomly arranged particles on its surface and the annealed film resembles the morphology of 1:1 film.
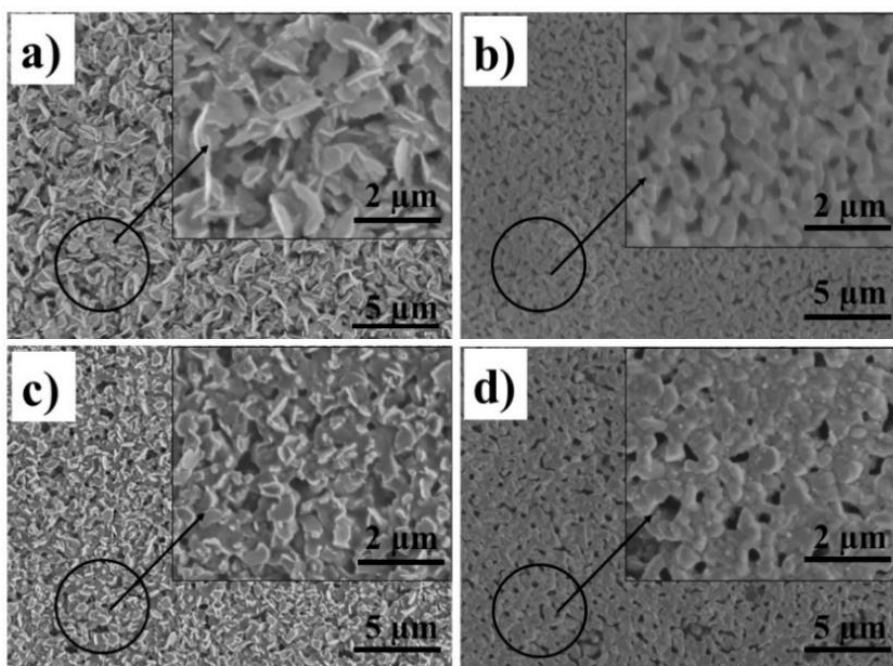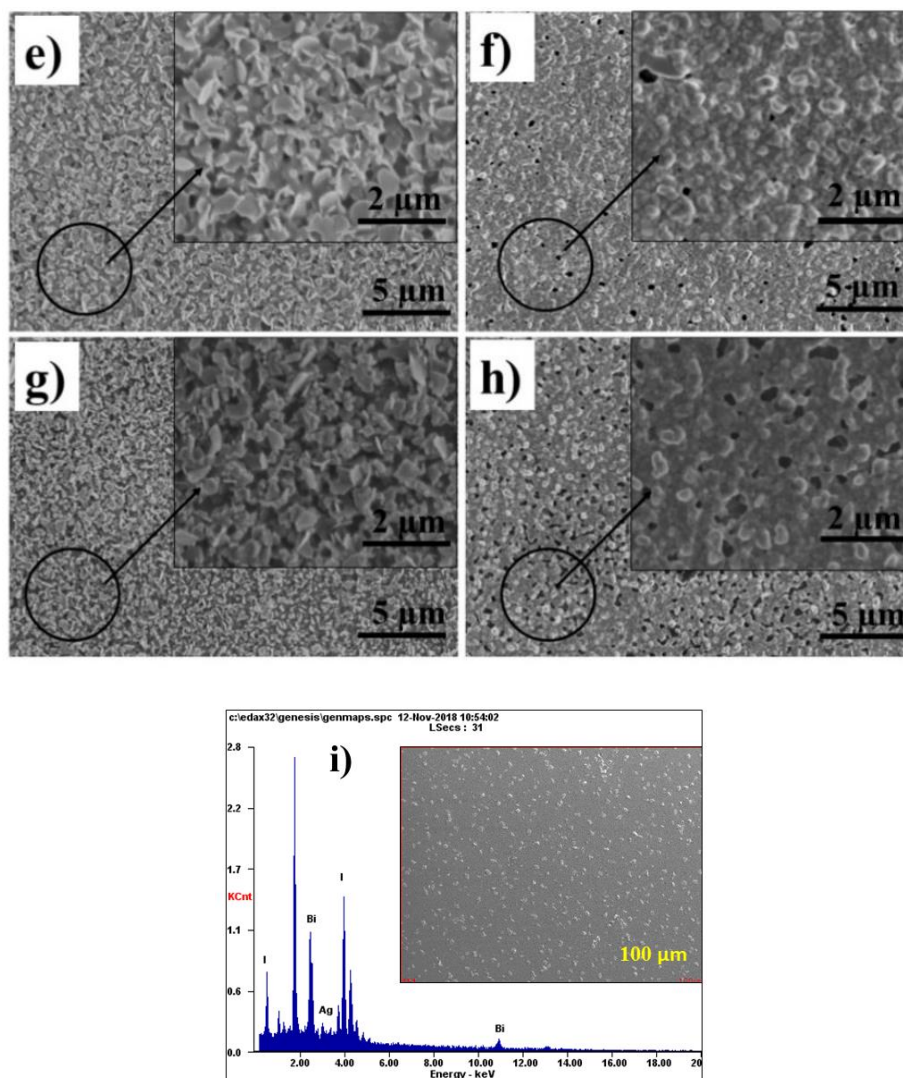
Figure 4.3. FESEM images of Ag_2BiI_5 perovskite thin films ($AgI:BiI_3$). As deposited films (a, c, e, and g) and annealed films (b, d, f, and h) of 1:1, 1:0.95, 1:0.75, 1:0.45 concentrations, i) EDS analysis of 1:1 film (doi.org/10.1016/j.mtcomm.2020.101092).

The surface morphologies for 1:0.75 and 1:0.95-as prepared are similar (Figure 4.3 (e)). The surface morphology of annealed-1:0.75 film consists of (Figure 4.3 (f)) spherical particles. The pristine-1:0.45 film (Figure 4.3 (g)) is composed of spherical particles. In contrast its annealed film morphology (Figure 4.3 (h)) comprises voids and randomly distributed particles. Each heat-treated film has a different morphology and the morphology of BiI_3 film is entirely different from the Ag_2BiI_5 perovskite thin films indicating the formation of new structures. Various kinds of morphologies have been reported so far in the previous studies related to Ag_2BiI_5 phase. For example, Zhu et *al*.

reported square-and flat-shaped clusters of particles for the Ag_2BiI_5 phase[90]. Hosseini and co-workers reported that Ag_2BiI_5 film surface is composed of non-uniformly distributed agglomerated particles[218]. Khadka et *al*. observed that the antisolvent vapor assisted annealing resulted in improved surface morphology of films[222]. EDS analysis of our Ag_2BiI_5 (1:1) film is given in Figure 4.3 (i). From the spectrum Ag, I and Bi elements were detected. The low solubility of AgI precursor causes the deficiency of Ag in the perovskite structure.

4.2.4. *Elemental composition and chemical state*

XPS analysis was conducted for the compositional and surface state studies of our perovskite. An area ratio of 3:2 and 4:3 (for 3d and 4f respectively) was maintained during peak fitting. Figure 4.4 shows the survey spectra of precursor powders, films and perovskite films. The survey pattern of Ag_2BiI_5 film reveals the elements: Ag, Bi, I, and C on its surface. As precursor concentration increases the peak intensities of Bi 4f and I 3d also increase. The peak intensity of Ag 3d in SBI is low compared with AgI powder. Low solubility of AgI and its resultant deficiency might be the reason for the Ag 3d peak intensity reduction. High-resolution spectra of annealed Ag_2BiI_5 perovskite film (with 1:1 case) is given in Figure 4.5.
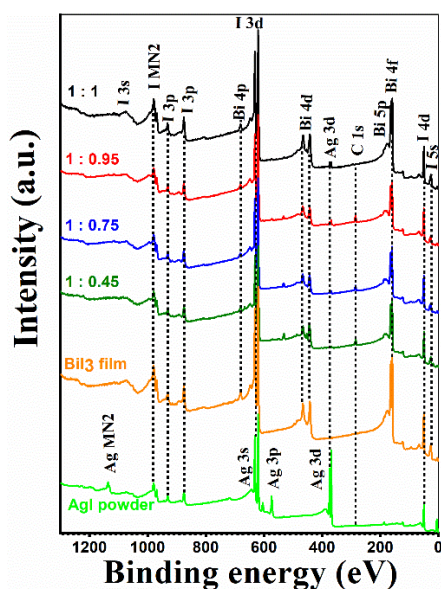
Figure 4.4. Comparison between the survey patterns of the precursors and Ag_2BiI_5 perovskite (doi.org/10.1016/j.mtcomm.2020.101092).

Figure 4.5. starts with the Ag 3d core level spectrum that consists of a doublet at 368.23 eV and 374.23 eV binding energy values (Ag $3d_{5/2}$ and Ag $3d_{3/2}$). These values are corresponding to +1 state of Ag in Ag_2BiI_5 perovskite. High-resolution spectrum of Bi 4f core level spectrum is composed of two singlets, namely, Bi $4f_{7/2}$ and Bi $4f_{5/2}$ and their corresponding B.E. values are 159.09 and 164.4 eV. These B.E. values show the +3 state of Bi in the perovskite. The high-resolution spectra of I 3d at 619.25 and 630.77 eV are assigned to -1 oxidation state of I in Ag_2BiI_5. The characteristic peak B.E., FWHM, area ratio values of the perovskite are compared with the precursors and listed in Table 4.2.
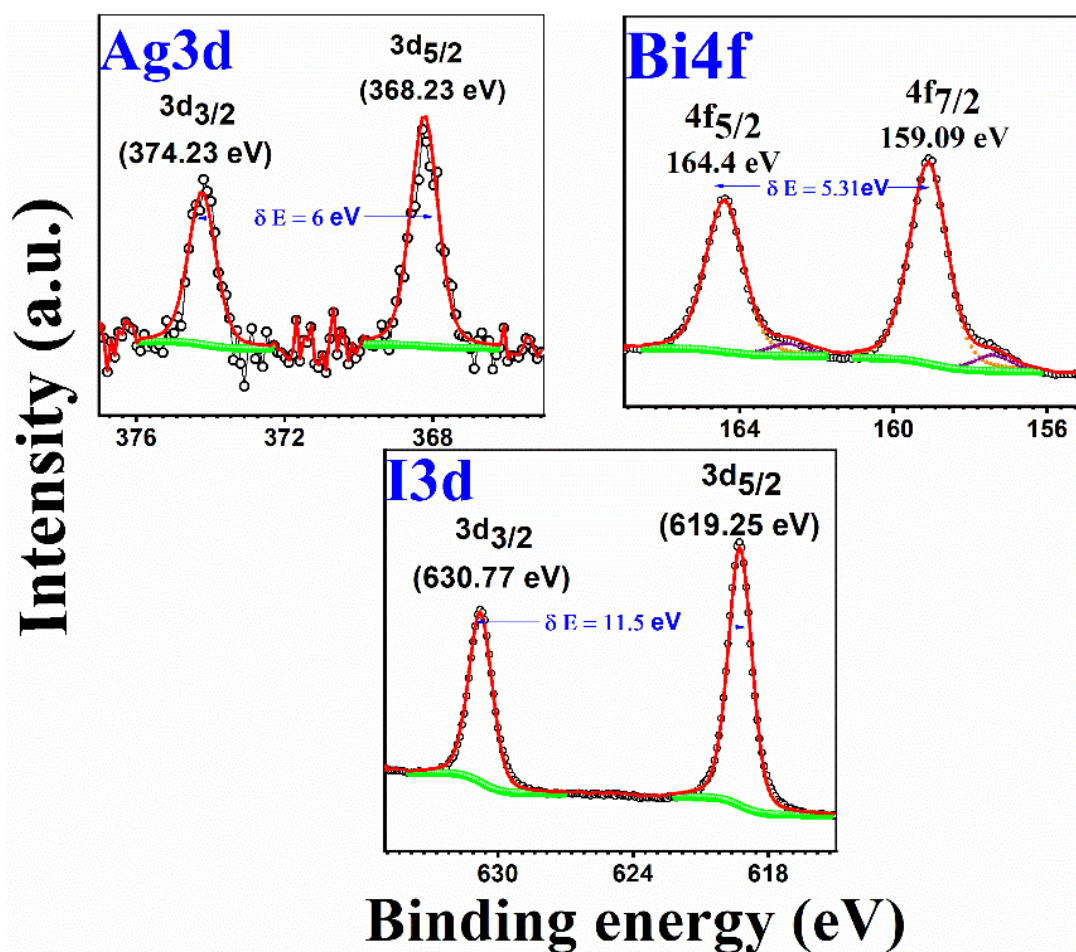
Figure 4.5. XPS high-resolution spectra of the Ag_2BiI_5 perovskite (1:1 case). (doi.org/10.1016/j.mtcomm.2020.101092).

Table 4.2. The compound, peak binding energy, FWHM, area ratio and chemical states for the corresponding deconvoluted peaks of precursors and Ag_2BiI_5 perovskite (doi.org/10.1016/j.mtcomm.2020.101092).

Sample	Peak	Position (eV)	Element	FWHM (eV)	Area ratio	Chemical state
AgI (powder)	Ag 3d	368.2	Ag 3d$_{5/2}$	0.88	1	Ag$^+$
	Ag 3d	374.2	Ag 3d$_{3/2}$	0.88	0.66	Ag$^+$
	I 3d	619.51	I 3d$_{5/2}$	1.19	1	I$^-$
	I 3d	631.01	I 3d$_{3/2}$	1.19	0.66	I$^-$
BiI$_3$ (powder)	Bi 4f	159.28	Bi 4f$_{7/2}$	1.05	1	Bi^{3+}
	Bi 4f	164.59	Bi 4f$_{5/2}$	1.05	0.75	Bi^{3+}
	I 3d	619.4	I 3d$_{5/2}$	1.29	1	I$^-$
	I 3d	630.9	I 3d$_{3/2}$	1.29	0.66	I$^-$
BiI$_3$ (film)	Bi 4f	159.29	Bi 4f$_{7/2}$	1.05	0.64	Bi^{3+}
	Bi 4f	164.6	Bi 4f$_{5/2}$	1.05	0.48	Bi^{3+}
	I 3d	619.47	I 3d$_{5/2}$	1.25	1	I$^-$
	I 3d	630.97	I 3d$_{3/2}$	1.25	0.66	I$^-$
Ag$_2$BiI$_5$ (film)	Ag 3d	368.23	Ag 3d$_{5/2}$	0.88	1	Ag$^+$
	Ag 3d	374.23	Ag 3d$_{3/2}$	0.88	0.66	Ag$^+$
	Bi 4f	159.09	Bi 4f$_{7/2}$	1.15	1	Bi^{3+}
	Bi 4f	164.4	Bi 4f$_{5/2}$	1.15	0.75	Bi^{3+}
	I 3d	619.25	I 3d$_{5/2}$	1.24	1	I$^-$
	I 3d	630.77	I 3d$_{5/2}$	1.24	0.66	I$^-$

A comparison between the etched and unetched samples high-resolution spectra is shown in Figure 4.6 (at the top)). Figure 4.6 (at the bottom) shows the depth profile analysis of Ag$_2$BiI$_5$ perovskite. The spectra altogether composed of the constituent elements' (Ag, Bi and I) profiles. Ag$_2$BiI$_5$ film was removed by Argon ions in each cycle during the etching process. After the first cycle of etching, metallic bismuth is detected. The depth profile analysis of Ag 3d level shows its uniform distribution for the first 7th levels. Bi 4f level's depth profile reveals the metallic peaks of Bi. It might be due to the argon induced effects. I 3d level's depth profile displays its uniform distribution till the seventh level (similar to Bi 4f level). In short, our perovskite depth profile analysis

confirms the even distribution of its constituent elements until the seventh level. The Ag_2BiI_5 was the main phase in the present study regardless of precursor concentration. Similar results related to the Ag_2BiI_5 perovskite formation (at non-stoichiometric conditions) have been reported in the previous reports[93,218,219,223]. Compositional results obtained from XPS and EDS are listed in Table 4.3.
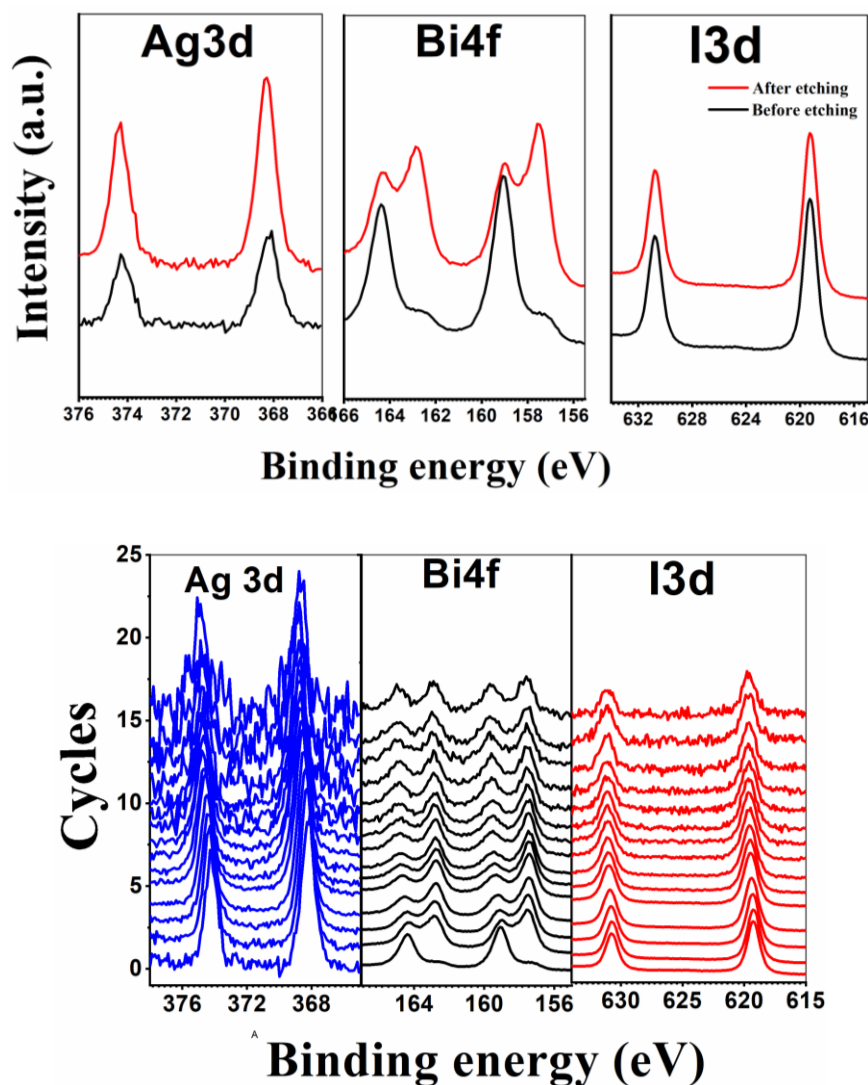
Figure 4.6. Comparison between the high-resolution spectra of the Ag_2BiI_5 perovskite (before and after etching (at the top)) and depth profile analysis (at the bottom). (doi.org/10.1016/j.mtcomm.2020.101092).

Table 4.3. Atomic percentage values of constituent elements obtained from EDS and XPS analysis (1:1 film). (doi.org/10.1016/j.mtcomm.2020.101092).

	EDS analysis	XPS analysis
Element	Atomic percentage (%)	Atomic percentage (%)
Ag	4.30	3.85
I	67.16	68.32
Bi	28.15	27.83

4.2.5. *Optical properties*

The optical properties of the Ag_2BiI_5 perovskites were investigated from their respective absorption spectra. Figure 4.7 (a) displays the absorbance spectra of all the pristine films. Films show absorption edges around 570-590 nm. After annealing, a shift in the absorption spectra is observed with an absorption edge in the range of 800-690 nm (Figure 4.7 (b)). A sharp peak around 640-650 nm is found in all the cases and is a common characteristic of iodide compounds[224]. Oh et *al*. observed that $AgBi_2I_7$ perovskites have similar sharp peaks in their absorption spectrum[225]. 2.14 and 1.71 eV are the respected bandgap values obtained for pristine and annealed films (1:1 case). The bandgap variations with the BiI_3 concentration reveal that it decreases with an increase in the concentration of precursor. The improvement in crystallinity may be responsible for the reduction in bandgap for higher concentrations. A comparison has done between the bandgap values obtained in the present study with previous reports and are given in Table 4.4. The direct bandgap value (1.71 eV) suggests that Ag_2BiI_5 perovskites can fit well among the family of lead-free materials for different optoelectronic applications.
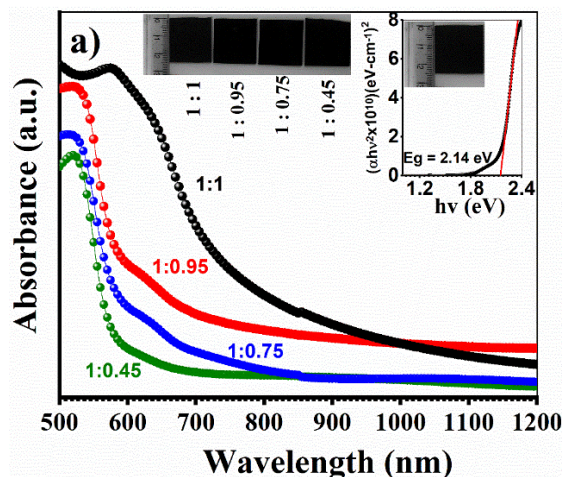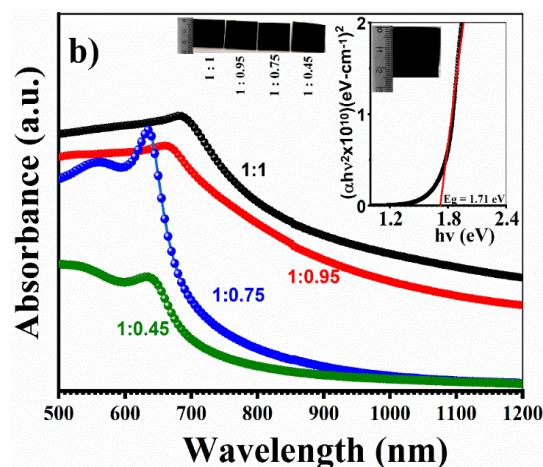
Figure 4.7. Optical absorption spectra of (a) as prepared (b) annealed Ag_2BiI_5 perovskites films. Tauc plot for 1:1 case is given in inset (doi.org/10.1016/j.mtcomm.2020.101092).

Table 4.4. Comparison between the bandgap values of the SBI in the present study with earlier reported results (doi.org/10.1016/j.mtcomm.2020.101092).

	Compound	Bandgap type	Bandgap values (eV)
Present study	Ag_2BiI_5	Direct bandgap	1.71
Jung et al.[219]	Ag_2BiI_5	Direct bandgap	1.83 and 1.88
Zhu et al.[90]	Ag_2BiI_5	Indirect and direct bandgap	1.62 and 1.85
Khazaee et al.[93]	Ag_2BiI_5	Direct bandgap	1.9
Hosseini et al.[218]	Ag_2BiI_5	Direct bandgap	1.38-1.6

4.2.6. Photodetector device

Based on the above results, a photodetector device was fabricated and is schematically illustrated in Figure 4.8 (a). Figure 4.8 (b) displays the photocurrent responses of SBI films. The highest photocurrent value is observed for 1:1 film. Improved crystallinity, surface morphology and appropriate band gap might be the reason behind this current value. The device was illuminated with LEDs of different wavelengths (50 W) and the corresponding photocurrent response was measured for 10 cycles to check the stability

and reproducibility. The photocurrent-voltage (I-V) characteristics are shown in Figure 4.9(a).
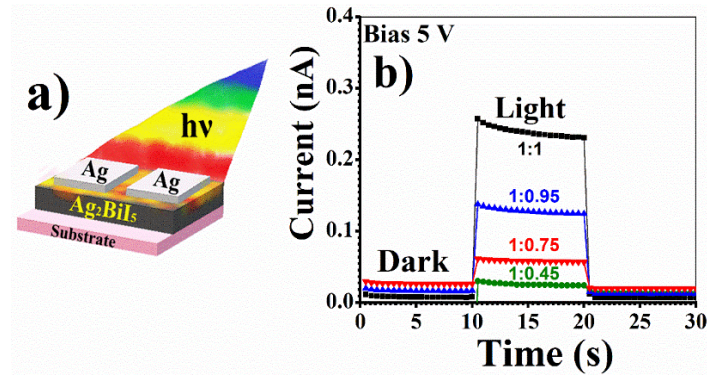
Figure 4.8. a) Schematic representation of the SBI photodetector b) I-t plot of SBI under illumination with tungsten lamp (doi.org/10.1016/j.mtcomm.2020.101092).
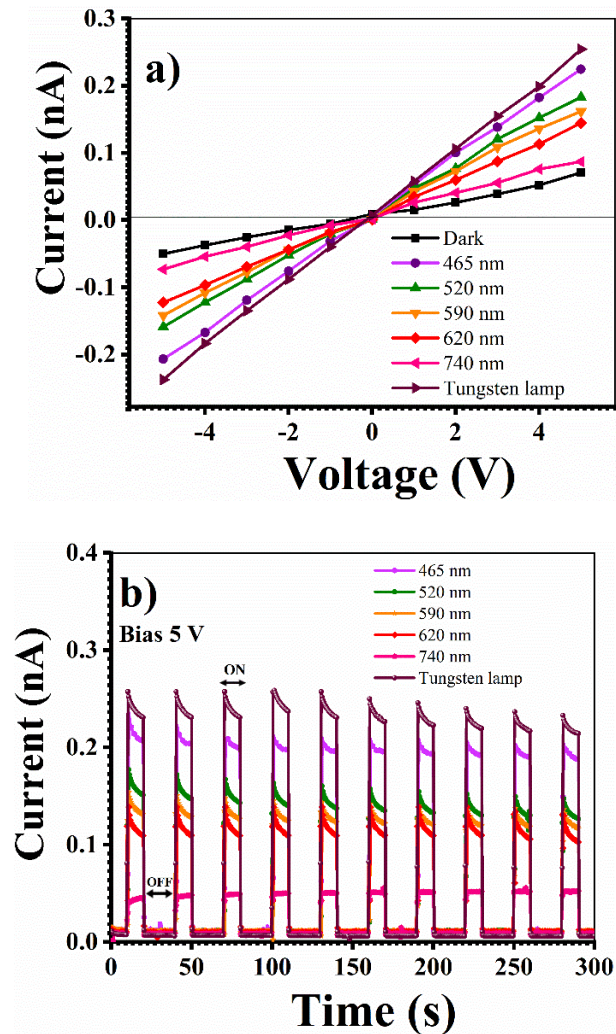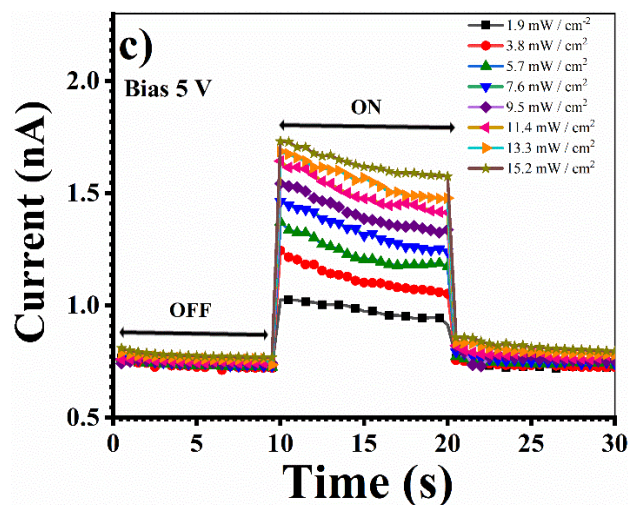
Figure 4.9.a) I-V curves under dark and illumination with different wavelengths of LEDs, b) switching behavior when the device was illuminated with different wavelengths of LEDs, and c) photocurrent response of the device when illuminated with different power densities of light (532 nm) (doi.org/10.1016/j.mtcomm.2020.101092).

The device detected a photocurrent when the light source was switched on. A bias voltage of 5 V was used in the entire measurement. Dark current values are detected in the range 0.007-0.019 nA whereas a noticeable photocurrent response in the range 0.049-0.234 nA is detected under illumination (given in Figure 4.9(b)).
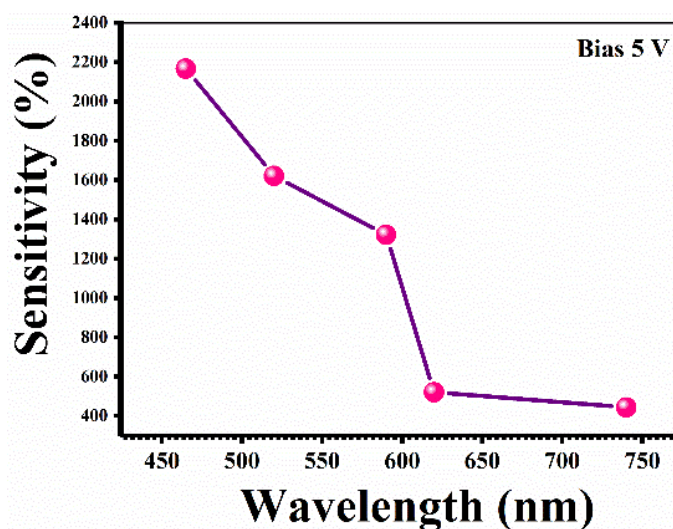
Figure 4.10. The sensitivity versus wavelength plot for Ag_2BiI_5 photodetector (doi.org/10.1016/j.mtcomm.2020.101092).

For any device, its stability and reproducibility are essential parameters for evaluating its performance. Thus, the device was illuminated with the light source which was alternatively turned on and off. The photodetector shows high reproducibility and stability during the switching process. The photodetector's sensitivity values towards different wavelengths of illumination from LEDs are calculated according to equation (4)(see section 1.5) and are tabulated in Table 4.5. The device shows good selectivity towards different wavelengths of light (Figure 4.10).

Table 4.5. Sensitivity values of Ag_2BiI_5 photodetector using LEDs of different wavelengths (doi.org/10.1016/j.mtcomm.2020.101092).

Wavelength (nm)	I_{dark} (nA)	I_{light} (nA)	Sensitivity (%)
465	0.009	0.204	2166.6
520	0.009	0.155	1622.2
590	0.009	0.128	1322.2
620	0.019	0.118	521.05
740	0.009	0.049	444.4
Tungsten	0.007	0.234	3242.8

Further, we calculated the photodetector's responsivity using the equation (3) (see section 1.5). Figure 4.9 (c) illustrates the photocurrent response corresponds to different power densities of light. Figure 4.11 displays the plot of the device's sensitivity and responsivity towards light of different wavelengths and the values are tabulated in Table 4.6.

Table 4.6. Sensitivity and responsivity values of SBI photodetector at different power densities of light (doi.org/10.1016/j.mtcomm.2020.101092).

Power density (mW / cm²)	I_{dark} (nA)	I_{light} (nA)	Sensitivity (%)	Responsivity (A / W) x 10^{-9}
1.9	0.7326	0.9741	32.96	506
3.8	0.7298	1.1017	50.95	389
5.7	0.7325	1.205	64.50	303

7.6	0.7406	1.3109	77.00	298
9.5	0.7461	1.3801	84.97	265
11.4	0.7494	1.476	96.957	254
13.3	0.7626	1.5687	105.70	241
15.2	0.7748	1.6138	108.28	220
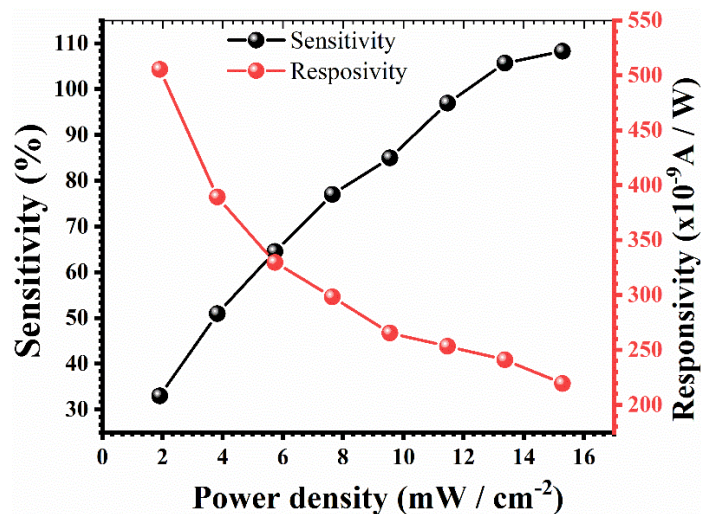
Figure 4.11. Sensitivity and responsivity of the SBI photodetector as a function of power density (doi.org/10.1016/j.mtcomm.2020.101092).

It is observed that the photocurrent increases with the intensity of incident light. In contrast, the responsivity decreases with an increase in light intensity. The reduction in responsivity of the device may be due to the non-uniform surface coverage and the presence of trap states. It leads to the recombination of carriers and suppression of the transportation of photocarriers[226–228].

4.2.7. Stability study

Further, we investigated the stability of Ag_2BiI_5 perovskite by exposing them to the open atmosphere for seven days. We observed a slow degradation of the samples after each day. Also, a color change was observed from black to grey. Compared to the smooth and shiny surface of freshly prepared films, 1-week old sample appeared with powdery surfaces. Structural stability studies are done by analyzing their XRD patterns (shown in Figure

4.12 (a)). It is evident from XRD results that almost all the peak intensities are reduced, the peak corresponding to (104) plane is vanished and the silver oxide peak is appeared. Figure 4.12 (b) portraits the surface morphology of the 1-week old sample (1:1 case). From morphology study, pinholes are observed, indicating the reduction in surface coverage.
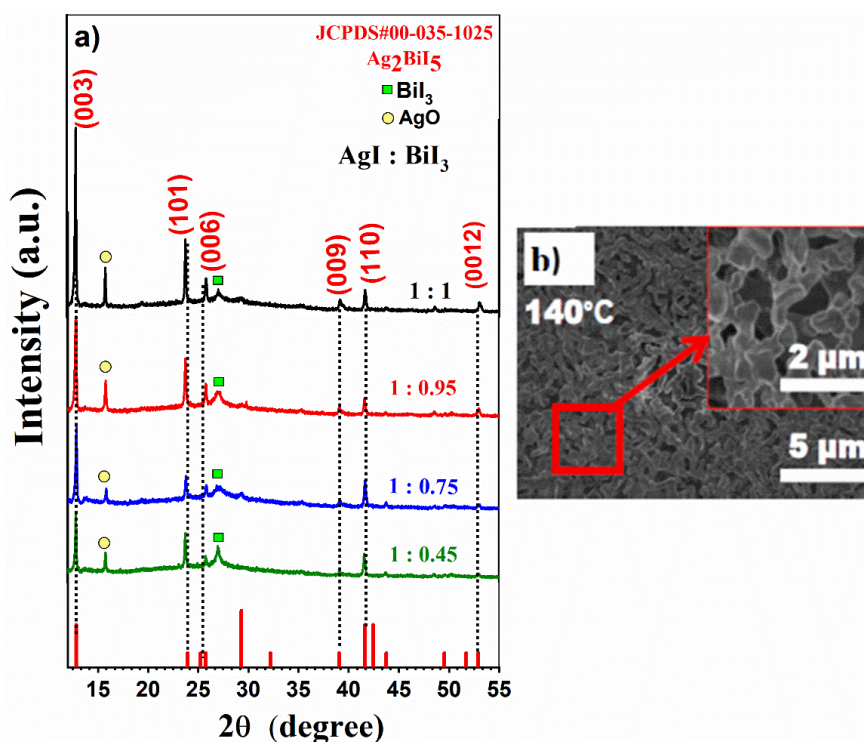
Figure 4.12. Seven days air exposed Ag_2BiI_5 perovskite thin film a) XRD pattern b) FESEM image (1:1 film) (doi.org/10.1016/j.mtcomm.2020.101092).

Based on the above-mentioned results we can summarize that the variation of precursor concentration effects on the structure, morphology, and optoelectronic properties of Ag_2BiI_5 perovskite. XRD results revealed the formation of the hexagonal-Ag_2BiI_5 phase. Raman spectra for the perovskite thin films confirmed the phases and structure present in the film. 1:1 case showed a uniform surface morphology with fewer voids. Better structure, morphology and optoelectronic properties were tunable by changing precursor concentration. A direct bandgap value of 1.71 eV was obtained for 1:1 film. A photodetector device was developed, and it showed excellent reproducibility,

stability, and sensitivity in the visible region. Thus, this lead-free perovskite has promising future for the optoelectronic and photovoltaic application.

Chapter 5

Fabrication of Cu_2BiI_5 perovskite thin films for photodetector application

5.1. Introduction

During this rapid development of silver bismuth iodides, as an alternative to Pb, copper also grabs more attention very recently. Its non-toxicity and high charge carrier mobility promote it to use in the replacement of lead[42,136] and so far studies related with copper bismuth iodide (Cu-Bi-I) perovskite system are less in number. Only a few studies related to $CuBiI_4$ perovskites are reported so far. The first report about $CuBiI_4$ was made by Fourcroy et *al.* in 1991 where they investigated the structure of $CuBiI_4$[88]. In 2018, Zhaosheng et *al.* synthesized $CuBiI_4$ by solution processing method using CuI and BiI_3 powders[95]. In the same year, Zhang et *al.* synthesized $CuBiI_4$ by an in-situ reaction of Cu-Bi alloy with I_2 at room temperature without using any organic solvent. A photovoltaic device with structure: ITO/$CuBiI_4$:Spiro-MeO-TAD/Au produced a PCE of 1.119%[74]. Thus, new synthesis techniques and their properties studies are necessary for the further development of this material. This chapter deals with the fabrication of copper bismuth iodide (CBI) thin films. The structure, phase, surface morphology, composition, optical properties of the Cu_2BiI_5 are investigated in detail. A photodetector device was developed based on copper bismuth iodide and the wavelength dependency of photocurrent is studied.

5.2. Results and discussions

5.2.1. Structure
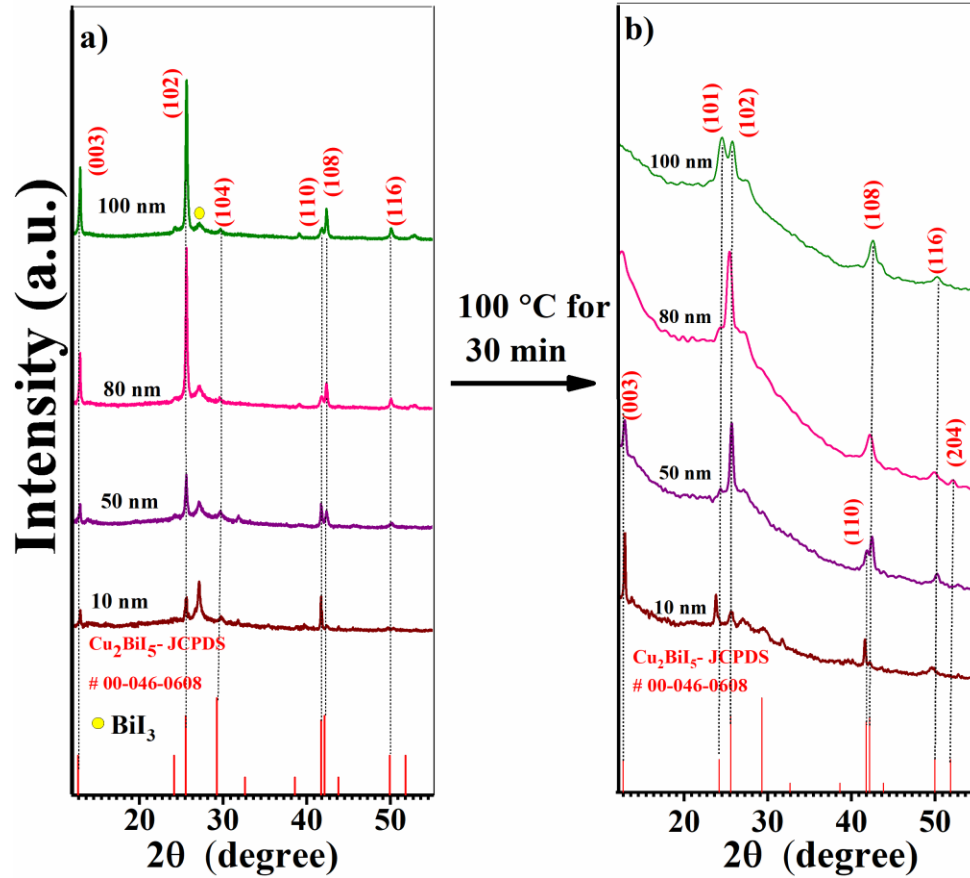
Figure 5.1. XRD patterns of a) as prepared and b) annealed CBI thin films with various copper thicknesses.

Figure 5.1 shows the diffraction patterns of as prepared and annealed CBI perovskite films with different copper thickness. XRD patterns of CBI thin films with various copper thicknesses are compared with the standard database with JCPDS number 00-046-0608. After the comparison with the standard databases of the Cu-Bi-I system, the diffraction peaks at 2θ values: 12.65°, 24.1°, 25.5°, 29.25°, 41.7°, and 42.11° are matching well with the hexagonal Cu_2BiI_5 structure. The as prepared CBI films have diffraction peaks at 2θ values: 12.65°, 25.5°, 29.25°, 41.7°, and 42.11° which are assigned to (003), (102), (104), (110), and (108) crystal planes. In addition to these diffraction peaks, a low intensity peak of BiI_3 is observed at 27.04°. Copper thickness has a vital role in the

crystallinity and the formation of Cu_2BiI_5 perovskite. For the lowest thickness of copper (10 nm) comparatively high intense diffraction peak of BiI_3 is detected. With the gradual addition of copper (50, 80, and 100 nm), diffraction peak intensity of BiI_3 at 27.04° is decreased considerably with the complete formation of Cu_2BiI_5. With the increase in copper thickness, the characteristic diffraction peaks of Cu_2BiI_5 at 2θ values: 12.65°, 25.5°, 42.11° show a gradual increment in intensity with the suppression of BiI_3 diffraction peak indicating the vital role of Cu thickness in the ternary perovskite formation.

Upon annealing of CBI thin films at 100 °C for 30 min, the diffraction peak at 12.65° disappears for the 100 nm case. New peaks appear at 24.1° for 10 and 100 nm cases of CBI films. Also, the diffraction peak at 41.7° vanishes for 80 and 100 nm cases. Interestingly all the annealed films show pure Cu_2BiI_5 phase without any binary phases (CuI or BiI_3), suggesting that annealing facilitates the removal of the BiI_3 impurity phase from the Cu_2BiI_5 perovskite structure. Our observations are matching with the annealing effect on the structure of silver bismuth iodide system and according to their study BiI_3 was removed entirely from the sample after annealing[93].

The reaction mechanism based on our experimental studies and Cu_2BiI_5 phase formation can be described as follows. We assume that the formation of copper iodide occurs when Cu reacts with iodine from BiI_3. An immediate reaction between this copper iodide and BiI_3 leading to the formation of Cu_2BiI_5 phase. The exact formation mechanism of Cu_2BiI_5 perovskites is still unknown and more relevant studies are necessary for a better understanding. Like Ag_2BiI_5: one formed via solid-state reaction irrespective of the precursor concentration[218,219,223], our Cu_2BiI_5 perovskite formation is also independent of the precursor composition. It is found that Cu_2BiI_5 is the dominant phase irrespective of copper thickness and our observations are matching with the studies related with Ag_2BiI_5 perovskites. The reaction mechanism that we proposed for Cu_2BiI_5 perovskites can be written as follows,

$$2\,Cu + I_2(from\ BiI_3)\ \rightarrow 2\,CuI \qquad (15)$$

$$2\,CuI + BiI_3 \rightarrow Cu_2BiI_5 \qquad (16)$$
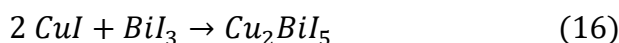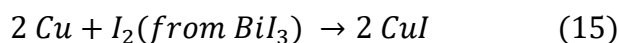
5.2.2. Structure and phase

Figure 5.2 shows the comparison between the Raman spectra of the as prepared and annealed CBI thin films. According to the present scenario, Raman spectra of the Cu-Bi-I system have not been reported so far. Four common peaks are detected in the Raman spectra and situated at 44, 52, 83, and 112 cm^{-1}. For both as prepared and annealed films, the most intense peak is located at 112 cm^{-1}. Raman peak at 150 cm^{-1} may be contributed from the second-order Raman line from BiI$_3$[174,175,229] and it disappears for the annealed samples. This result is in a good correlation with our XRD results. Compared to Raman spectra of precursor films, CBI perovskite thin films show a systematic shift in the position of peaks by one or two wavenumbers. These peak shifts can be considered as the formation of the ternary phase.
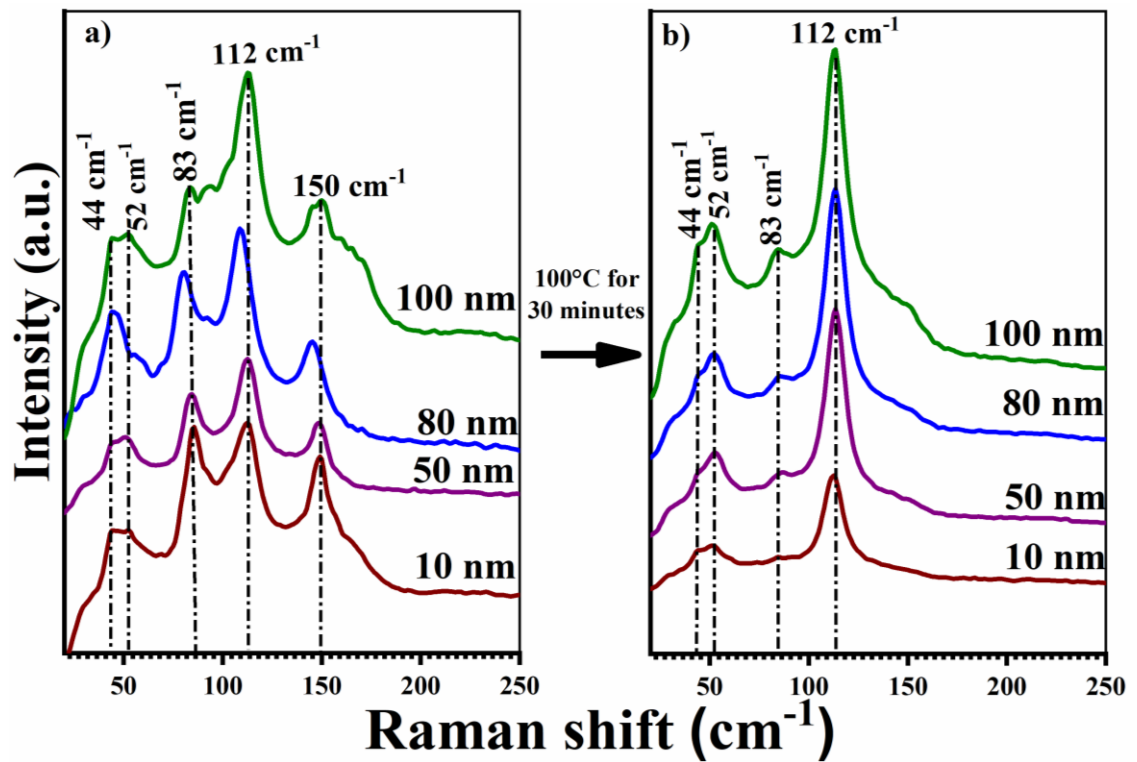
Figure 5.2. Raman spectra of a) as prepared and b) annealed CBI perovskite thin films.

5.2.3. Morphology

Surface morphologies of Cu_2BiI_5 perovskite thin films were taken using FESEM and the micrographs of pristine and annealed samples with their magnified images are given in the inset of Figure 5.3. All the images were taken with an acceleration voltage of 2 kV in the secondary electron mode (SE) at magnifications of 10 and 25 k.
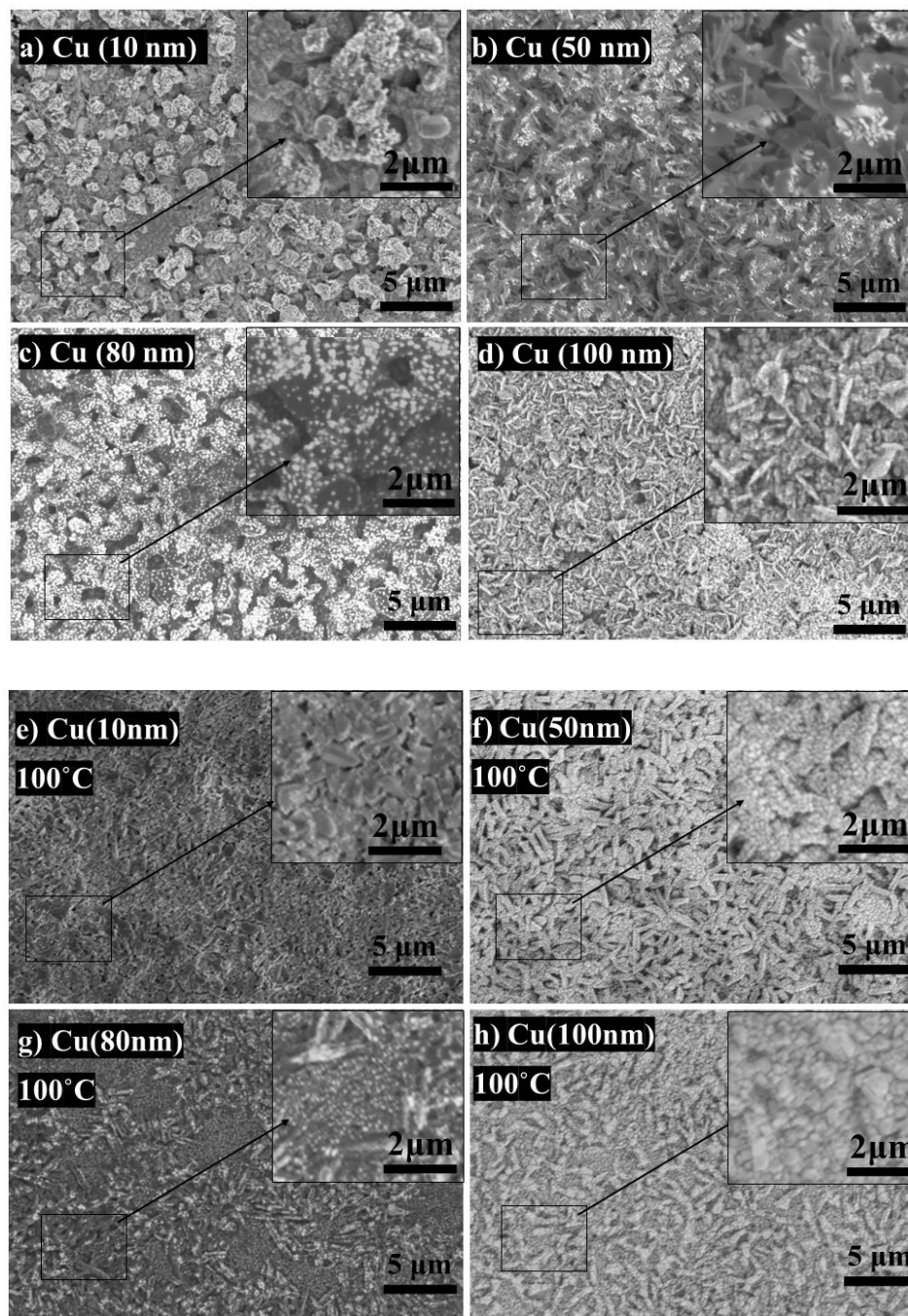
Figure 5.3. FESEM micrographs of Cu_2BiI_5 perovskite thin films formed with different Cu thicknesses, a) pristine 10 nm, b) pristine 50 nm, c) pristine 80 nm, and d) pristine 100 nm and films and e) annealed 10 nm, f) annealed 50 nm, g) annealed 80 nm, and h) annealed 100 nm.
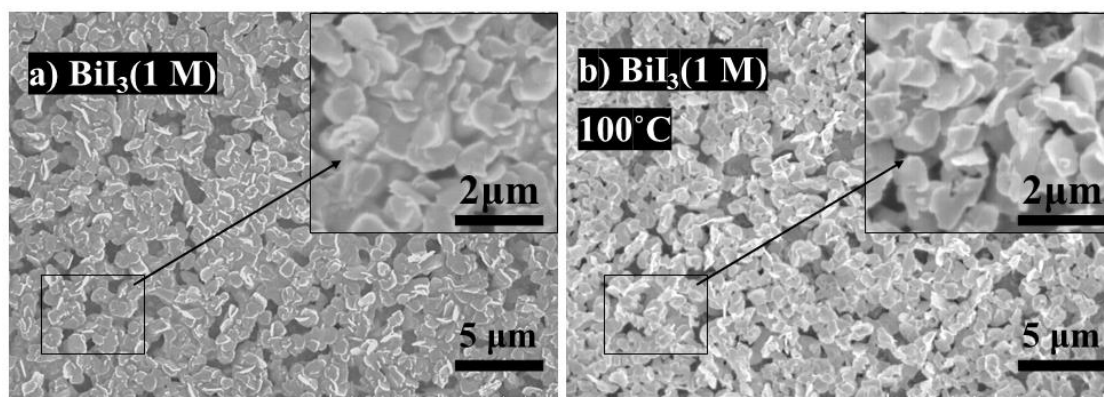
Figure 5.4. FESEM images of BiI_3 thin films a) pristine and b) annealed at 100˚C.

FESEM micrographs of pristine and annealed CBI perovskite thin films are compared. All the pristine films show distinct surface morphologies for different copper thicknesses. Figure 5.3 (a) shows the morphology of the CBI perovskite thin film with the lowest copper thickness (10 nm). It has a compact surface morphology with irregularly shaped agglomerated particles that are distributed randomly. For a 50 nm copper thickness case, the pristine CBI perovskite thin film reveals a better surface coverage and is composed of plane like structures (Figure 5.3 (b)). In the case of 80 nm, its surface morphology (Figure 5.3 (c)) is composed of corals-like agglomerated particles. As the copper thickness is increased to the highest value (100 nm) comparatively, compact surface morphology is observed (Figure 5.3 (d)). In this case, surface morphology is appeared as a compacted version of the 50 nm case surface, with plane like structures pointing out of the surface. When the copper content is increased surface morphology of CBI thin films is improved and became denser. The surface morphology of thin film has a crucial role when a semiconductor material is considered for application purposes. Because when the film has better surface coverage and compactness, the photoinduced charge carrier transfer will be enhanced, and it will reflect in the high performance of the device.

Surface morphologies of annealed CBI thin films are displayed in Figure 5.3 (e, f, g, and h). A completely different morphology is observed for annealed CBI film compared to the as prepared samples. The surface morphology of Cu_2BiI_5 perovskite thin film is affected by copper content and temperature. When 10 nm Cu CBI thin film was subjected to annealing, the surface morphology changes from shapeless particles into small rod-like structures (Figure 5.3 (e)). As we increased the copper thickness from 10 nm, that is, 50 to 100 nm, the surface becomes denser and compact for all the annealed samples (Figure 5.3 (f, g and h). From the SEM micrographs, it is understood that annealing promotes the reduction of BiI_3 impurity present in our samples. Because the surface morphology of BiI_3 films is (both pristine and annealed) composed of plane-like structures (Figure 5.4) and these kinds of structures are observed only for pristine CBI samples. It is evident from the SEM images of BiI_3 and CBI films that, the two-step deposition method for CBI thin films resulted in compact and homogeneous surface morphologies. Optoelectronic properties of the perovskites are highly influenced by their surface morphologies, one of the most important factors for solution-processed perovskite formation is concentrating on the overall surface coverage with least pinholes and voids[34]. Thus, our strategy of combining both spin coating and thermal evaporation methods resulted in good quality films with better surface coverage.
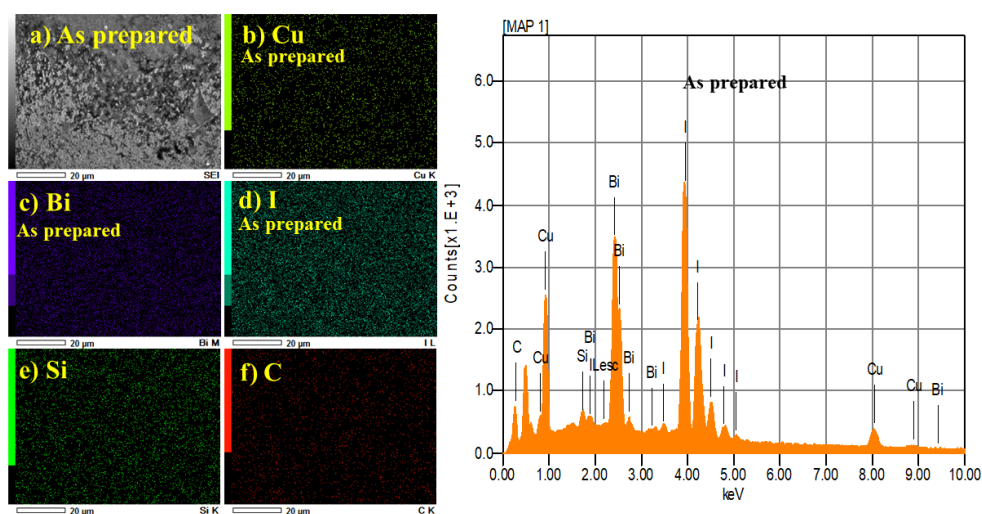
Figure 5.5. EDS mapping of as prepared Cu_2BiI_5 thin films with a Cu thicknesses of 80 nm.
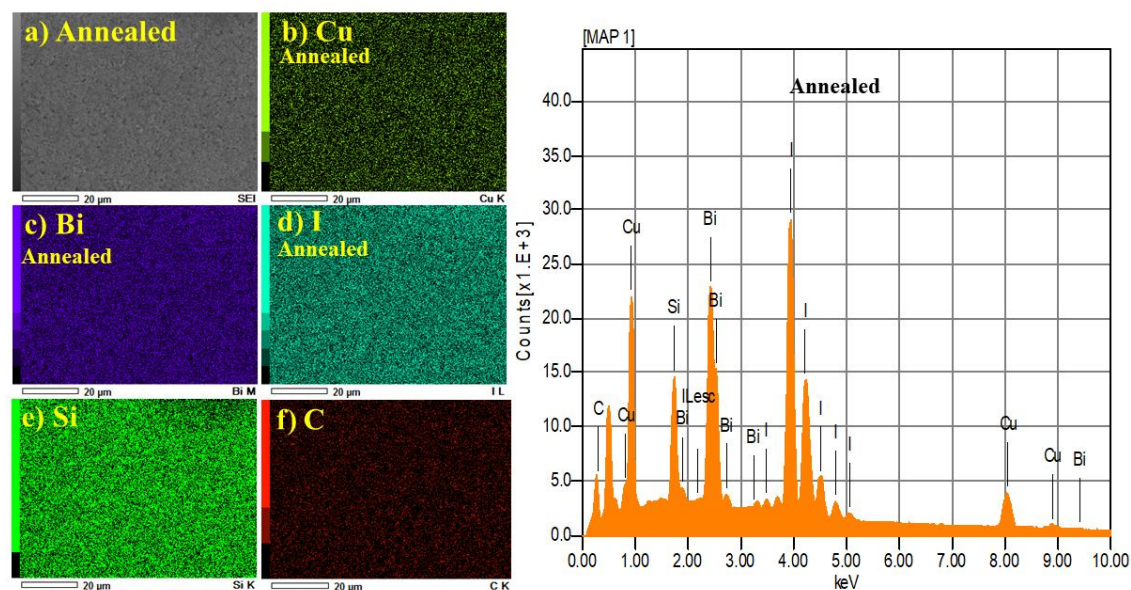
Figure 5.6. EDS mapping of annealed Cu_2BiI_5 thin films with a Cu thickness of 80 nm.

Energy dispersive X-ray mapping was done to study the elemental distribution and composition of as prepared as well as annealed CBI (80 nm) samples (Figure 5.5 and Figure 5.6). In the EDS analysis elements such as Cu, Bi, I, Si, and C are detected. We noticed that Cu, Bi and I are uniformly distributed over the film surface. Table 5.1 shows the atomic percentage values, Cu to Bi and I to Bi ratios.

Table 5.1. Atomic percentage of the elements: Cu, Bi, and I obtained from EDS mapping.

As prepared Cu_2BiI_5 perovskite				Annealed Cu_2BiI_5 perovskite			
Element	Atomic percentage	Cu/Bi ratio	I/Bi ratio	Element	Atomic percentage	Cu/Bi ratio	I/Bi ratio
Cu	10.70			Cu	15.18		
Bi	9.32	1.14	6.55	Bi	7.92	1.91	6.64
I	61.09			I	52.62		

5.2.4. Optical properties

Optical absorbance of all the CBI films were measured in the wavelength ranging from 500-2500 nm and the absorption spectra (of as prepared and annealed CBI thin films) are illustrated in Figure 5.7. We observed that the absorption spectra of as prepared CBI thin films have absorption edges in the Visible-NIR region around 632-911 nm. Annealed films show absorption edges in the onset around 710-810 nm. From the optical absorption spectra, it is evident that the black colored Cu_2BiI_5 perovskite thin films can absorb light from the visible to NIR region. This feature will help Cu_2BiI_5 perovskites to put their fingerprint for sunlight harvesting and other optoelectronic applications.
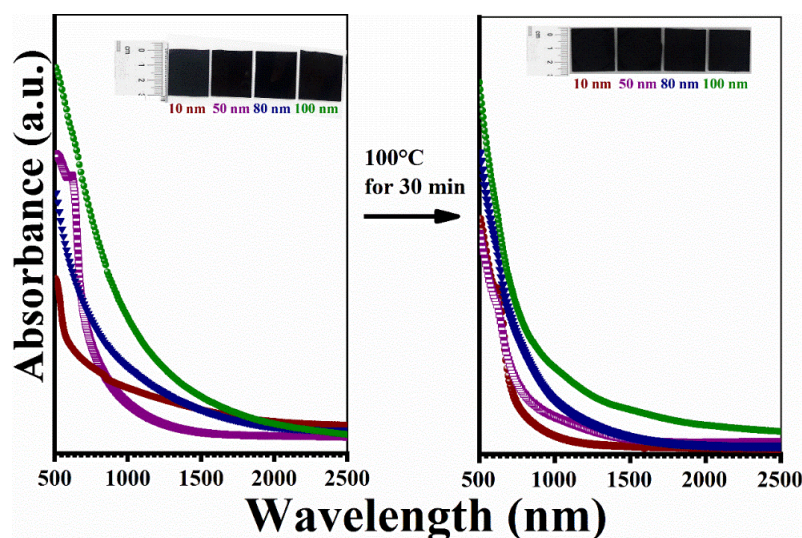
Figure 5.7. UV-Vis absorption spectra of as prepared and annealed CBI films with different copper thickness: 10, 50, 80, and 100 nm.
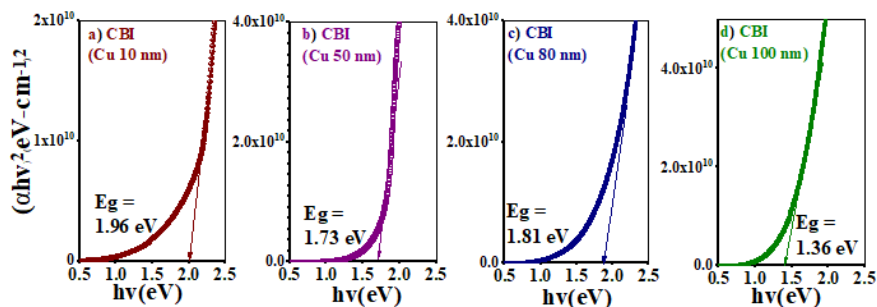
Figure 5.8. Direct Tauc plots for as prepared CBI films with different copper thickness: 10, 50, 80, and 100 nm.
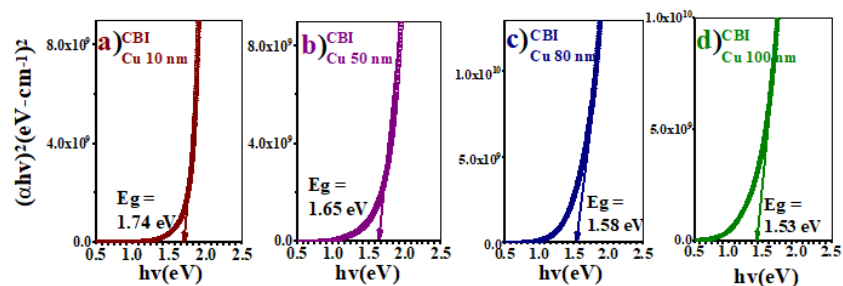
Figure 5.9. Direct Tauc plots for annealed CBI films with different copper thickness: 10, 50, 80, and 100 nm.

A good linear fit for $(\alpha h\nu)^2$ versus $h\nu$ is obtained for Cu_2BiI_5 perovskites implying that the allowed transition is direct. Direct bandgap values for all the cases are calculated from their respective Tauc plots and are given in Figure 5.8 and Figure 5.9. As prepared films show direct bandgap values (Figure 5.8) ranging from 1.96 to 1.36 eV, annealed films reveal values range from 1.74 to 1.53 eV (Figure 5.9). The wider bandgap values obtained for pristine CBI thin films might be due to the excess BiI_3 impurity phase. Also, for both as deposited and annealed films of Cu_2BiI_5 perovskite thin films, the bandgap values are tunable and by varying the copper thickness.

5.2.5. Photodetector device

The above-mentioned results motivated us to develop a Cu_2BiI_5 photodetector device. Ag electrodes with dimension 5×5 mm were painted using silver paint as shown in Figure 5.10(a). Photocurrent response of all the CBI thin films were examined by irradiating them with tungsten lamp and LEDs (465, 520 and 590 nm) at a bias of 0.2 V. All the samples were kept under dark for 10 minutes before measurements. A 20 s of time interval was programmed for measuring current in dark followed by illumination and again under dark conditions. Before the photocurrent measurements, the illumination from the light sources was guided carefully for getting the maximum coverage of the entire device area for better responses. The same dimension for Ag electrodes was maintained for all the CBI samples. As evident from Figure 5.11 that all the films are photoconductive. It is revealed from the figure that when excited with incident photons, the photocurrent

shows an increase under illumination and suddenly goes to a low value under dark conditions.

Reproducibility and stability are essential factors when considering the device's practical applications. Thanks to the compact morphology and good absorption in the Vis-NIR region of Cu_2BiI_5 perovskites, the photodetector showed high reproducibility and stability when irradiated with different wavelengths of light from LEDs (shown in Figure 5.12). The photocurrent response graphs of Cu_2BiI_5 photodetector produces a high photocurrent and returned to a low photocurrent value when the light is alternatively turned on and off. The device can operate at a lower bias voltage of 0.2 V. It is observed that CBI 10 case possesses a different photoresponse shape than other cases. It might be due to the lesser amount of copper atoms compared to other cases. As the copper concentration in the perovskite structure increases the effective electric field also increases. It causes the reduction in trapping of charge carriers[230] and leads to a high photocurrent value.
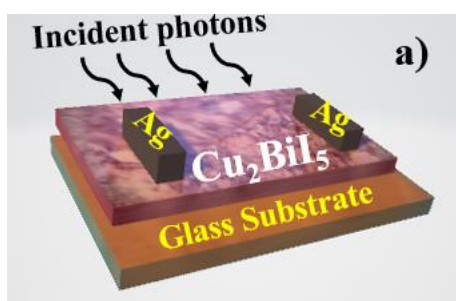
Figure 5.10. Schematic diagram of Cu_2BiI_5 photodetector.

Sensitivity is one of the important parameters of a photodetector and we calculated the device sensitivity towards different wavelengths of light using the equation (4) (see section 1.5) and is tabulated (Table 5.2). Figure 5.13 illustrates the wavelength-dependent sensitivity of Cu_2BiI_5 photodetector.
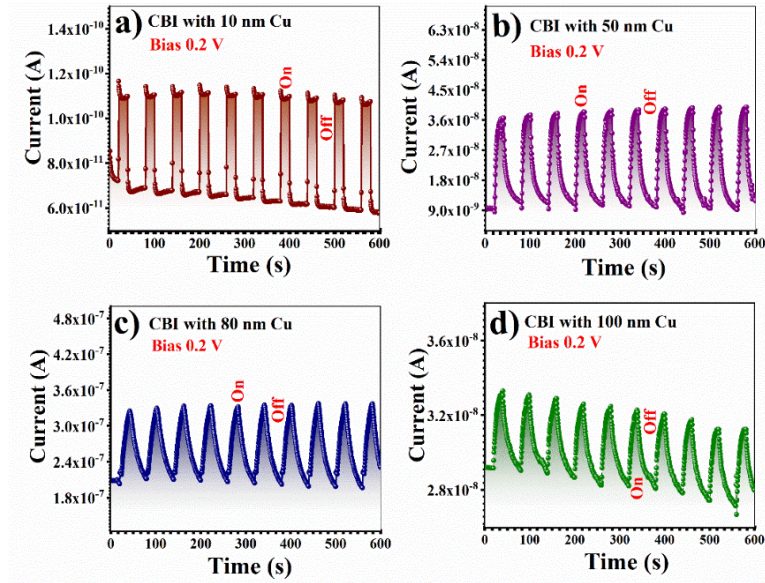
Figure 5.11. Switching behavior of Cu₂BiI₅ photodetectors when illuminated with Tungsten lamp.
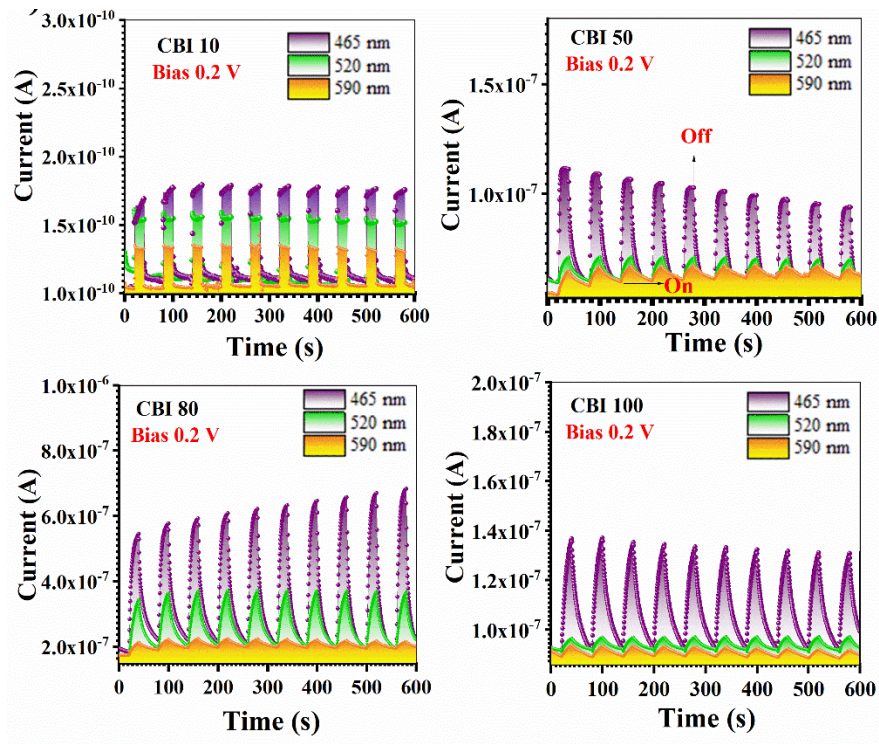
Figure 5.12. Photocurrent response of Cu₂BiI₅ photodetector when illuminated with different wavelength of light from LEDs.

Table 5.2. Sensitivity measurements of Cu_2BiI_5 photodetectors towards different wavelengths of light from LEDs at a bias voltage of 0.2 V.

Sample	Wavelength (nm)	I_{dark} (nA)	I_{light} (nA)	Sensitivity (%)
CBI 10	465	0.112	0.18	60.71
	520	0.11	0.14	27.27
	590	0.11	0.13	18.18
CBI 50	465	59.2	104	75.67
	520	59	79	33.89
	590	54	65	20.37
CBI 80	465	198	500	152.52
	520	185	290	56.75
	590	108	158	46.29
CBI 100	465	88	143	62.5
	520	88	97	10.22
	590	88	92	4.54
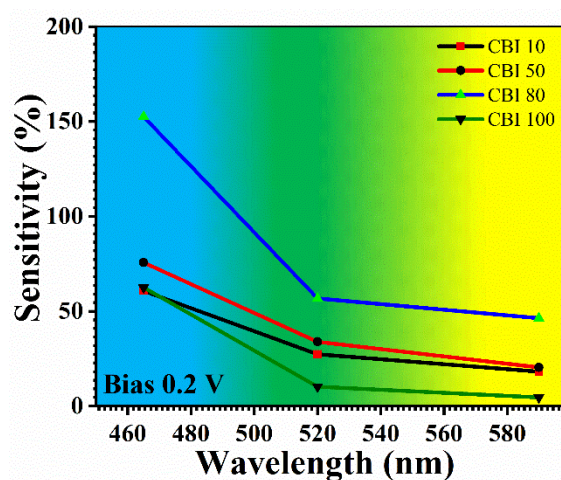
Figure 5.13. Sensitivity of Cu_2BiI_5 photodetector as a function of wavelength of light.

5.2.6. Stability study

A detailed investigation on the stability of Cu_2BiI_5 perovskites was done. For this, Cu_2BiI_5 perovskite samples were exposed to open atmospheric conditions for 30 days. The XRD patterns of 30 days old CBI thin films are given in Figure 5.14 (a). A comparison between the XRD patterns of fresh and 30 days old CBI 50 films is done Figure 5.14 (b).
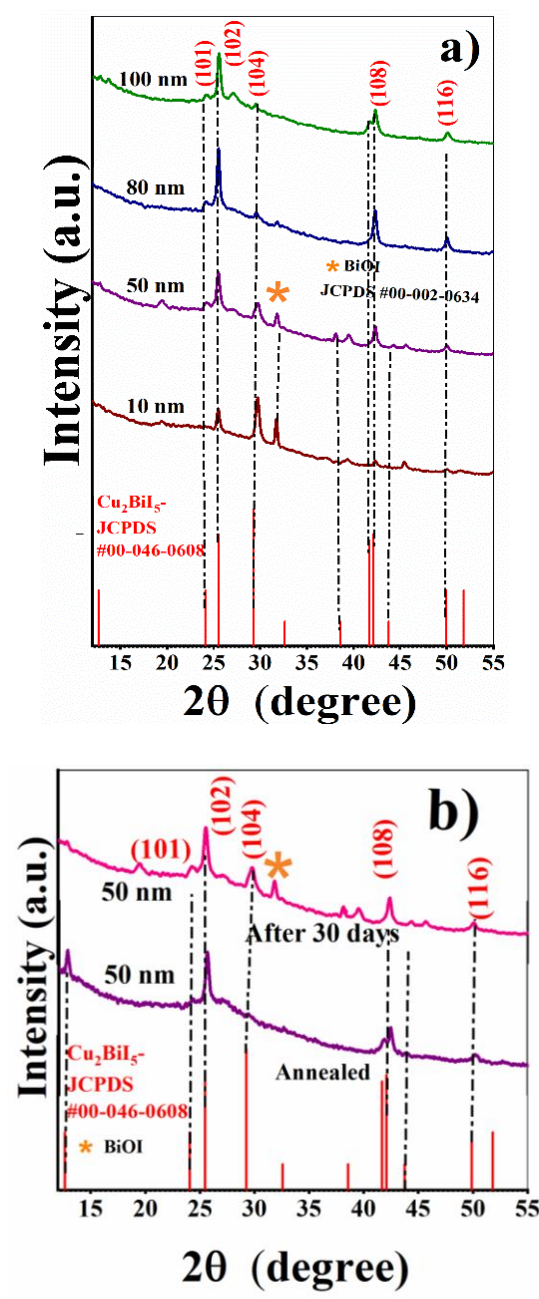
Figure 5.14. XRD patterns of a) annealed films after 30 days of exposure to open atmospheric conditions and b) annealed and 30 days old CBI thin films with 50 nm Cu thickness.

In addition, the diffraction peak at 12.65° disappears for all the 30 days old CBI thin films. The diffraction peak intensity of (101) crystal plane is reduced compared to the freshly annealed samples. Interestingly, the diffraction peak intensities at 25.5° of all the 30 days old samples show a gradual increase. On the other hand, the diffraction peak intensity of the characteristic peak of Cu_2BiI_5 at 29.25° appears with a significant increase in its peak intensity especially for 10 and 50 nm samples. Also, a progressive increment in the intensities of diffraction peaks at 42.1° and 49.9° is observed. After 30 days of exposure to ambient atmospheric conditions, the diffraction intensities of most of the Cu_2BiI_5 peak show a gradual increase. The presence of BiOI in 10 and 50 nm cases cannot be neglected, and it might be due to the sample's exposure to atmospheric air and a lesser amount of Cu atoms (copper deficient Cu_2BiI_5). Thus, the exposure period has a pronounced effect on the crystallinity and nucleation growth for the Cu_2BiI_5 perovskites. More studies are necessary to understand the structural-stability properties of Cu_2BiI_5 perovskites for its further development.

Raman spectra were collected for 30 days old samples to analyze any phase structure changes after exposure to ambient atmospheric conditions (shown in Figure 5.15). Compared to the freshly prepared samples, 30 days old samples of Cu thicknesses 10, 50, and 80 nm showed new Raman lines at 57, 68 and 94 cm^{-1}. These peaks might be attributed to the new peaks of 30-days old Cu_2BiI_5 perovskite, which we observed in the XRD patterns (Figure 5.14 (a)). The most intense peak detected for fresh samples (at 112 cm^{-1}) is observed only for 100 nm Cu thickened sample. Raman peak at 102 cm^{-1} is detected for 10 and 50 nm samples only and is attributed to the BiOI phase[231], matching our XRD results well. The peak intensity corresponding to BiOI phase completely vanished for 80 and 100 nm samples. These results are in good accordance with our XRD results.
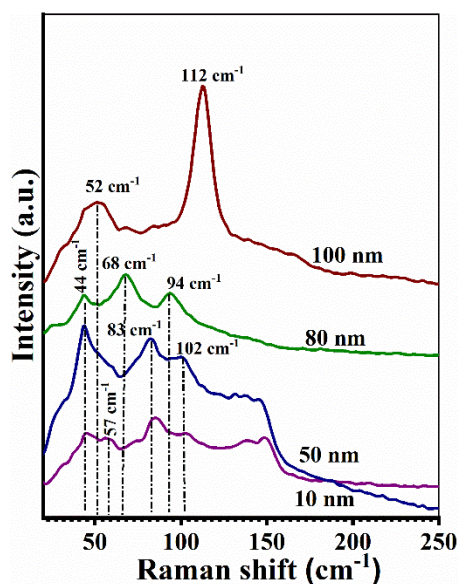
Figure 5.15. Raman spectra of 30 days old CBI perovskite thin films.

To investigate the morphological stability and the effect of storage life on the surface morphology of Cu_2BiI_5 perovskite thin films, we captured FESEM images of 30 days old samples (samples exposed to ambient atmospheric conditions). Their FESEM images (given in Figure 5.16) were compared with that of the freshly annealed samples. Interestingly even after exposure, all the CBI thin films maintained dense and compact surface morphologies with fewer pinholes. This result encourages us to hope that Cu_2BiI_5 perovskite can be a potential candidate for Pb-replacement for future optoelectronic applications.
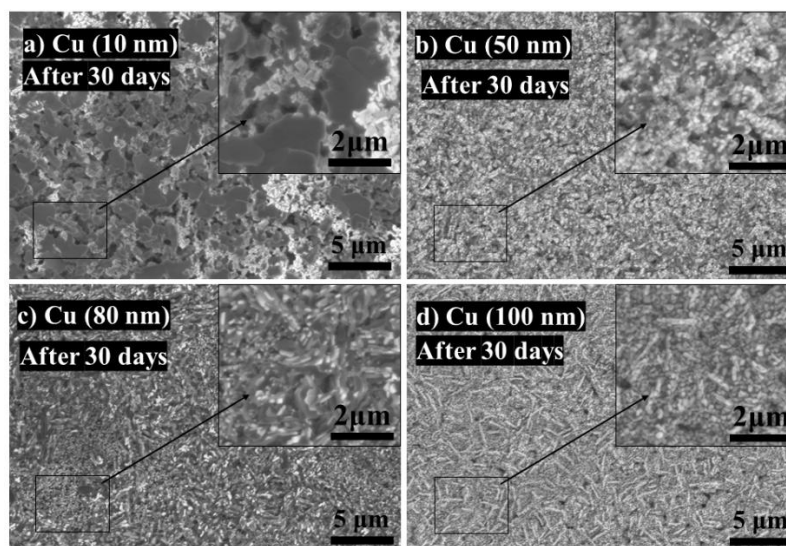
Figure 5.16. FESEM micrographs of 30 days old Cu_2BiI_5 perovskite thin films formed with different Cu thicknesses a) 10 nm, b) 50 nm, c) 80 nm, and d) 100 nm.

The optical absorption spectra of the 30 days exposed samples were collected to check the stability and are given in Figure 5.17. We did not observe significant visual changes on the surface of the samples. Shiny surfaces of CBI 10 and 50 nm films were a little bit powdery, while CBI 80 and 100 nm films were smooth and shiny to the naked eye. Thus, copper content also plays a vital role in maintaining the stability of Cu_2BiI_5 perovskite thin films. From the optical absorption spectra of 30 days old samples, we observed a relatively small shift towards lower wavelengths in the absorbance curve for each case compared to freshly annealed samples. Our optical properties of 30 days old CBI thin films are in a good correlation with structural and morphological results. The vanishing of certain peaks in XRD results and BiOI impurity phase formation might be the reason for this shift. Even after exposure to open atmospheric conditions, CBI thin films are stable since they can absorb light in the visible-NIR zone.
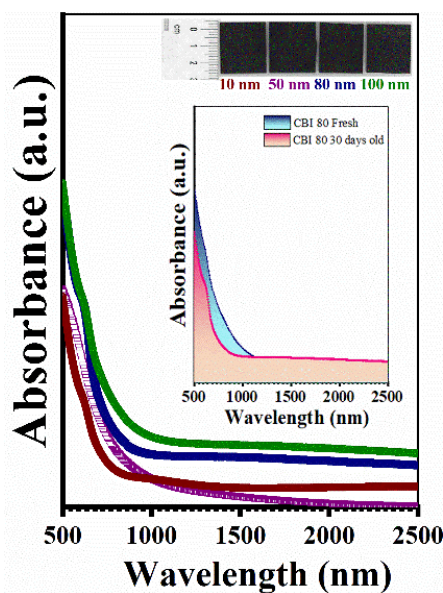
Figure 5.17. UV-Vis absorption spectra of 30 days old CBI films with different copper thicknesses: 10, 50, 80, and 100 nm after exposure to ambient atmospheric conditions.

Additionally, the photocurrent response of 30 days old samples was examined. As evident from Figure 5.18 that 30 days old CBI samples are photoconductive and show stable and reproducible photocurrent. This stable, rapid photocurrent response dynamics

during the switching process and high reproducibility features of newly presenting Cu_2BiI_5 photodetector indicate their suitability for future optoelectronics applications.
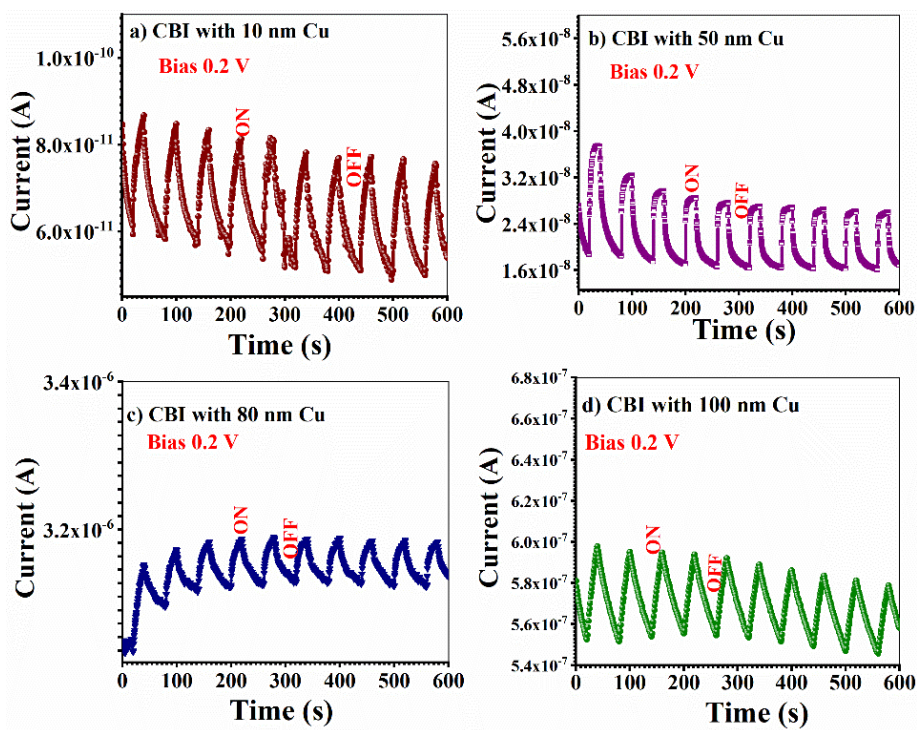
Figure 5.18. Switching behavior of 30 days old Cu_2BiI_5 photodetectors when illuminated with Tungsten lamp.

Chapter 6
Summary and outlook

This chapter presents a summary of the results of this thesis. These are from the synthesis and characterization of binary iodides and newly emerging lead-free ternary perovskites and their optoelectronic applications presented in chapters 3 to 5.

In summary,

✓ Phase pure rhombohedral BiI_3 thin films were fabricated via spin coating method. 1 M concentration was used for this purpose and a film of 450 nm thickness with a direct bandgap of 1.67 eV was obtained. BiI_3-based photodetector was developed and its wavelength dependency on the photocurrent was investigated. The device performance was good in the visible zone with high sensitivity and responsivity. We found that the power density of incident light influences the photocurrent response of our device.

✓ Phase pure SbI_3 thin films were fabricated via low-temperature iodization of Sb_2S_3 thin films for the first ever time. Their structure, morphology, elemental composition, optical and electrical properties were highly influenced by the film thickness of Sb_2S_3 and iodization time. We found that 2 h deposition of Sb_2S_3 and 120 s of iodization were the optimum experimental conditions for SbI_3 thin films with better optoelectronic properties. Their direct bandgap values varied from 2.45 to 2.05 eV with iodization times. Compact and surface morphologies with fewer-voids and uniformity of films were our other encouragement factors to study their optoelectronic properties. Thus, the material was successfully explored for the photodetector application. We propose this material as a promising candidate for future optoelectronic applications.

✓ Structure, morphology, and optical properties of CuI and AgI thin films were investigated as a function of their respective metal film (Cu/Ag) thickness. The

crystallinity of films improved with an increase in the thickness of precursor material (Cu and Ag) and all of them showed high transparency in the visible region. The two-step fabrication method of CuI and AgI resulted in high-quality, uniform thin films and could be useful for future optoelectronic and photovoltaic applications.

✓ Ag_2BiI_5 perovskite thin films were prepared using AgI and BiI_3 powders via spin coating method. Their structure, morphology, composition, optical and electrical properties were investigated for different BiI_3 concentrations while AgI concentration was kept constant. The precursor concentration affected the overall properties of the perovskite. We found that the 1:1 molar concentration of AgI and BiI_3 is the optimum synthesis condition for the formation of Ag_2BiI_5 phase with better structure, morphology and optoelectronic properties. As different characterization techniques confirmed our findings, Ag_2BiI_5 photodetector was developed. The appreciable direct bandgap value of the synthesized material (1.71 eV) showed a device with good reproducibility.

✓ Last but not least, we introduced a bismuth iodide-based new perovskite material: copper bismuth iodide. We incorporated metallic copper into the spin coated BiI_3 thin film utilizing the advantage of a thermal evaporator. For the first time, we produced a new phase for the Cu-Bi-I system: Cu_2BiI_5. A detailed investigation of the influence of Cu thickness on the properties of Cu_2BiI_5 perovskite thin films was done. The actual mechanism for the perovskite formation still needs more detailed investigation. A phase pure Cu_2BiI_5 perovskites formation was favored mostly by 80 nm Cu thickness and an annealing temperature of 100 °C (annealing time: 30 min). A noticeable improvement in the surface morphology for the perovskite thin film was attained as we increased Cu thickness. Direct bandgap values ranging from 1.74-1.53 eV was obtained. These band gap values are favorable for the absorption of entire visible light. The structure, morphology, and optoelectronic properties were tunable by changing the precursor film thickness. A photodetector device with good reproducibility and stability is highly motivating for its future development for optoelectronic applications. We did a detailed stability study for Cu_2BiI_5 thin films and surprisingly all the 30 days old samples showed good surface morphologies with absorption in the Vis-NIR region.

In general, this thesis work be an encouragement for developing lead-free perovskite materials for optoelectronic applications. The present study gives more insight into the synthesis of new perovskite as well as binary compounds. It can be considered as an initiative for lead-free materials for optoelectronic applications. A comprehensive and thorough investigation carried out in the entire research period can inspire others to investigate these materials further, thereby understanding more about a better, pollutant-free ambiance. The results demonstrated in this thesis work can open further possibilities for exploring new materials. The optimization conditions employed here will energize the material research community to develop novel materials for optoelectronic and photovoltaic applications of lead free, stable perovskites.

References

(1)   Hao, F.; Stoumpos, C. C.; Cao, D. H.; Chang, R. P. H.; Kanatzidis, M. G. Lead-Free Solid-State Organic-Inorganic Halide Perovskite Solar Cells. *Nat. Photonics* **2014**, *8* (6), 489–494. https://doi.org/10.1038/nphoton.2014.82.

(2)   Boix, P. P.; Nonomura, K.; Mathews, N.; Mhaisalkar, S. G. Current Progress and Future Perspectives for Organic/Inorganic Perovskite Solar Cells. *Materials Today*. Elsevier B.V. January 1, 2014, pp 16–23. https://doi.org/10.1016/j.mattod.2013.12.002.

(3)   Green, M. A.; Ho-Baillie, A.; Snaith, H. J. The Emergence of Perovskite Solar Cells. *Nature Photonics*. Nature Publishing Group July 27, 2014, pp 506–514. https://doi.org/10.1038/nphoton.2014.134.

(4)   Jin, K. X.; Li, Y. F.; Wang, Z. L.; Peng, H. Y.; Lin, W. N.; Kyaw, A. K. K.; Jin, Y. L.; Jin, K. J.; Sun, X. W.; Soci, C.; et al. Tunable Photovoltaic Effect and Solar Cell Performance of Self-Doped Perovskite SrTiO3. *AIP Adv.* **2012**, *2* (4), 042131. https://doi.org/10.1063/1.4766279.

(5)   Cui, J.; Yuan, H.; Li, J.; Xu, X.; Shen, Y. Recent Progress in Ef Fi Cient Hybrid Lead Halide Perovskite Solar Cells. *Sci Technol Adv Mater* **2015**, *16*, 036004–036017. https://doi.org/10.1088/1468-6996/16/3/036004.

(6)   Shi, Z.; Guo, J.; Chen, Y.; Li, Q.; Pan, Y.; Zhang, H.; Xia, Y. Lead-Free Organic – Inorganic Hybrid Perovskites for Photovoltaic Applications : Recent Advances and Perspectives. **2017**. https://doi.org/10.1002/adma.201605005.

(7)   Yang, S.; Fu, W.; Zhang, Z.; Chen, H.; Li, C. E Ffi Ciency , Stability and Lead-Free Perovskite. *J Mater Chem A* **2017**, *5*, 11462–11482. https://doi.org/10.1039/c7ta00366h.

(8)   Boudour, S.; Bouchama, I.; Bouarissa, N.; Hadjab, M. A Study of CdTe Solar

Cells Using Ga-Doped MgxZn1-XO Buffer/TCO Layers: Simulation and Performance Analysis. *J. Sci. Adv. Mater. Devices* **2019**, *4* (1), 111–115. https://doi.org/10.1016/J.JSAMD.2018.12.001.

(9)   Ratner, M. The Physics of Solar Cells ; Third Generation Photovoltaics: Advanced Solar Energy Conversion The Physics of Solar Cells. *Phys. Today* **2004**, *57* (12), 71–72. https://doi.org/10.1063/1.1878345.

(10)   Kojima, A.; Teshima, K.; Shirai, Y.; Miyasaka, T. Organometal Halide Perovskites as Visible-Light Sensitizers for Photovoltaic. *J. Am. Chem. Soc.* **2009**, *131*, 6050–6051. https://doi.org/10.1021/ja809598r.

(11)   NREL. Best Research-Cell Efficiency Chart https://www.nrel.gov/pv/assets/pdfs/best-research-cell-efficiencies.20191106.pdf (accessed Jan 4, 2020).

(12)   Yao, Z.; Wang, W.; Shen, H.; Zhang, Y.; Luo, Q.; Yin, X.; Dai, X.; Li, J.; Lin, H. CH 3 NH 3 PbI 3 Grain Growth and Interfacial Properties in Meso-Structured Perovskite Solar Cells Fabricated by Two-Step Deposition. *Sci. Technol. Adv. Mater.* **2017**, *18* (1), 1–10. https://doi.org/10.1080/14686996.2017.1298974.

(13)   Han, J.; Yin, X.; Nan, H.; Zhou, Y.; Yao, Z.; Li, J.; Oron, D.; Lin, H. Enhancing the Performance of Perovskite Solar Cells by Hybridizing SnS Quantum Dots with CH 3 NH 3 PbI 3. *Small.* **2017**, *13*, 1–8. https://doi.org/10.1002/smll.201700953.

(14)   Yin, X.; Yao, Z.; Luo, Q.; Dai, X.; Zhou, Y.; Zhang, Y.; Zhou, Y.; Luo, S.; Li, J.; Wang, N.; et al. High E Ffi Ciency Inverted Planar Perovskite Solar Cells with Solution- Processed NiO. *ACS appl mater interfaces* **2017**, *9*, 2439–2448. https://doi.org/10.1021/acsami.6b13372.

(15)   Kumar, A.; Singh, A.; Ojha, A. K. A New Approach to Predict the Formation of 3D Hybrid Organic-Inorganic Perovskites. *Int. J. Quantum Chem.* **2019**, *119* (22). https://doi.org/10.1002/qua.26012.

(16)   Li, C.; Soh, K. C. K.; Wu, P. Formability of ABO3 Perovskites. *J. Alloys Compd.*

2004, *372* (1–2), 40–48. https://doi.org/10.1016/j.jallcom.2003.10.017.

(17) Amat, A.; Mosconi, E.; Ronca, E.; Quarti, C.; Umari, P.; Nazeeruddin, M. K.; Grätzel, M.; De Angelis, F. Cation-Induced Band-Gap Tuning in Organohalide Perovskites: Interplay of Spin-Orbit Coupling and Octahedra Tilting. *Nano Lett.* **2014**, *14* (6), 3608–3616. https://doi.org/10.1021/nl5012992.

(18) Kieslich, G.; Sun, S.; Cheetham, A. K. Solid-State Principles Applied to Organic–Inorganic Perovskites: New Tricks for an Old Dog. *Chem. Sci.* **2014**, *5* (12), 4712–4715. https://doi.org/10.1039/c4sc02211d.

(19) Zhao, Y.; Zhu, K. Organic-Inorganic Hybrid Lead Halide Perovskites for Optoelectronic and Electronic Applications. *Chemical Society Reviews*. Royal Society of Chemistry February 7, 2016, pp 655–689. https://doi.org/10.1039/c4cs00458b.

(20) Yang, J.; Siempelkamp, B. D.; Mosconi, E.; De Angelis, F.; Kelly, T. L. Origin of the Thermal Instability in CH3NH3PbI3 Thin Films Deposited on ZnO. *Chem. Mater.* **2015**, *27* (12), 4229–4236. https://doi.org/10.1021/acs.chemmater.5b01598.

(21) Conings, B.; Drijkoningen, J.; Gauquelin, N.; Babayigit, A.; D'Haen, J.; D'Olieslaeger, L.; Ethirajan, A.; Verbeeck, J.; Manca, J.; Mosconi, E.; et al. Intrinsic Thermal Instability of Methylammonium Lead Trihalide Perovskite. *Adv. Energy Mater.* **2015**, *5* (15), 1500477. https://doi.org/10.1002/aenm.201500477.

(22) Ahmad, S.; Kanaujia, P. K.; Niu, W.; Baumberg, J. J.; Vijaya Prakash, G. In Situ Intercalation Dynamics in Inorganic-Organic Layered Perovskite Thin Films. *ACS Appl. Mater. Interfaces* **2014**, *6* (13), 10238–10247. https://doi.org/10.1021/am501568j.

(23) Juarez-Perez, E. J.; Ono, L. K.; Maeda, M.; Jiang, Y.; Hawash, Z.; Qi, Y. Photodecomposition and Thermal Decomposition in Methylammonium Halide Lead Perovskites and Inferred Design Principles to Increase Photovoltaic Device Stability. *J. Mater. Chem. A* **2018**, *6* (20), 9604–9612.

https://doi.org/10.1039/c8ta03501f.

(24)   Saliba, M.; Matsui, T.; Seo, J. Y.; Domanski, K.; Correa-Baena, J. P.;
        Nazeeruddin, M. K.; Zakeeruddin, S. M.; Tress, W.; Abate, A.; Hagfeldt, A.; et
        al. Cesium-Containing Triple Cation Perovskite Solar Cells: Improved Stability,
        Reproducibility and High Efficiency. *Energy Environ. Sci.* **2016**, *9* (6), 1989–
        1997. https://doi.org/10.1039/c5ee03874j.

(25)   Wang, Z.; Lin, Q.; Chmiel, F. P.; Sakai, N.; Herz, L. M.; Snaith, H. J. Efficient
        Ambient-Air-Stable Solar Cells with 2D-3D Heterostructured Butylammonium-
        Caesium-Formamidinium Lead Halide Perovskites. *Nat. Energy* **2017**, *2* (9), 1–
        10. https://doi.org/10.1038/nenergy.2017.135.

(26)   Zheng, K.; Chen, Y.; Sun, Y.; Chen, J.; Chábera, P.; Schaller, R.; Al-Marri, M. J.;
        Canton, S. E.; Liang, Z.; Pullerits, T. Inter-Phase Charge and Energy Transfer in
        Ruddlesden-Popper 2D Perovskites: Critical Role of the Spacing Cations. *J.
        Mater. Chem. A* **2018**, *6* (15), 6244–6250. https://doi.org/10.1039/c8ta01518j.

(27)   Grancini, G.; Roldán-Carmona, C.; Zimmermann, I.; Mosconi, E.; Lee, X.;
        Martineau, D.; Narbey, S.; Oswald, F.; De Angelis, F.; Graetzel, M.; et al. One-
        Year Stable Perovskite Solar Cells by 2D/3D Interface Engineering. *Nat.
        Commun.* **2017**, *8* (1), 1–8. https://doi.org/10.1038/ncomms15684.

(28)   Chaudhary, B.; Kulkarni, A.; Jena, A. K.; Ikegami, M.; Udagawa, Y.; Kunugita,
        H.; Ema, K.; Miyasaka, T. Poly(4-Vinylpyridine)-Based Interfacial Passivation to
        Enhance Voltage and Moisture Stability of Lead Halide Perovskite Solar Cells.
        ChemSusChem **2017**, *10* (11), 2473–2479.
        https://doi.org/10.1002/cssc.201700271.

(29)   Weerasinghe, H. C.; Dkhissi, Y.; Scully, A. D.; Caruso, R. A.; Cheng, Y. B.
        Encapsulation for Improving the Lifetime of Flexible Perovskite Solar Cells.
        Nano Energy **2015**, *18*, 118–125. https://doi.org/10.1016/j.nanoen.2015.10.006.

(30)   Wang, R.; Mujahid, M.; Duan, Y.; Wang, Z. K.; Xue, J.; Yang, Y. A Review of
        Perovskites Solar Cell Stability. *Advanced Functional Materials*. Wiley-VCH
        Verlag November 1, 2019, p 1808843. https://doi.org/10.1002/adfm.201808843.

(31)   Babayigit, A.; Ethirajan, A.; Muller, M.; Conings, B. Toxicity of Organometal
        Halide Perovskite Solar Cells. *Nature Materials*. Nature Publishing Group
        February 24, 2016, pp 247–251. https://doi.org/10.1038/nmat4572.

(32)   Aristidou, N.; Sanchez-Molina, I.; Chotchuangchutchaval, T.; Brown, M.;
        Martinez, L.; Rath, T.; Haque, S. A. The Role of Oxygen in the Degradation of
        Methylammonium Lead Trihalide Perovskite Photoactive Layers. *Angew. Chemie
        Int. Ed.* **2015**, *54* (28), 8208–8212. https://doi.org/10.1002/anie.201503153.

(33)   Zhang, Q.; Ting, H.; Wei, S.; Huang, D.; Wu, C.; Sun, W.; Qu, B.; Wang, S.;
        Chen, Z.; Xiao, L. Recent Progress in Lead-Free Perovskite (-like) Solar Cells.
        Mater. Today Energy **2018**, *8*, 157–165.
        https://doi.org/10.1016/J.MTENER.2018.03.001.

(34)   Fu, H. Review of Lead-Free Halide Perovskites as Light-Absorbers for
        Photovoltaic Applications: From Materials to Solar Cells. *Sol. Energy Mater. Sol.
        Cells* **2019**, *193*, 107–132. https://doi.org/10.1016/J.SOLMAT.2018.12.038.

(35)   Hoefler, S. F.; Trimmel, G.; Rath, T. Progress on Lead-Free Metal Halide
        Perovskites for Photovoltaic Applications: A Review. *Monatshefte fur Chemie*.
        Springer-Verlag Wien May 1, 2017, pp 795–826. https://doi.org/10.1007/s00706-
        017-1933-9.

(36)   Noel, N. K.; Stranks, S. D.; Abate, A.; Wehrenfennig, C.; Guarnera, S.;
        Haghighirad, A. A.; Sadhanala, A.; Eperon, G. E.; Pathak, S. K.; Johnston, M. B.;
        et al. Lead-Free Organic-Inorganic Tin Halide Perovskites for Photovoltaic
        Applications. *Energy Environ. Sci.* **2014**, *7* (9), 3061–3068.
        https://doi.org/10.1039/c4ee01076k.

(37)   Krishnamoorthy, T.; Ding, H.; Yan, C.; Leong, W. L.; Baikie, T.; Zhang, Z.;
        Sherburne, M.; Li, S.; Asta, M.; Mathews, N.; et al. Lead-Free Germanium Iodide
        Perovskite Materials for Photovoltaic Applications. *J. Mater. Chem. A* **2015**, *3*
        (47), 23829–23832. https://doi.org/10.1039/c5ta05741h.

(38)   Grimm, J.; Wenger, O. S.; Krämer, K. W.; Güdel, H. U. 4f-4f and 4f-5d Excited
        States and Luminescence Properties of Tm2 +- Doped CaF2, CaCl2, SrCl2 and

BaCl2. *J. Lumin.* **2007**, *126* (2), 590–596.
https://doi.org/10.1016/j.jlumin.2006.10.007.

(39)   Grimm, J.; Beurer, E.; Gerner, P.; Güdel, H. U. Upconversion between 4f-5d
        Excited States in Tm2+-Doped CsCaCl3, CsCaBr3, and CsCaI3. *Chem. - A Eur.
        J.* **2007**, *13* (4), 1152–1157. https://doi.org/10.1002/chem.200600418.

(40)   Hu, J.; Yan, L.; You, W. Two-Dimensional Organic–Inorganic Hybrid
        Perovskites: A New Platform for Optoelectronic Applications. *Adv. Mater.* **2018**,
        30 (48). https://doi.org/10.1002/adma.201802041.

(41)   Suta, M.; Urland, W.; Daul, C.; Wickleder, C. Photoluminescence Properties of
        Yb2+ Ions Doped in the Perovskites CsCaX3 and CsSrX3 (X = Cl, Br, and I)-a
        Comparative Study. *Phys. Chem. Chem. Phys.* **2016**, *18* (19), 13196–13208.
        https://doi.org/10.1039/c6cp00085a.

(42)   Cui, X. P.; Jiang, K. J.; Huang, J. H.; Zhang, Q. Q.; Su, M. J.; Yang, L. M.; Song,
        Y. L.; Zhou, X. Q. Cupric Bromide Hybrid Perovskite Heterojunction Solar Cells.
        Synth. Met. **2015**, *209*, 247–250. https://doi.org/10.1016/j.synthmet.2015.07.013.

(43)   Filip, M. R.; Giustino, F. Computational Screening of Homovalent Lead
        Substitution in Organic-Inorganic Halide Perovskites. *J. Phys. Chem. C* **2016**, *120*
        (1), 166–173. https://doi.org/10.1021/acs.jpcc.5b11845.

(44)   Arend, H.; Huber, W.; K., G. Layer Perovskites of the (CnH2n+1NH3)2MX4 and
        NH3(CH2)MNH3MX4 Families with M = Cd, Cu, Fe, Mn OR Pd and X = Cl OR
        Br: Importance, Solubilities and Simple Growth Techniques. *J. Cryst. Growth*
        1978, *43* (2), 213–223. https://doi.org/10.1016/0022-0248(78)90170-7.

(45)   Raw, A. D.; Ibers, J. A.; Poeppelmeier, K. R. Syntheses and Structure of
        Hydrothermally Prepared CsNiX 3 (X=Cl, Br, I). *J. Solid State Chem.* **2012**, *192*,
        34–37. https://doi.org/10.1016/j.jssc.2012.03.037.

(46)   Choudhary, K. Identification of Potential Replacement Materials for Lead in
        CH3NH3PbI3 Using First Principle Calculations. *Appl. Surf. Sci.* **2015**, *334*, 40–
        44.

(47)   Matsushita, N.; Kitagawa, H.; Kojima, N. A Three-Dimensional Iodo-Bridged
        Mixed-Valence Gold(I,III) Compound, Cs2AuIAuIIII6. *Acta Crystallogr. Sect. C
        Cryst. Struct. Commun.* **1997**, *53* (6), 663–666.
        https://doi.org/10.1107/S0108270197000279.

(48)   Retuerto, M.; Emge, T.; Hadermann, J.; Stephens, P. W.; Li, M. R.; Yin, Z. P.;
        Croft, M.; Ignatov, A.; Zhang, S. J.; Yuan, Z.; et al. Synthesis and Properties of
        Charge-Ordered Thallium Halide Perovskites, CsTl+0.5Tl3+0.5X3 (X = F or Cl):
        Theoretical Precursors for Superconductivity? *Chem. Mater.* **2013**, *25* (20), 4071–
        4079. https://doi.org/10.1021/cm402423x.

(49)   Park, B.-W.; Philippe, B.; Zhang, X.; Rensmo, H.; Boschloo, G.; Johansson, E.
        M. J. Bismuth Based Hybrid Perovskites A 3 Bi 2 I 9 (A: Methylammonium or
        Cesium) for Solar Cell Application. *Adv. Mater.* **2015**, *27* (43), 6806–6813.
        https://doi.org/10.1002/adma.201501978.

(50)   Saparov, B.; Hong, F.; Sun, J. P.; Duan, H. S.; Meng, W.; Cameron, S.; Hill, I. G.;
        Yan, Y.; Mitzi, D. B. Thin-Film Preparation and Characterization of Cs3Sb2I9: A
        Lead-Free Layered Perovskite Semiconductor. *Chem. Mater.* **2015**, *27* (16),
        5622–5632. https://doi.org/10.1021/acs.chemmater.5b01989.

(51)   Lehner, A. J.; Fabini, D. H.; Evans, H. A.; Hébert, C. A.; Smock, S. R.; Hu, J.;
        Wang, H.; Zwanziger, J. W.; Chabinyc, M. L.; Seshadri, R. Crystal and Electronic
        Structures of Complex Bismuth Iodides A3Bi2I9 (A = K, Rb, Cs) Related to
        Perovskite: Aiding the Rational Design of Photovoltaics. *Chem. Mater.* **2015**, *27*
        (20), 7137–7148. https://doi.org/10.1021/acs.chemmater.5b03147.

(52)   Sun, Y. Y.; Shi, J.; Lian, J.; Gao, W.; Agiorgousis, M. L.; Zhang, P.; Zhang, S.
        Discovering Lead-Free Perovskite Solar Materials with a Split-Anion Approach.
        Nanoscale **2016**, *8* (12), 6284–6289. https://doi.org/10.1039/c5nr04310g.

(53)   Hong, F.; Saparov, B.; Meng, W.; Xiao, Z.; Mitzi, D. B.; Yan, Y. Viability of
        Lead-Free Perovskites with Mixed Chalcogen and Halogen Anions for
        Photovoltaic Applications. *J. Phys. Chem. C* **2016**, *120* (12), 6435–6441.
        https://doi.org/10.1021/acs.jpcc.6b00920.

122

(54)   Nitta, T.; Nagase. Formation, Microstructure, and Properties of Barium Zirconium Sulfide Ceramics. *J. Am. Ceram. Soc.* **1970**, *53* (11), 601–604. https://doi.org/10.1111/j.1151-2916.1970.tb15981.x.

(55)   Lelieveld, R.; IJdo, D. J. W. Sulphides with the GdFeO 3 Structure . *Acta Crystallogr. Sect. B Struct. Crystallogr. Cryst. Chem.* **1980**, *36* (10), 2223–2226. https://doi.org/10.1107/s056774088000845x.

(56)   Yang, S. Y.; Martin, L. W.; Byrnes, S. J.; Conry, T. E.; Basu, S. R.; Paran, D.; Reichertz, L.; Ihlefeld, J.; Adamo, C.; Melville, A.; et al. Photovoltaic Effects in BiFeO3. *Appl. Phys. Lett.* **2009**, *95* (6), 062909. https://doi.org/10.1063/1.3204695.

(57)   Jung, M. C.; Raga, S. R.; Qi, Y. Properties and Solar Cell Applications of Pb-Free Perovskite Films Formed by Vapor Deposition. *RSC Adv.* **2016**, *6* (4), 2819–2825. https://doi.org/10.1039/c5ra21291j.

(58)   Chung, I.; Lee, B.; He, J.; Chang, R. P. H.; Kanatzidis, M. G. All-Solid-State Dye-Sensitized Solar Cells with High Efficiency. *Nature* **2012**, *485* (7399), 486–489. https://doi.org/10.1038/nature11067.

(59)   Wang, N.; Zhou, Y.; Ju, M.-G.; Garces, H. F.; Ding, T.; Pang, S.; Zeng, X. C.; Padture, N. P.; Sun, X. W. Heterojunction-Depleted Lead-Free Perovskite Solar Cells with Coarse-Grained B-γ-CsSnI 3 Thin Films. *Adv. Energy Mater.* **2016**, *6* (24), 1601130. https://doi.org/10.1002/aenm.201601130.

(60)   Kumar, M. H.; Dharani, S.; Leong, W. L.; Boix, P. P.; Prabhakar, R. R.; Baikie, T.; Shi, C.; Ding, H.; Ramesh, R.; Asta, M.; et al. Lead-Free Halide Perovskite Solar Cells with High Photocurrents Realized Through Vacancy Modulation. *Adv. Mater.* **2014**, *26* (41), 7122–7127. https://doi.org/10.1002/adma.201401991.

(61)   Peedikakkandy, L.; Bhargava, P. Composition Dependent Optical, Structural and Photoluminescence Characteristics of Cesium Tin Halide Perovskites. *RSC Adv.* **2016**, *6* (24), 19857–19860. https://doi.org/10.1039/c5ra22317b.

(62)   Stoumpos, C. C.; Malliakas, C. D.; Kanatzidis, M. G. Semiconducting Tin and

Lead Iodide Perovskites with Organic Cations: Phase Transitions, High Mobilities, and near-Infrared Photoluminescent Properties. *Inorg. Chem.* **2013**, *52* (15), 9019–9038. https://doi.org/10.1021/ic401215x.

(63)   Koh, T. M.; Krishnamoorthy, T.; Yantara, N.; Shi, C.; Leong, W. L.; Boix, P. P.; Grimsdale, A. C.; Mhaisalkar, S. G.; Mathews, N. Formamidinium Tin-Based Perovskite with Low Eg for Photovoltaic Applications. *J. Mater. Chem. A* **2015**, *3* (29), 14996–15000. https://doi.org/10.1039/c5ta00190k.

(64)   Lee, S. J.; Shin, S. S.; Kim, Y. C.; Kim, D.; Ahn, T. K.; Noh, J. H.; Seo, J.; Seok, S. Il. Fabrication of Efficient Formamidinium Tin Iodide Perovskite Solar Cells through SnF2-Pyrazine Complex. *J. Am. Chem. Soc.* **2016**, *138* (12), 3974–3977. https://doi.org/10.1021/jacs.6b00142.

(65)   Liao, W.; Zhao, Y. Lead-Free Inverted Planar Formamidinium Tin Triiodide Perovskite Solar Cells Achieving Power Conversion Efficiencies up to 6.22%. *Adv. Mater.* **2016**, *28* (42), 9333–9340. https://doi.org/10.1002/adma.201602992.

(66)   Stoumpos, J. I.; Kanatzidis, M. G. Hybrid Germanium Iodide Perovskite Semiconductors: Active Lone Pairs, Structural Distortions, Direct and Indirect Energy Gaps, and Strong Nonlinear Optical Properties. *J. Am. Chem. Soc.* **2015**, *137* (21), 6804–6819. https://doi.org/10.1021/jacs.5b01025.

(67)   Tang, L. C.; Chang, Y. C.; Huang, J. Y.; Lee, M. H.; Chang, C. S. First Principles Calculations of Linear and Second-Order Optical Responses in Rhombohedrally Distorted Perovskite Ternary Halides, CsGeX3 (X = Cl, Br, and I). *Jpn. J. Appl. Phys.* **2009**, *48* (11), 112402. https://doi.org/10.1143/JJAP.48.112402.

(68)   Huang, L. Y.; Lambrecht, W. R. L. Electronic Band Structure Trends of Perovskite Halides: Beyond Pb and Sn to Ge and Si. *Phys. Rev. B* **2016**, *93* (19), 195211. https://doi.org/10.1103/PhysRevB.93.195211.

(69)   Lu, X.; Zhao, Z.; Li, K.; Han, Z.; Wei, S.; Guo, C.; Zhou, S.; Wu, Z.; Guo, W.; Wu, C. M. L. First-Principles Insight into the Photoelectronic Properties of Ge-Based Perovskites. *RSC Adv.* **2016**, *6* (90), 86976–86981. https://doi.org/10.1039/c6ra18534g.

(70) Qian, J.; Xu, B.; Tian, W. A Comprehensive Theoretical Study of Halide
      Perovskites ABX3. *Org. Electron.* **2016**, *37*, 61–73.
      https://doi.org/10.1016/j.orgel.2016.05.046.

(71) Pazoki, M.; Jacobsson, T. J.; Hagfeldt, A.; Boschloo, G.; Edvinsson, T. Effect of
      Metal Cation Replacement on the Electronic Structure of Metalorganic Halide
      Perovskites: Replacement of Lead with Alkaline-Earth Metals. *Phys. Rev. B* **2016**,
      93 (14), 144105. https://doi.org/10.1103/PhysRevB.93.144105.

(72) Uribe, J. I.; Ramirez, D.; Osorio-Guillén, J. M.; Osorio, J.; Jaramillo, F.
      CH3NH3CaI3 Perovskite: Synthesis, Characterization, and First-Principles
      Studies. *J. Phys. Chem. C* **2016**, *120* (30), 16393–16398.
      https://doi.org/10.1021/acs.jpcc.6b04207.

(73) Cortecchia, D.; Dewi, H. A.; Yin, J.; Bruno, A.; Chen, S.; Baikie, T.; Boix, P. P.;
      Grätzel, M.; Mhaisalkar, S.; Soci, C.; et al. Lead-Free MA2CuClxBr4-x Hybrid
      Perovskites. *Inorg. Chem.* **2016**, *55* (3), 1044–1052.
      https://doi.org/10.1021/acs.inorgchem.5b01896.

(74) Zhang, B.; Lei, Y.; Qi, R.; Yu, H.; Yang, X.; Cai, T.; Zheng, Z. An In-Situ Room
      Temperature Route to CuBiI 4 Based Bulk-Heterojunction Perovskite-like Solar
      Cells. *Sci. China Mater.* **2019**, *62* (4), 519–526. https://doi.org/10.1007/s40843-
      018-9355-0.

(75) Peresh, E. Y.; Sidei, V. I.; Zubaka, O. V.; Stercho, I. P. K 2(Rb 2,Cs 2,Tl 2)TeBr
      6(I 6) and Rb 3(Cs 3)Sb 2(Bi 2)Br 9(I 9) Perovskite Compounds. *Inorg. Mater.*
      2011, *47* (2), 208–212. https://doi.org/10.1134/S0020168511010109.

(76) McClure, E. T.; Ball, M. R.; Windl, W.; Woodward, P. M. Cs2AgBiX6 (X = Br,
      Cl): New Visible Light Absorbing, Lead-Free Halide Perovskite Semiconductors.
      Chem. Mater. **2016**, *28* (5), 1348–1354.
      https://doi.org/10.1021/acs.chemmater.5b04231.

(77) Kreuzer, M.; Schnelzer, M.; Tschense, A.; Walsh, L.; Grosche, B. Cohort Profile:
      The German Uranium Miners Cohort Study (WISMUT Cohort), 1946-2003. *Int.
      J. Epidemiol.* **2010**, *39* (4), 980–987. https://doi.org/10.1093/ije/dyp216.

(78)   Attique, S.; Ali, N.; Ali, S.; Khatoon, R.; Li, N.; Khesro, A.; Rauf, S.; Yang, S.;
Wu, H. A Potential Checkmate to Lead: Bismuth in Organometal Halide
Perovskites, Structure, Properties, and Applications. *Adv. Sci.* **2020**, *7* (13),
1903143. https://doi.org/10.1002/advs.201903143.

(79)   Brandt, R. E.; Stevanović, V.; Ginley, D. S.; Buonassisi, T. Identifying Defect-
Tolerant Semiconductors with High Minority-Carrier Lifetimes: Beyond Hybrid
Lead Halide Perovskites. *MRS Commun.* **2015**, *5* (2), 265–275.
https://doi.org/10.1557/mrc.2015.26.

(80)   Saparov, B.; Mitzi, D. B. Organic-Inorganic Perovskites: Structural Versatility for
Functional Materials Design. *Chemical Reviews*. American Chemical Society
April 27, 2016, pp 4558–4596. https://doi.org/10.1021/acs.chemrev.5b00715.

(81)   Allen, L. C. Electronegativity Is the Average One-Electron Energy of the
Valence-Shell Electrons in Ground-State Free Atoms. *J. Am. Chem. Soc.* **1989**,
111 (25), 9003–9014. https://doi.org/10.1021/ja00207a003.

(82)   Filip, M. R.; Hillman, S.; Haghighirad, A. A.; Snaith, H. J.; Giustino, F. Band
Gaps of the Lead-Free Halide Double Perovskites Cs2BiAgCl6 and Cs2BiAgBr6
from Theory and Experiment. *J. Phys. Chem. Lett.* **2016**, *7* (13), 2579–2585.
https://doi.org/10.1021/acs.jpclett.6b01041.

(83)   Slavney, A. H.; Hu, T.; Lindenberg, A. M.; Karunadasa, H. I. A Bismuth-Halide
Double Perovskite with Long Carrier Recombination Lifetime for Photovoltaic
Applications. *J. Am. Chem. Soc.* **2016**, *138* (7), 2138–2141.
https://doi.org/10.1021/jacs.5b13294.

(84)   Kamminga, M. E.; Stroppa, A.; Picozzi, S.; Chislov, M.; Zvereva, I. A.; Baas, J.;
Meetsma, A.; Blake, G. R.; Palstra, T. T. M. Polar Nature of (CH3NH3)3Bi2I9
Perovskite-Like Hybrids. *Inorg. Chem.* **2017**, *56* (1), 33–41.
https://doi.org/10.1021/acs.inorgchem.6b01699.

(85)   Pazoki, M.; Johansson, M. B.; Zhu, H.; Broqvist, P.; Edvinsson, T.; Boschloo, G.;
Johansson, E. M. J. Bismuth Iodide Perovskite Materials for Solar Cell
Applications: Electronic Structure, Optical Transitions, and Directional Charge

Transport. *J. Phys. Chem. C* **2016**, *120* (51), 29039–29046.
https://doi.org/10.1021/acs.jpcc.6b11745.

(86)   Podraza, N. J.; Qiu, W.; Hinojosa, B. B.; Motyka, M. A.; Phillpot, S. R.; Baciak,
J. E.; Trolier-mckinstry, S.; Nino, J. C. Band Gap and Structure of Single Crystal
BiI3 : Resolving Discrepancies in Literature. *J. Appl. Phys.* **2015**, *033110* (2013),
033110. https://doi.org/10.1063/1.4813486.

(87)   Kim, Y.; Yang, Z.; Jain, A.; Voznyy, O.; Kim, G.-H.; Liu, M.; Quan, L. N.;
García de Arquer, F. P.; Comin, R.; Fan, J. Z.; et al. Pure Cubic-Phase Hybrid
Iodobismuthates AgBi $_2$ I $_7$ for Thin-Film Photovoltaics. *Angew. Chemie Int. Ed.*
2016, *55* (33), 9586–9590. https://doi.org/10.1002/anie.201603608.

(88)   Fourcroy, P. H.; Carré, D.; Thévet, F.; Rivet, J. Structure Du Tétraiodure de
Cuivre(I) et de Bismuth(III), CuBiI4. *Acta Crystallogr. Sect. C Cryst. Struct.*
Commun. **1991**, *47* (10), 2023–2025.
https://doi.org/10.1107/s0108270191005309.

(89)   Kim, Y.; Yang, Z.; Jain, A.; Voznyy, O.; Kim, G.-H.; Liu, M.; Quan, L. N.;
García de Arquer, F. P.; Comin, R.; Fan, J. Z.; et al. Pure Cubic-Phase Hybrid
Iodobismuthates AgBi 2 I 7 for Thin-Film Photovoltaics. *Angew. Chemie Int. Ed.*
2016, *55* (33), 9586–9590. https://doi.org/10.1002/anie.201603608.

(90)   Zhu, H.; Pan, M.; Johansson, M. B.; Johansson, E. M. J. High Photon-to-Current
Conversion in Solar Cells Based on Light-Absorbing Silver Bismuth Iodide.
ChemSusChem **2017**, *10* (12), 2592–2596.
https://doi.org/10.1002/cssc.201700634.

(91)   Turkevych, I.; Kazaoui, S.; Ito, E.; Urano, T.; Yamada, K.; Tomiyasu, H.;
Yamagishi, H.; Kondo, M.; Aramaki, S. Photovoltaic Rudorffites: Lead-Free
Silver Bismuth Halides Alternative to Hybrid Lead Halide Perovskites.
ChemSusChem **2017**, *10* (19), 3754–3759.
https://doi.org/10.1002/cssc.201700980.

(92)   Pai, N.; Lu, J.; Gengenbach, T. R.; Seeber, A.; Chesman, A. S. R.; Jiang, L.;
Senevirathna, D. C.; Andrews, P. C.; Bach, U.; Cheng, Y.; et al. Silver Bismuth

Sulfoiodide Solar Cells: Tuning Optoelectronic Properties by Sulfide Modification for Enhanced Photovoltaic Performance. *Adv. Energy Mater.* **2018**, *9* (5), 1803396. https://doi.org/10.1002/aenm.201803396.

(93)   Khazaee, M.; Sardashti, K.; Chung, C.-C.; Sun, J.-P.; Zhou, H.; Bergmann, E.; Dunlap-Shohl, W. A.; Han, Q.; Hill, I. G.; Jones, J. L.; et al. Dual-Source Evaporation of Silver Bismuth Iodide Films for Planar Junction Solar Cells. *J. Mater. Chem. A* **2019**, *7* (5), 2095–2105. https://doi.org/10.1039/C8TA08679F.

(94)   Shao, Z.; Le Mercier, T.; Madec, M. B.; Pauporté, T. Exploring AgBixI3x + 1 Semiconductor Thin Films for Lead-Free Perovskite Solar Cells. *Mater. Des.* **2018**, *141*, 81–87. https://doi.org/10.1016/J.MATDES.2017.12.036.

(95)   Hu, Z.; Wang, Z.; Kapil, G.; Ma, T.; Iikubo, S.; Minemoto, T.; Yoshino, K.; Toyoda, T.; Shen, Q.; Hayase, S. Solution-Processed Air-Stable Copper Bismuth Iodide for Photovoltaics. *ChemSusChem* **2018**, *11* (17), 2930–2935. https://doi.org/10.1002/cssc.201800815.

(96)   Konstantatos, G.; Sargent, E. H. Nanostructured Materials for Photon Detection. *Nature Nanotechnology*. Nature Publishing Group May 16, 2010, pp 391–400. https://doi.org/10.1038/nnano.2010.78.

(97)   Yang, Y.; Dai, H.; Yang, F.; Zhang, Y.; Luo, D.; Zhang, X.; Wang, K.; Sun, X. W.; Yao, J. All-Perovskite Photodetector with Fast Response. *Nanoscale Res. Lett.* **2019**, *14* (1), 291. https://doi.org/10.1186/s11671-019-3082-z.

(98)   Pettersson, H.; Trägårdh, J.; Persson, A. I.; Landin, L.; Hessman, D.; Samuelson, L. Infrared Photodetectors in Heterostructure Nanowires. *Nano Lett.* **2006**, *6* (2), 229–232. https://doi.org/10.1021/nl052170l.

(99)   Karimi, M.; Jain, V.; Heurlin, M.; Nowzari, A.; Hussain, L.; Lindgren, D.; Stehr, J. E.; Buyanova, I. A.; Gustafsson, A.; Samuelson, L.; et al. Room-Temperature InP/InAsP Quantum Discs-in-Nanowire Infrared Photodetectors. *Nano Lett.* **2017**, *17* (6), 3356–3362. https://doi.org/10.1021/acs.nanolett.6b05114.

(100) Banerjee, D.; Chattopadhyay, K. K. Hybrid Inorganic Organic Perovskites. In

Perovskite Photovoltaics; Elsevier, 2018; pp 123–162. https://doi.org/10.1016/b978-0-12-812915-9.00005-8.

(101)   Wang, J.; Zhang, J.; Zhou, Y.; Liu, H.; Xue, Q.; Li, X.; Chueh, C. C.; Yip, H. L.; Zhu, Z.; Jen, A. K. Y. Highly Efficient All-Inorganic Perovskite Solar Cells with Suppressed Non-Radiative Recombination by a Lewis Base. *Nat. Commun.* **2020**, *11* (1), 1–9. https://doi.org/10.1038/s41467-019-13909-5.

(102)   Xing, G.; Mathews, N.; Sun, S.; Lim, S. S.; Lam, Y. M.; Graẗzel, M.; Mhaisalkar, S.; Sum, T. C. Long-Range Balanced Electron-and Hole-Transport Lengths in Organic-Inorganic CH3NH3PbI3. *Science (80-.).* **2013**, *342* (6156), 344–347. https://doi.org/10.1126/science.1243167.

(103)   Li, T.; Liu, M.; Li, Q.; Chen, R.; Liu, X. Hybrid Photodetector Based on CsPbBr 3 Perovskite Nanocrystals and PC 71 BM Fullerene Derivative. *Chem. Phys. Lett.* **2018**, *699*, 208–211. https://doi.org/10.1016/j.cplett.2018.03.060.

(104)   Mahdi, M. S.; Ibrahim, K.; Hmood, A.; Ahmed, N. M.; Azzez, S. A.; Mustafa, F. I. A Highly Sensitive Flexible SnS Thin Film Photodetector in the Ultraviolet to near Infrared Prepared by Chemical Bath Deposition. *RSC Adv.* **2016**, *6* (116), 114980–114988. https://doi.org/10.1039/c6ra24491b.

(105)   Luo, L.-B.; Chen, J.-J.; Wang, M.-Z.; Hu, H.; Wu, C.-Y.; Li, Q.; Wang, L.; Huang, J.-A.; Liang, F.-X. Near-Infrared Light Photovoltaic Detector Based on GaAs Nanocone Array/Monolayer Graphene Schottky Junction. *Adv. Funct. Mater.* **2014**, *24* (19), 2794–2800. https://doi.org/10.1002/adfm.201303368.

(106)   Wang, X.; Li, M.; Zhang, B.; Wang, H.; Zhao, Y.; Wang, B. Recent Progress in Organometal Halide Perovskite Photodetectors. *Organic Electronics*. Elsevier B.V. January 1, 2018, pp 172–183. https://doi.org/10.1016/j.orgel.2017.10.027.

(107)   Wang, H.; Kim, D. H. Perovskite-Based Photodetectors: Materials and Devices. *Chemical Society Reviews*. Royal Society of Chemistry September 7, 2017, pp 5204–5236. https://doi.org/10.1039/c6cs00896h.

(108)   Chen, L.; Zhang, Q.; Lei, Y.; Zhu, F.; Wu, B.; Zhang, T.; Niu, G.; Xiong, Z.;

Song, Q. Photocurrent Generation through Electron-Exciton Interaction at the Organic Semiconductor Donor/Acceptor Interface. *Phys. Chem. Chem. Phys.* **2013**, *15* (39), 16891–16897. https://doi.org/10.1039/c3cp52974f.

(109) Omnes, F. Introduction to Semiconductor Photodetectors. In *Optoelectronic Sensors*; ISTE, 2010; pp 1–14. https://doi.org/10.1002/9780470611630.ch1.

(110) Reddy, T. S.; Kumar, M. C. S. Co-Evaporated SnS Thin Films for Visible Light Photodetector Applications. *RSC Adv.* **2016**, *6* (98), 95680–95692. https://doi.org/10.1039/c6ra20129f.

(111) Haddadi, A.; Dehzangi, A.; Adhikary, S.; Chevallier, R.; Razeghi, M. Background-Limited Long Wavelength Infrared InAs/InAs1−xSbx Type-II Superlattice-Based Photodetectors Operating at 110 K. *APL Mater.* **2017**, *5* (3), 035502. https://doi.org/10.1063/1.4975619.

(112) Li, Z.; Xu, K.; Wei, F. Recent Progress in Photodetectors Based on Low-Dimensional Nanomaterials. *Nanotechnology Reviews*. De Gruyter October 25, 2018, pp 393–411. https://doi.org/10.1515/ntrev-2018-0084.

(113) Tian, W.; Sun, H.; Chen, L.; Wangyang, P.; Chen, X.; Xiong, J.; Li, L. Low-dimensional Nanomaterial/Si Heterostructure-based Photodetectors. *InfoMat* **2019**, *1* (2), inf2.12014. https://doi.org/10.1002/inf2.12014.

(114) Yang, D.; Ma, D. Development of Organic Semiconductor Photodetectors: From Mechanism to Applications. *Adv. Opt. Mater.* **2019**, *7* (1), 1800522. https://doi.org/10.1002/adom.201800522.

(115) Ndiaye Dione, A.; Ndiaye, S.; Hadji Oumar Gueye, E.; Dioum, A.; Aidara Diouf, A.; Bichara Abderaman, M.; Diop Ngom, B.; Chedikh Beye, A. Optical and Electrical Modeling of a Hybrid Solar Cell Based on a Mesostructured Perovskite CH3NH3PbI3: Influence of the Depth and Thickness of the Photoactive Layer. *Am. J. Nanomater.* **2017**, *5* (2), 68–71. https://doi.org/10.12691/ajn-5-2-4.

(116) Mei, F.; Sun, D.; Mei, S.; Feng, J.; Zhou, Y.; Xu, J.; Xiao, X. Recent Progress in Perovskite-Based Photodetectors: The Design of Materials and Structures. *Adv.*

Phys. X **2019**, *4* (1), 1592709. https://doi.org/10.1080/23746149.2019.1592709.

(117) Hu, X.; Zhang, X.; Liang, L.; Bao, J.; Li, S.; Yang, W.; Xie, Y. High-Performance Flexible Broadband Photodetector Based on Organolead Halide Perovskite. *Adv. Funct. Mater.* **2014**, *24* (46), 7373–7380. https://doi.org/10.1002/adfm.201402020.

(118) Maculan, G.; Sheikh, A. D.; Abdelhady, A. L.; Saidaminov, M. I.; Haque, M. A.; Murali, B.; Alarousu, E.; Mohammed, O. F.; Wu, T.; Bakr, O. M. CH3NH3PbCl3 Single Crystals: Inverse Temperature Crystallization and Visible-Blind UV-Photodetector. *J. Phys. Chem. Lett.* **2015**, *6* (19), 3781–3786. https://doi.org/10.1021/acs.jpclett.5b01666.

(119) Saidaminov, M. I.; Adinolfi, V.; Comin, R.; Abdelhady, A. L.; Peng, W.; Dursun, I.; Yuan, M.; Hoogland, S.; Sargent, E. H.; Bakr, O. M. Planar-Integrated Single-Crystalline Perovskite Photodetectors. *Nat. Commun.* **2015**, *6* (1), 1–7. https://doi.org/10.1038/ncomms9724.

(120) Dirin, D. N.; Cherniukh, I.; Yakunin, S.; Shynkarenko, Y.; Kovalenko, M. V. Solution-Grown CsPbBr3Perovskite Single Crystals for Photon Detection. *Chem. Mater.* **2016**, *28* (23), 8470–8474. https://doi.org/10.1021/acs.chemmater.6b04298.

(121) Liu, D.; Yu, B.-B.; Liao, M.; Jin, Z.; Zhou, L.; Zhang, X.; Wang, F.; He, H.; Gatti, T.; He, Z. Self-Powered and Broadband Lead-Free Inorganic Perovskite Photodetector with High Stability. *ACS Appl. Mater. Interfaces* **2020**, *12* (27), 30530–30537. https://doi.org/10.1021/acsami.0c05636.

(122) Hussain, A. A. Constructing Caesium-Based Lead-Free Perovskite Photodetector Enabling Self-Powered Operation with Extended Spectral Response. *ACS Appl. Mater. Interfaces* **2020**, *12* (41), 46317–46329. https://doi.org/10.1021/acsami.0c14083.

(123) Tong, X. W.; Kong, W. Y.; Wang, Y. Y.; Zhu, J. M.; Luo, L. B.; Wang, Z. H. High-Performance Red-Light Photodetector Based on Lead-Free Bismuth Halide Perovskite Film. *ACS Appl. Mater. Interfaces* **2017**, *9* (22), 18977–18985.

https://doi.org/10.1021/acsami.7b04616.

(124) Hussain, A. A.; Rana, A. K.; Ranjan, M. Air-Stable Lead-Free Hybrid Perovskite Employing Self-Powered Photodetection with an Electron/Hole-Conductor-Free Device Geometry. *Nanoscale* **2019**, *11* (3), 1217–1227. https://doi.org/10.1039/c8nr08959k.

(125) Pecunia, V.; Yuan, Y.; Zhao, J.; Xia, K.; Wang, Y.; Duhm, S.; Portilla, L.; Li, F. Perovskite-Inspired Lead-Free Ag2BiI5 for Self-Powered NIR-Blind Visible Light Photodetection. *Nano-Micro Lett.* **2020**, *12* (1), 1–12. https://doi.org/10.1007/s40820-020-0371-0.

(126) Lei, L. Z.; Shi, Z. F.; Li, Y.; Ma, Z. Z.; Zhang, F.; Xu, T. T.; Tian, Y. T.; Wu, D.; Li, X. J.; Du, G. T. High-Efficiency and Air-Stable Photodetectors Based on Lead-Free Double Perovskite Cs2AgBiBr6 Thin Films. *J. Mater. Chem. C* **2018**, *6* (30), 7982–7988. https://doi.org/10.1039/c8tc02305k.

(127) Li, Y.; Shi, Z.; Liang, W.; Wang, L.; Li, S.; Zhang, F.; Ma, Z.; Wang, Y.; Tian, Y.; Wu, D.; et al. Highly Stable and Spectrum-Selective Ultraviolet Photodetectors Based on Lead-Free Copper-Based Perovskites. *Mater. Horizons* **2020**, *7* (2), 530–540. https://doi.org/10.1039/c9mh01371g.

(128) Waleed, A.; Tavakoli, M. M.; Gu, L.; Wang, Z.; Zhang, D.; Manikandan, A.; Zhang, Q.; Zhang, R.; Chueh, Y. L.; Fan, Z. Lead-Free Perovskite Nanowire Array Photodetectors with Drastically Improved Stability in Nanoengineering Templates. *Nano Lett.* **2016**, *17* (1), 523–530. https://doi.org/10.1021/acs.nanolett.6b04587.

(129) Yang, B.; Li, Y. J.; Tang, Y. X.; Mao, X.; Luo, C.; Wang, M. S.; Deng, W. Q.; Han, K. L. Constructing Sensitive and Fast Lead-Free Single-Crystalline Perovskite Photodetectors. *J. Phys. Chem. Lett.* **2018**, *9* (11), 3087–3092. https://doi.org/10.1021/acs.jpclett.8b01116.

(130) Zhang, W.; Sui, Y.; Kou, B.; Peng, Y.; Wu, Z.; Luo, J. Large-Area Exfoliated Lead-Free Perovskite-Derivative Single-Crystalline Membrane for Flexible Low-Defect Photodetectors. *ACS Appl. Mater. Interfaces* **2020**, *12* (8), 9141–9149.

https://doi.org/10.1021/acsami.9b15744.

(131) Premkumar, S.; Liu, D.; Zhang, Y.; Nataraj, D.; Ramya, S.; Jin, Z.; Mamba, B. B.; Kuvarega, A. T.; Gui, J. Stable Lead-Free Silver Bismuth Iodide Perovskite Quantum Dots for UV Photodetection. *ACS Appl. Nano Mater.* **2020**, *3* (9), 9141–9150. https://doi.org/10.1021/acsanm.0c01787.

(132) Tao, K.; Li, Y.; Ji, C.; Liu, X.; Wu, Z.; Han, S.; Sun, Z.; Luo, J. A Lead-Free Hybrid Iodide with Quantitative Response to X-Ray Radiation. *Chem. Mater.* **2019**, *31* (15), 5927–5932. https://doi.org/10.1021/acs.chemmater.9b02263.

(133) Lv, K.; Qi, S.; Liu, G.; Lou, Y.; Chen, J.; Zhao, Y. Lead-Free Silver-Antimony Halide Double Perovskite Quantum Dots with Superior Blue Photoluminescence. *Chem. Commun.* **2019**, *55* (98), 14741–14744. https://doi.org/10.1039/c9cc07397c.

(134) Zheng, X.; Zhao, W.; Wang, P.; Tan, H.; Saidaminov, M. I.; Tie, S.; Chen, L.; Peng, Y.; Long, J.; Zhang, W. H. Ultrasensitive and Stable X-Ray Detection Using Zero-Dimensional Lead-Free Perovskites. *J. Energy Chem.* **2020**, *49*, 299–306. https://doi.org/10.1016/j.jechem.2020.02.049.

(135) Turkevych, I.; Kazaoui, S.; Ito, E.; Urano, T.; Yamada, K.; Tomiyasu, H.; Yamagishi, H.; Kondo, M.; Aramaki, S. Photovoltaic Rudorffites: Lead-Free Silver Bismuth Halides Alternative to Hybrid Lead Halide Perovskites. *ChemSusChem* **2017**, *10* (19), 3754–3759. https://doi.org/10.1002/cssc.201700980.

(136) Cortecchia, D.; Dewi, H. A.; Yin, J.; Bruno, A.; Chen, S.; Baikie, T.; Boix, P. P.; Grätzel, M.; Mhaisalkar, S.; Soci, C.; et al. Lead-Free $MA_2CuCl_xBr_{4-x}$ Hybrid Perovskites. *Inorg. Chem.* **2016**, *55* (3), 1044–1052. https://doi.org/10.1021/acs.inorgchem.5b01896.

(137) Krishnan, B.; Arato, A.; Cardenas, E.; Roy, T. K. D.; Castillo, G. A. On the Structure, Morphology, and Optical Properties of Chemical Bath Deposited Sb_2S_3 Thin Films. *Appl. Surf. Sci.* **2008**, *254* (10), 3200–3206. https://doi.org/10.1016/j.apsusc.2007.10.098.

(138) Garza, C.; Shaji, S.; Arato, A.; Perez Tijerina, E.; Alan Castillo, G.; Das Roy, T. K.; Krishnan, B. P-Type CuSbS2 Thin Films by Thermal Diffusion of Copper into Sb2S3. *Sol. Energy Mater. Sol. Cells* **2011**, *95* (8), 2001–2005. https://doi.org/10.1016/j.solmat.2010.06.011.

(139) Sahu, N.; Parija, B.; Panigrahi, S. Fundamental Understanding and Modeling of Spin Coating Process: A Review. In *Indian Journal of Physics*; Springer, 2009; Vol. 83, pp 493–502. https://doi.org/10.1007/s12648-009-0009-z.

(140) X-Ray Diffraction - an overview | ScienceDirect Topics https://www.sciencedirect.com/topics/materials-science/x-ray-diffraction (accessed May 14, 2020).

(141) Raman Spectroscopy - an overview | ScienceDirect Topics https://www.sciencedirect.com/topics/neuroscience/raman-spectroscopy (accessed May 14, 2020).

(142) Abd Mutalib, M.; Rahman, M. A.; Othman, M. H. D.; Ismail, A. F.; Jaafar, J. Scanning Electron Microscopy (SEM) and Energy-Dispersive X-Ray (EDX) Spectroscopy. In *Membrane Characterization*; Elsevier Inc., 2017; pp 161–179. https://doi.org/10.1016/B978-0-444-63776-5.00009-7.

(143) Greczynski, G.; Hultman, L. X-Ray Photoelectron Spectroscopy: Towards Reliable Binding Energy Referencing. *Progress in Materials Science*. Elsevier Ltd January 1, 2020, p 100591. https://doi.org/10.1016/j.pmatsci.2019.100591.

(144) Lu, F.; Wang, W.; Luo, X.; Xie, X.; Cheng, Y.; Dong, H.; Liu, H.; Wang, W. H. A Class of Monolayer Metal Halogenides MX2: Electronic Structures and Band Alignments. *Appl. Phys. Lett.* **2016**, *108* (13), 132104. https://doi.org/10.1063/1.4945366.

(145) Wang, Q. H.; Kalantar-Zadeh, K.; Kis, A.; Coleman, J. N.; Strano, M. S. Electronics and Optoelectronics of Two-Dimensional Transition Metal Dichalcogenides. *Nature Nanotechnology*. Nature Publishing Group November 6, 2012, pp 699–712. https://doi.org/10.1038/nnano.2012.193.

(146) Kumar, A.; Singh, A.; Ojha, A. K. A New Approach to Predict the Formation of 3D Hybrid Organic-inorganic Perovskites. *Int. J. Quantum Chem.* **2019**, *119* (22). https://doi.org/10.1002/qua.26012.

(147) Yi, Z.; Ladi, N. H.; Shai, X.; Li, H.; Shen, Y.; Wang, M. Will Organic-Inorganic Hybrid Halide Lead Perovskites Be Eliminated from Optoelectronic Applications? *Nanoscale Advances*. Royal Society of Chemistry April 9, 2019, pp 1276–1289. https://doi.org/10.1039/c8na00416a.

(148) Virko, S.; Petrenko, T.; Yaremko, A.; Wysokiński, R.; Michalska, D. Density Functional and Ab Initio Studies of the Molecular Structures and Vibrational Spectra of Metal Triiodides, MI3 (M = As, Sb, Bi). *J. Mol. Struct. THEOCHEM* **2002**, *582* (1–3), 137–142. https://doi.org/10.1016/S0166-1280(01)00779-5.

(149) Mady, K. A.; Eid, A. H.; Soliman, W. Z. Optical Properties and Interband Transitions in the Layered Compounds SbI3. *Czechoslov. J. Phys.* **1979**, *29* (8), 907–912. https://doi.org/10.1007/BF01596368.

(150) Lai, K.; Yan, C. L.; Gao, L. Q.; Zhang, W. B. AI3 (A = As, Sb) Single Layers and Their VdW Heterostructure for Photocatalysis and Solar Cell Applications. *J. Phys. Chem. C* **2018**, *122* (14), 7656–7663. https://doi.org/10.1021/acs.jpcc.8b01874.

(151) Lai, K.; Li, H.; Xu, Y. K.; Zhang, W. B.; Dai, J. Achieving a Direct Band Gap and High Power Conversion Efficiency in an SbI3/BiI3 Type-II VdW Heterostructure: Via Interlayer Compression and Electric Field Application. *Phys. Chem. Chem. Phys.* **2019**, *21* (5), 2619–2627. https://doi.org/10.1039/c8cp07298a.

(152) Kępińska, M.; Nowak, M.; Duka, P.; Kotyczka-Morańska, M.; Szperlich, P. Optical Properties of SbI3 Single Crystalline Platelets. *Opt. Mater. (Amst).* **2011**, *33* (11), 1753–1759. https://doi.org/10.1016/j.optmat.2011.06.009.

(153) Kępińska, M.; Starczewska, A.; Bednarczyk, I.; Szala, J.; Szperlich, P.; Mistewicz, K. Fabrication and Characterisation of SbI3-Opal Structures. *Mater. Lett.* **2014**, *130*, 17–20. https://doi.org/10.1016/j.matlet.2014.05.063.

(154) Sun, X. X.; Li, C.; Hou, Q. Y.; Zhang, Y. Phase Transition and Electronic Properties of SbI3: First-Principles Calculations. *Mod. Phys. Lett. B* **2017**, *31* (18), 1750200. https://doi.org/10.1142/S0217984917502001.

(155) Mady, K. A.; Eid, A. H.; Soliman, W. Z. Electrical Conductivity of Antimony Triiodide Single Crystals. *J. Mater. Sci. Lett.* **1987**, *6* (3), 251–253. https://doi.org/10.1007/BF01729316.

(156) Hassan, M.; Al-hakimi, A. N.; Rafiuddin. Electrical Conductivity of AgI-CdI2-KI and AgI-CuI-KI Ionic Conducting Systems. *Arab. J. Chem.* **2011**, *4* (1), 45–49. https://doi.org/10.1016/j.arabjc.2010.06.017.

(157) Sáfrán, G.; Geszti, O.; Radnóczi, G.; Barna, P. B.; Tóth, K. TEM Study of the Structure and Morphology of AgI Crystals Formed on Ag (001), (011) and (111) Thin Films. *Thin Solid Films* **1995**, *259* (1), 96–104. https://doi.org/10.1016/0040-6090(94)06412-1.

(158) Fokina, S. V.; Borisov, E. N.; Tomaev, V. V.; Tumkin, I. I.; Tveryanovich, Y. S. AgI Thin Films Prepared by Laser Ablation. *Solid State Ionics* **2016**, *297*, 64–67. https://doi.org/10.1016/j.ssi.2016.10.004.

(159) Wen, X. J.; Shen, C. H.; Fei, Z. H.; Fang, D.; Liu, Z. T.; Dai, J. T.; Niu, C. G. Recent Developments on AgI Based Heterojunction Photocatalytic Systems in Photocatalytic Application. *Chemical Engineering Journal*. Elsevier B.V. March 1, 2020, p 123083. https://doi.org/10.1016/j.cej.2019.123083.

(160) Yu, C.; Wei, L.; Zhou, W.; Chen, J.; Fan, Q.; Liu, H. Enhancement of the Visible Light Activity and Stability of Ag 2 CO 3 Byformation of AgI/Ag 2 CO 3 Heterojunction. *Appl. Surf. Sci.* **2014**, *319* (1), 312–318. https://doi.org/10.1016/j.apsusc.2014.05.158.

(161) Bharathi Mohan, D.; Sunandana, C. S. Iodization of Rf Sputter Induced Disordered Ag Thin Films Reveals Volume Plasmon-Exciton "Transition." *J. Appl. Phys.* **2006**, *100* (6), 064314. https://doi.org/10.1063/1.2353238.

(162) Fortunato, E.; Barquinha, P.; Martins, R. Oxide Semiconductor Thin-Film

Transistors: A Review of Recent Advances. *Adv. Mater.* **2012**, *24* (22), 2945–2986. https://doi.org/10.1002/adma.201103228.

(163) Schein, F. L.; Von Wenckstern, H.; Grundmann, M. Transparent P-CuI/n-ZnO Heterojunction Diodes. *Appl. Phys. Lett.* **2013**, *102* (9), 092109. https://doi.org/10.1063/1.4794532.

(164) Cota-Leal, M.; Cabrera-German, D.; Sotelo-Lerma, M.; Martínez-Gil, M.; García-Valenzuela, J. A. Highly-Transparent and Conductive CuI Films Obtained by a Redirected Low-Cost and Electroless Two-Step Route: Chemical Solution Deposition of CuS 2 and Subsequent Iodination. *Mater. Sci. Semicond. Process.* **2019**, *95*, 59–67. https://doi.org/10.1016/j.mssp.2019.02.016.

(165) Baek, S. D.; Kwon, D. K.; Kim, Y. C.; Myoung, J. M. Violet Light-Emitting Diodes Based on p-CuI Thin Film/n-MgZnO Quantum Dot Heterojunction. *ACS Appl. Mater. Interfaces* **2020**, *12* (5), 6037–6047. https://doi.org/10.1021/acsami.9b18507.

(166) Alami, A. H.; Faraj, M.; Aokal, K.; Abu Hawili, A.; Tawalbeh, M.; Zhang, D. Investigating Various Permutations of Copper Iodide/FeCu Tandem Materials as Electrodes for Dye-Sensitized Solar Cells with a Natural Dye. *Nanomaterials* **2020**, *10* (4), 784. https://doi.org/10.3390/nano10040784.

(167) Kariper, I. A. CuI Film Produced by Chemical Extraction Method in Different Media. *Mater. Res.* **2016**, *19* (5), 991–998. https://doi.org/10.1590/1980-5373-MR-2016-0067.

(168) Sun, W.; Peng, H.; Li, Y.; Yan, W.; Liu, Z.; Bian, Z.; Huang, C. Solution-Processed Copper Iodide as an Inexpensive and Effective Anode Buffer Layer for Polymer Solar Cells. *J. Phys. Chem. C* **2014**, *118* (30), 16806–16812. https://doi.org/10.1021/jp412784q.

(169) Miyake, S.; Hoshino, S.; Takenaka, T. On the Phase Transition in Cuprous Iodide. *J. Phys. Soc. Japan* **1952**, *7* (1), 19–24. https://doi.org/10.1143/JPSJ.7.19.

(170) Christians, J. A.; Fung, R. C. M.; Kamat, P. V. An Inorganic Hole Conductor for

Organo-Lead Halide Perovskite Solar Cells. Improved Hole Conductivity with Copper Iodide. *J. Am. Chem. Soc.* **2014**, *136* (2), 758–764. https://doi.org/10.1021/ja411014k.

(171) Wang, Y.; Shi, X.; Wang, G.; Tong, J.; Pan, D. All-Inorganic and Lead-Free BiI3thin Film Solar Cells by Iodization of BiSI Thin Films. *J. Mater. Chem. C* **2020**, *8* (40), 14066–14074. https://doi.org/10.1039/d0tc03753b.

(172) Pandian, M. G. M.; Khadka, D. B.; Shirai, Y.; Umedov, S.; Yanagida, M.; Subashchandran, S.; Grigorieva, A.; Miyano, K. Effect of Solvent Vapour Annealing on Bismuth Triiodide Film for Photovoltaic Applications and Its Optoelectronic Properties. *J. Mater. Chem. C* **2020**, *8* (35), 12173–12180. https://doi.org/10.1039/d0tc02455d.

(173) Hamdeh, U. H.; Nelson, R. D.; Ryan, B. J.; Bhattacharjee, U.; Petrich, J. W. Solution-Processed BiI3 Thin Films for Photovoltaic Applications: Improved Carrier Collection via Solvent Annealing. https://doi.org/10.1021/acs.chemmater.6b02347.

(174) Yang, Y.; Wang, C.; Hou, J.; Dai, J. Raman Scattering, Far Infrared Spectrum of BiI3 Nanocrystallites. *Mater. Lett.* **2003**, *57* (15), 2185–2188. https://doi.org/10.1016/S0167-577X(02)01171-0.

(175) Hsueh, H. C.; Chen, R. K.; Vass, H.; Clark, S. J.; Ackland, G. J.; Poon, W. C.-K.; Crain, J. Compression Mechanisms in Quasimolecular X I 3 (X = A s , S b , B i) Solids. *Phys. Rev. B* **1998**, *58* (22), 14812–14822. https://doi.org/10.1103/PhysRevB.58.14812.

(176) Moulder, J. F.; Stickle, W. F.; Sobol, P. E.; Bomben, K. D. *Handbook of X-Ray Photoelectron Spectroscopy: A Reference Book of Standard Spectra for Identification and Interpretation of XPS Data*; Physical Electronics Division, Perkin-Elmer Corp, 1992. https://doi.org/9780962702624.

(177) Qiu, W.; Dudder, G. J.; Zhao, X.; Perry, S. S.; Nino, J. C. Interfacial Reactivity of Au, Pd, and Pt on BiI 3 (001): Implications for Electrode Selection. *ACS Appl. Mater. Interfaces* **2011**, *3* (6), 1910–1917. https://doi.org/10.1021/am200120j.

(178) Xu, B.; Hao, J.; Guo, Q.; Wang, J.; Bai, G.; Fei, B.; Zhou, S.; Qiu, J. Ultrabroadband Near-Infrared Luminescence and Efficient Energy Transfer in Bi and Bi/Ho Co-Doped Thin Films. *J. Mater. Chem. C* **2014**, *2* (14), 2482. https://doi.org/10.1039/c3tc32177k.

(179) Garg, A.; Tomar, M.; Gupta, V. Synthesis and Characterisation of Thin Films of Bismuth Triiodide for Semiconductor Radiation Detectors. *Conf. Pap. Sci.* **2014**, *2014*, 1–3. https://doi.org/10.1155/2014/370436.

(180) Jellison, G. E.; Ramey, J. O.; Boatner, L. A. Optical Functions of   BiI 3   as Measured by Generalized Ellipsometry. *Phys. Rev. B* **1999**, *59* (15), 9718–9721. https://doi.org/10.1103/PhysRevB.59.9718.

(181) Lehner, A. J.; Wang, H.; Fabini, D. H.; Liman, C. D.; Hébert, C.-A.; Perry, E. E.; Wang, M.; Bazan, G. C.; Chabinyc, M. L.; Seshadri, R. Electronic Structure and Photovoltaic Application of BiI ₃. *Appl. Phys. Lett.* **2015**, *107* (13), 131109. https://doi.org/10.1063/1.4932129.

(182) Jain, S. M.; Phuyal, D.; Davies, M. L.; Li, M.; Philippe, B.; De Castro, C.; Qiu, Z.; Kim, J.; Watson, T.; Tsoi, W. C.; et al. An Effective Approach of Vapour Assisted Morphological Tailoring for Reducing Metal Defect Sites in Lead-Free, (CH3NH3)3Bi2I9 Bismuth-Based Perovskite Solar Cells for Improved Performance and Long-Term Stability. *Nano Energy* **2018**, *49*, 614–624. https://doi.org/10.1016/J.NANOEN.2018.05.003.

(183) Bharathi Mohan, D.; Philip, A.; Sunandana, C. S. Iodization of Antimony Thin Films: XRD, SEM and Optical Studies of Nanostructured SbI3. *Vacuum* **2008**, *82* (6), 561–565. https://doi.org/10.1016/j.vacuum.2007.08.014.

(184) Tiwari, D.; Alibhai, D.; Fermin, D. J. Above 600 MV Open-Circuit Voltage BiI3 Solar Cells. *ACS Energy Lett.* **2018**, *3* (8), 1882–1886. https://doi.org/10.1021/acsenergylett.8b01182.

(185) Drago, R. S. On Pearson's Quantitative Statement of HSAB. *Inorganic Chemistry*. American Chemical Society September 1, 1973, pp 2211–2212. https://doi.org/10.1021/ic50127a063.

(186) R. Loudon. Theory of the First-Order Raman Effect in Crystals. *J. Phys.* **1963**, *275* (1361), 218–232. https://doi.org/10.1098/rspa.1963.0166.

(187) Anderson, A.; Campbell, J. A.; Syme, R. W. G. Raman Spectra of Crystalline Antimony Triiodide and Arsenic Triiodide. *J. Raman Spectrosc.* **1988**, *19* (6), 379–382. https://doi.org/10.1002/jrs.1250190602.

(188) Saitoh, A.; Komatsu, T.; Karasawa, T.; Ohtake, H.; Suemoto, T. Raman Scattering under Hydrostatic Pressures in Layered BiI3 and SbI3 Crystals. *Phys. status solidi* **2001**, *226* (2), 357–367. https://doi.org/10.1002/1521-3951(200108)226:2<357::AID-PSSB357>3.0.CO;2-8.

(189) C.D. Wagner, A.V. Naumkin, A. Kraut-Vass, J.W. Allison, C.J. Powell, J. R. J. R. NIST Standard Reference Database 20,Version 3.4 (web version),2003 http:/srdata.nist.gov/xps/ (accessed Jul 13, 2020).

(190) Shaji, S.; Garcia, L. V.; Loredo, S. L.; Krishnan, B.; Aguilar Martinez, J. A.; Das Roy, T. K.; Avellaneda, D. A. Antimony Sulfide Thin Films Prepared by Laser Assisted Chemical Bath Deposition. *Appl. Surf. Sci.* **2017**, *393*, 369–376. https://doi.org/10.1016/j.apsusc.2016.10.051.

(191) Liu, P.; Lu, F.; Wu, M.; Luo, X.; Cheng, Y.; Wang, X. W.; Wang, W.; Wang, W. H.; Liu, H.; Cho, K. Electronic Structures and Band Alignments of Monolayer Metal Trihalide Semiconductors MX3. *J. Mater. Chem. C* **2017**, *5* (35), 9066–9071. https://doi.org/10.1039/c7tc03003g.

(192) Boopathi, K. M.; Karuppuswamy, P.; Singh, A.; Hanmandlu, C.; Lin, L.; Abbas, S. A.; Chang, C. C.; Wang, P. C.; Li, G.; Chu, C. W. Solution-Processable Antimony-Based Light-Absorbing Materials beyond Lead Halide Perovskites. *J. Mater. Chem. A* **2017**, *5* (39), 20843–20850. https://doi.org/10.1039/c7ta06679a.

(193) Cho, D. Y.; Tappertzhofen, S.; Waser, R.; Valov, I. Chemically-Inactive Interfaces in Thin Film Ag/AgI Systems for Resistive Switching Memories. *Sci. Rep.* **2013**, *3* (1), 1–5. https://doi.org/10.1038/srep01169.

(194) Petkova, T.; Ilcheva, V.; Popov, C.; Reithmaier, J. P.; Socol, G.; Axente, E.;

Mihailescu, I. N.; Petkov, P.; Hineva, T. Study of (As2Se3)100-X(AgI)X Thin Films Prepared by Pld and Vte Methods. In *Nanostructured Materials for Advanced Technological Applications*; Springer Netherlands, 2009; pp 329–334. https://doi.org/10.1007/978-1-4020-9916-8_35.

(195) Mohan, D. B.; Reddy, V. S.; Sunandana, C. S. AgI Nanostructure Development in Sputter-Disordered and Al-Doped Ag Films Probed by XRD, SEM, Optical Absorption and Photoluminescence. *Appl. Phys. A Mater. Sci. Process.* **2007**, *86* (1), 73–82. https://doi.org/10.1007/s00339-006-3727-5.

(196) Palles, D.; Konidakis, I.; Varsamis, C. P. E.; Kamitsos, E. I. Vibrational Spectroscopic and Bond Valence Study of Structure and Bonding in Al2O3-Containing AgI-AgPO3 Glasses. *RSC Adv.* **2016**, *6* (20), 16697–16710. https://doi.org/10.1039/c6ra00162a.

(197) Fontana, A.; Rossi, F.; Armellini, C.; Dangelo, G.; Tripodo, G.; Bartolotta, A. Low-Temperature Optical and Thermal Properties of AgI-Based Phosphate Glasses. *Philos. Mag. B* **1999**, *79* (11–12), 2073–2080. https://doi.org/10.1080/13642819908223096.

(198) Kostadinova, O.; Petkova, T.; Chrissanthopoulos, A.; Petkov, P.; Yannopoulos, S. N. Structure of AgI-AsSe Glasses by Raman Scattering and Ab Initio Calculations. In *Nanotechnological Basis for Advanced Sensors*; Springer, Dordrecht, 2011; pp 217–223. https://doi.org/10.1007/978-94-007-0903-4_23.

(199) Salamon, M. Ben. *Physics of Superionic Conductors*; 2013. https://doi.org/10.1007/978-3-642-81328-3.

(200) Preda, N.; Mihut, L.; Baibarac, M.; Baltog, I. Intercalation of Layered Metal Iodides with Pyridine Evidenced by Raman Spectroscopy. *Acta Phys. Pol. A* **2009**, *116* (1), 81–83. https://doi.org/10.12693/APhysPolA.116.81.

(201) Zheng, Z.; Liu, A. R.; Wang, S. M.; Huang, B. J.; Ma, X. M.; Zhao, H. X.; Li, D. P.; Zhang, L. Z. In Situ Fabrication of AgI Films on Various Substrates. *Mater. Res. Bull.* **2008**, *43* (8–9), 2491–2496. https://doi.org/10.1016/j.materresbull.2007.09.017.

(202)   Wang, X.; Yang, J.; Ma, S.; Zhao, D.; Dai, J.; Zhang, D. In Situ Fabrication of
        AgI/AgVO $_3$ Nanoribbon Composites with Enhanced Visible Photocatalytic
        Activity for Redox Reactions. *Catal. Sci. Technol.* **2016**, *6* (1), 243–253.
        https://doi.org/10.1039/C5CY00787A.

(203)   Kato, Y.; Ono, L. K.; Lee, M. V.; Wang, S.; Raga, S. R.; Qi, Y. Silver Iodide
        Formation in Methyl Ammonium Lead Iodide Perovskite Solar Cells with Silver
        Top Electrodes. *Adv. Mater. Interfaces* **2015**, *2* (13), 1500195.
        https://doi.org/10.1002/admi.201500195.

(204)   Liang, C.; Niu, C. G.; Guo, H.; Huang, D. W.; Wen, X. J.; Yang, S. F.; Zeng, G.
        M. Combination of Efficient Charge Separation with the Assistance of Novel
        Dual Z-Scheme System: Self-Assembly Photocatalyst Ag@AgI/BiOI Modified
        Oxygen-Doped Carbon Nitride Nanosheet with Enhanced Photocatalytic
        Performance. *Catal. Sci. Technol.* **2018**, *8* (4), 1161–1175.
        https://doi.org/10.1039/c7cy02190a.

(205)   Kaushik, D. K.; Selvaraj, M.; Ramu, S.; Subrahmanyam, A. Thermal Evaporated
        Copper Iodide (CuI) Thin Films: A Note on the Disorder Evaluated through the
        Temperature Dependent Electrical Properties. *Sol. Energy Mater. Sol. Cells* **2017**,
        165, 52–58. https://doi.org/10.1016/j.solmat.2017.02.030.

(206)   Zi, M.; Li, J.; Zhang, Z.; Wang, X.; Han, J.; Yang, X.; Qiu, Z.; Gong, H.; Ji, Z.;
        Cao, B. Effect of Deposition Temperature on Transparent Conductive Properties
        of γ-CuI Film Prepared by Vacuum Thermal Evaporation. *Phys. status solidi*
        2015, *212* (7), 1466–1470. https://doi.org/10.1002/pssa.201532015.

(207)   Faustino, B. M. M.; Gomes, D.; Faria, J.; Juntunen, T.; Gaspar, G.; Bianchi, C.;
        Almeida, A.; Marques, A.; Tittonen, I.; Ferreira, I. CuI P-Type Thin Films for
        Highly Transparent Thermoelectric p-n Modules. *Sci. Rep.* **2018**, *8* (1), 6867.
        https://doi.org/10.1038/s41598-018-25106-3.

(208)   Dintle, L. K.; Luhanga, P. V. C.; Moditswe, C.; Muiva, C. M. Dependence of
        Structural and Optoelectronic Properties on Thickness of γ-Cui Thin Films
        Deposited by Vacuum Thermal Evaporation. In *MRS Advances*; Materials

Research Society, 2018; Vol. 3, pp 2627–2642.
https://doi.org/10.1557/adv.2018.317.

(209) Serrano, J.; Cardona, M.; Ritter, T. M.; Weinstein, B. A.; Rubio, A.; Lin, C. T. Pressure and Temperature Dependence of the Raman Phonons in Isotopic γ-CuI. *Phys. Rev. B - Condens. Matter Mater. Phys.* **2002**, *66* (24), 1–12. https://doi.org/10.1103/PhysRevB.66.245202.

(210) Kumar, M.; Bhatt, V.; Nayal, O. S.; Sharma, S.; Kumar, V.; Thakur, M. S.; Kumar, N.; Bal, R.; Singh, B.; Sharma, U. CuI Nanoparticles as Recyclable Heterogeneous Catalysts for C-N Bond Formation Reactions. *Catal. Sci. Technol.* **2017**, *7* (13), 2857–2864. https://doi.org/10.1039/c7cy00832e.

(211) Liu, A.; Zhu, H.; Park, W.-T.; Kang, S.-J.; Xu, Y.; Kim, M.-G.; Noh, Y.-Y. Room-Temperature Solution-Synthesized p-Type Copper(I) Iodide Semiconductors for Transparent Thin-Film Transistors and Complementary Electronics. *Adv. Mater.* **2018**, *30* (34), 1802379. https://doi.org/10.1002/adma.201802379.

(212) Yang, Z.; Wang, M.; Ding, J.; Sun, Z.; Li, L.; Huang, J.; Liu, J.; Shao, J. Semi-Transparent ZnO-CuI/CuSCN Photodiode Detector with Narrow-Band UV Photoresponse. *ACS Appl. Mater. Interfaces* **2015**, *7* (38), 21235–21244. https://doi.org/10.1021/acsami.5b05222.

(213) Sun, M.; Hu, J.; Zhai, C.; Zhu, M.; Pan, J. A P-n Heterojunction of CuI/TiO2 with Enhanced Photoelectrocatalytic Activity for Methanol Electro-Oxidation. *Electrochim. Acta* **2017**, *245*, 863–871. https://doi.org/10.1016/j.electacta.2017.06.035.

(214) Nowak, M.; Szperlich, P.; Talik, E.; Szala, J.; Rzychoń, T.; Stróz, D.; Nowrot, A.; Solecka, B. Sonochemical Preparation of Antimony Subiodide. *Ultrason. Sonochem.* **2010**, *17* (1), 219–227. https://doi.org/10.1016/j.ultsonch.2009.05.016.

(215) Balog, Á.; Samu, G. F.; Kamat, P. V.; Janáky, C. Optoelectronic Properties of CuI Photoelectrodes. *J. Phys. Chem. Lett.* **2019**, *10* (2), 259–264. https://doi.org/10.1021/acs.jpclett.8b03242.

(216) Yang, C.; Kneib, M.; Lorenz, M.; Grundmann, M. Room-Temperature Synthesized Copper Iodide Thin Filmas Degenerate p-Type Transparent Conductor with a Boosted Figure of Merit. *Proc. Natl. Acad. Sci. U. S. A.* **2016**, *113* (46), 12929–12933. https://doi.org/10.1073/pnas.1613643113.

(217) Cha, J. H.; Jung, D. Y. Air-Stable Transparent Silver Iodide-Copper Iodide Heterojunction Diode. *ACS Appl. Mater. Interfaces* **2017**, *9* (50), 43807–43813. https://doi.org/10.1021/acsami.7b14378.

(218) Hosseini, S. S.; Adelifard, M.; Ataei, M. An Investigation on Physical Properties of Ag2BiI5 Absorber Layers Synthesized by Microwave Assisted Spin Coating Technique. *J. Mater. Sci. Mater. Electron.* **2019**, *30* (5), 5021–5029. https://doi.org/10.1007/s10854-019-00799-y.

(219) Jung, K. W.; Sohn, M. R.; Lee, H. M.; Yang, I. S.; Sung, S. Do; Kim, J.; Wei-Guang Diau, E.; Lee, W. I. Silver Bismuth Iodides in Various Compositions as Potential Pb-Free Light Absorbers for Hybrid Solar Cells. *Sustain. Energy Fuels* **2018**, *2* (1), 294–302. https://doi.org/10.1039/C7SE00477J.

(220) Mashadieva, L. F.; Aliev, Z. S.; Shevelkov, A. V.; Babanly, M. B. Experimental Investigation of the Ag–Bi–I Ternary System and Thermodynamic Properties of the Ternary Phases. *J. Alloys Compd.* **2013**, *551*, 512–520. https://doi.org/10.1016/J.JALLCOM.2012.11.033.

(221) Klaeboe, P. The Raman Spectra of Some Iodine, Bromine, and Iodine Monochloride Charge-Transfer Coomplexes in Solution. *J. Am. Chem. Soc.* **1967**, *89* (15), 3667–3676. https://doi.org/10.1021/ja00991a001.

(222) Khadka, D. B.; Shirai, Y.; Yanagida, M.; Miyano, K. Tailoring the Film Morphology and Interface Band Offset of Caesium Bismuth Iodide-Based Pb-Free Perovskite Solar Cells. *J. Mater. Chem. C* **2019**, *7* (27), 8335–8343. https://doi.org/10.1039/c9tc02181g.

(223) Ghosh, B.; Wu, B.; Guo, X.; Harikesh, P. C.; John, R. A.; Baikie, T.; Wee, A. T. S.; Guet, C. Superior Performance of Silver Bismuth Iodide Photovoltaics Fabricated via Dynamic Hot-Casting Method under Ambient Conditions. **2018**,

1802051, 1–7. https://doi.org/10.1002/aenm.201802051.

(224) Tubbs, M. R. The Optical Absorption Spectra of Metal Iodides with Layer Structures. *J. Phys. Chem. Solids* **1968**, *29* (7), 1191–1203. https://doi.org/10.1016/0022-3697(68)90211-4.

(225) Oh, J. T.; Kim, D. H.; Kim, Y. Solution-Processed"silver-Bismuth-Iodine" Ternary Thin Films for Lead-Free Photovoltaic Absorbers. *J. Vis. Exp.* **2018**, *2018* (139). https://doi.org/10.3791/58286.

(226) Periyanagounder, D.; Gnanasekar, P.; Varadhan, P.; He, J. H.; Kulandaivel, J. High Performance, Self-Powered Photodetectors Based on a Graphene/Silicon Schottky Junction Diode. *J. Mater. Chem. C* **2018**, *6* (35), 9545–9551. https://doi.org/10.1039/c8tc02786b.

(227) Pecunia, V.; Yuan, Y.; Zhao, J.; Xia, K.; Wang, Y.; Duhm, S.; Portilla, L.; Li, F. Perovskite-Inspired Lead-Free Ag2BiI5 for Self-Powered NIR-Blind Visible Light Photodetection. *Nano-Micro Lett.* **2020**, *12* (1), 1–12. https://doi.org/10.1007/s40820-020-0371-0.

(228) Tong, X. W.; Kong, W. Y.; Wang, Y. Y.; Zhu, J. M.; Luo, L. B.; Wang, Z. H. High-Performance Red-Light Photodetector Based on Lead-Free Bismuth Halide Perovskite Film. *ACS Appl. Mater. Interfaces* **2017**, *9* (22), 18977–18985. https://doi.org/10.1021/acsami.7b04616.

(229) Bogner, U.; Röska, G. Fluorescence Changes of Dyes in Amorphous Solids, Induced by Selective Laser Excitation and by Heat Pulses. *J. Lumin.* **1981**, *24–25*, 683–686. https://doi.org/10.1016/0022-2313(81)90070-3.

(230) Klab, T.; Luszczynska, B.; Ulanski, J.; Wei, Q.; Chen, G.; Zou, Y. Influence of PEIE Interlayer on Detectivity of Red-Light Sensitive Organic Non-Fullerene Photodetectors with Reverse Structure. *Org. Electron.* **2020**, *77*, 1566–1199. https://doi.org/10.1016/j.orgel.2019.105527.

(231) Cao, J.; Xu, B.; Lin, H.; Luo, B.; Chen, S. Novel Heterostructured Bi2S3/BiOI Photocatalyst: Facile Preparation, Characterization and Visible Light

145

Photocatalytic Performance. *Dalt. Trans.* **2012**, *41* (37), 11482–11490. https://doi.org/10.1039/c2dt30883e.

Resume
Anjali Adappattu Ramachandran

Contact Address:

Av. Pico Bolivar1115, Las Puentes, Sector 11, San Nicolas De Los

Garza, 66460, Monterrey, Nuevo León, México
Email ID:

anjaliar033@gmail.com

LinkedIn:

linkedin.com/in/anjali-a-r-a7466714

Contact Number:

+52 8182706915

Nationality: Indian

Gender: Female

FIELDS OF INTEREST:

Thin Film, Photocatalysis, Laser ablation

EDUCATIONAL QUALIFICATIONS:
01/2017 - Present:

Doctoral degree in Materials Engineering –
Facultad de Ingeniería Mecánica y Eléctrica,
Universidad Autónoma de Nuevo León,
México

Master of Science in Physics –
Sree Sankara College, Kalady,
Mahatma Gandhi University, Kerala, India

Bachelor of Science in Physics –
Mar Thoma College for Women,
Mahatma Gandhi University, Kerala, India

147

PUBLICATION:

- **A.A. Ramachandran**, B. Krishnan, D.A.A. Leal, E.G. Martinez, J.A.A. Martinez, D.A. Avellaneda, S. Shaji, "*Ag$_2$BiI$_5$ perovskite thin films: Studies on structure, morphology, composition and optoelectronic properties for visible photodetector application*", Mater. Today Commun. 24 (2020) 101092. doi:10.1016/j.mtcomm.2020.101092.

EXPERIMENTAL SKILLS:

- Thin film coating using Spin coating, Chemical bath deposition, and Thermal evaporator system.
- Synthesis and optimization of experimental conditions for new perovskite materials and their optoelectronic properties.
- Characterization Skills such as Powder X-ray Diffraction, Raman spectroscopy, scanning electron microscopy (SEM), UV-Vis-NIR Spectroscopy, EDX, XPS, electrical measurements using Keithley Source Measuring Unit.